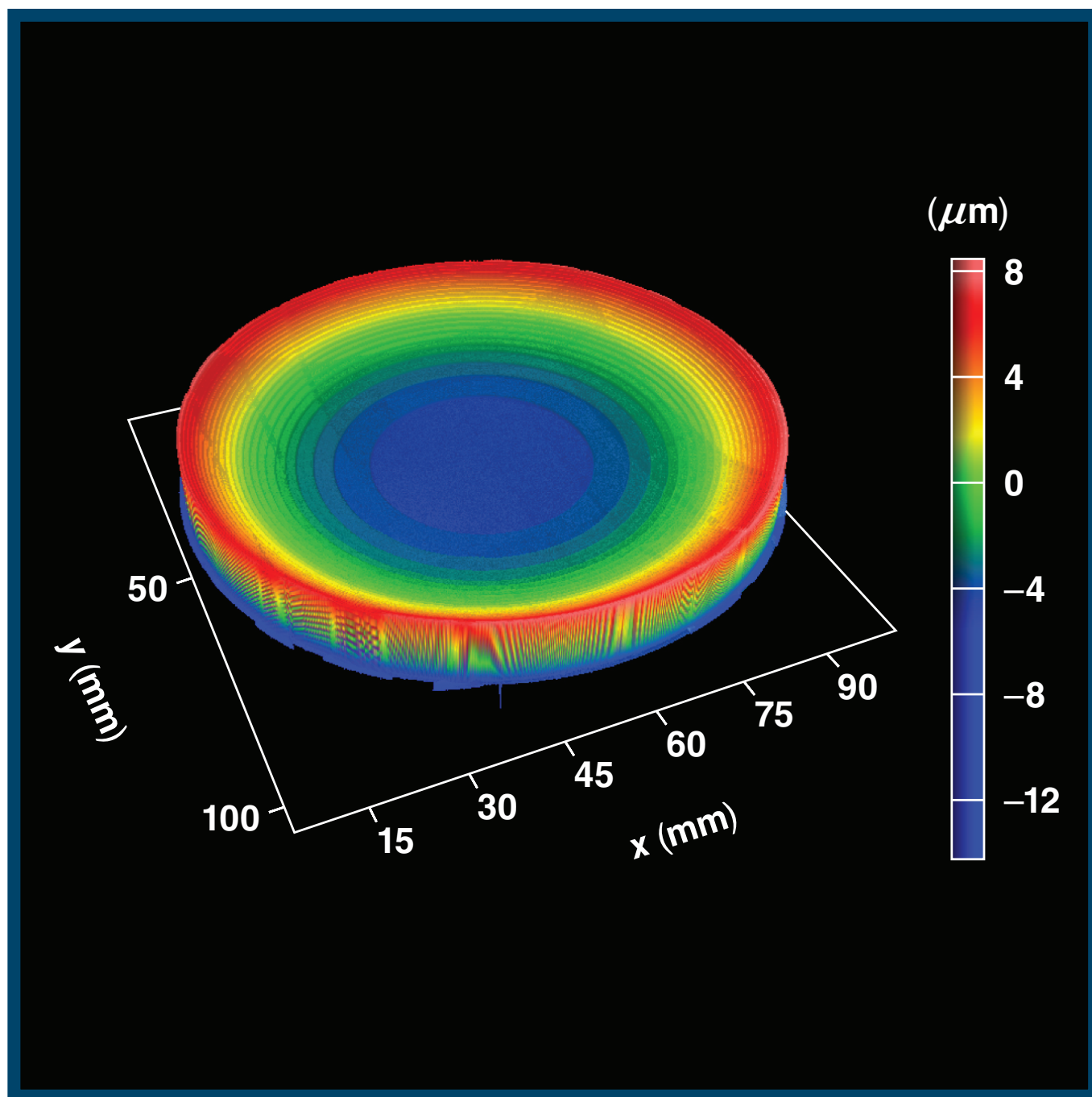


# LLE Review



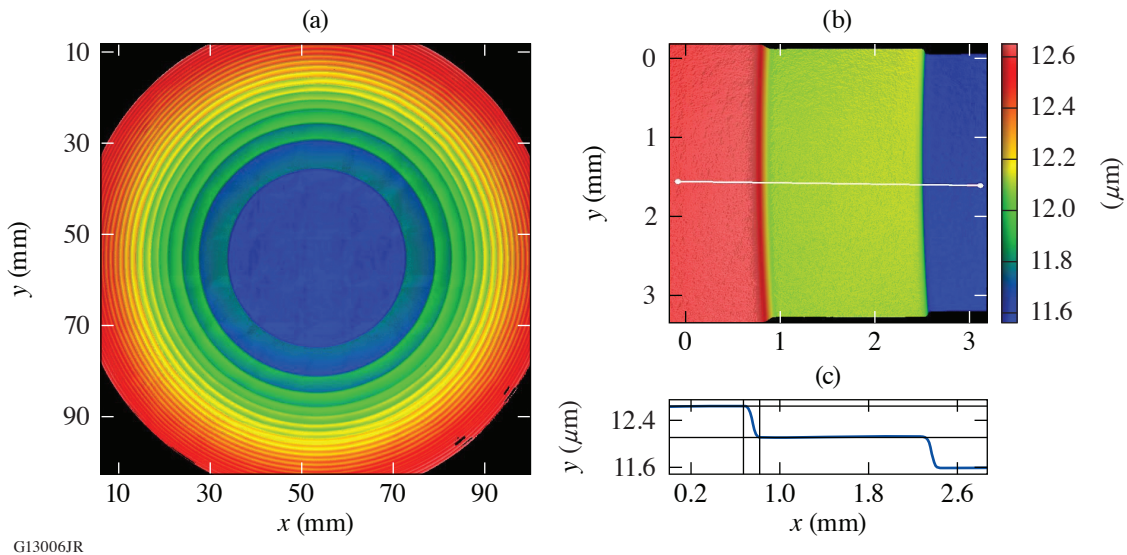
## Quarterly Report



## About the Cover:

The cover depicts the measured surface profile of a cylindrically symmetric echelon fabricated by electron-beam evaporation. A silicon dioxide monolayer is deposited through a discontinuous (stepped) mask profile to deposit a series of annular regions, each increasing in thickness by  $0.53 \mu\text{m}$  from the center (0 thickness) to the edge of the 100-mm-diam substrate (thickness  $12.1 \mu\text{m}$ ). The surface profile was characterized by R. Boni using stitching white-light interferometry on a Zygo NexView.

The figure below exhibits the concentric nature of the echelon steps. Transitions between the individual steps of the echelon display a sloped sidewall of the order of  $150 \mu\text{m}$ , the primary deviation from the ideal design with vertical sidewalls between steps.



This report was prepared as an account of work conducted by the Laboratory for Laser Energetics and sponsored by New York State Energy Research and Development Authority, the University of Rochester, the U.S. Department of Energy, and other agencies. Neither the above-named sponsors nor any of their employees makes any warranty, expressed or implied, or assumes any legal liability or responsibility for the accuracy, completeness, or usefulness of any information, apparatus, product, or process disclosed, or represents that its use would not infringe privately owned rights. Reference herein to any specific commercial product, process, or service by trade name, mark, manufacturer, or otherwise, does not necessarily constitute or imply its endorsement, recommendation, or favoring

by the United States Government or any agency thereof or any other sponsor. Results reported in the LLE Review should not be taken as necessarily final results as they represent active research. The views and opinions of authors expressed herein do not necessarily state or reflect those of any of the above sponsoring entities.

The work described in this volume includes current research at the Laboratory for Laser Energetics, which is supported by New York State Energy Research and Development Authority, the University of Rochester, the U.S. Department of Energy Office of Inertial Confinement Fusion under Cooperative Agreement No. DE-NA0003856, and other agencies.

Printed in the United States of America

Available from  
National Technical Information Services  
U.S. Department of Commerce  
5285 Port Royal Road  
Springfield, VA 22161  
[www.ntis.gov](http://www.ntis.gov)

For questions or comments, contact Katelynn Bauer, Editor, Laboratory for Laser Energetics, 250 East River Road, Rochester, NY 14623-1299, (585) 276-5618.

[www.lle.rochester.edu](http://www.lle.rochester.edu)

# LLE Review



## Quarterly Report

### Contents

<b>IN BRIEF</b> .....	iii
<b>INERTIAL CONFINEMENT FUSION</b>	
Novel Hot-Spot–Ignition Designs for Inertial Confinement Fusion with Liquid Deuterium–Tritium Spheres .....	47
First Observation of Hot-Spot Mix in Laser-Direct-Drive Inertial Confinement Fusion .....	50
<b>PLASMA AND ULTRAFAST PHYSICS</b>	
Anomalous Absorption by the Two-Plasmon–Decay Instability .....	53
<b>HIGH-ENERGY-DENSITY PHYSICS</b>	
X-Ray Diffraction at the National Ignition Facility .....	56
Optimizing Deuterated Metal Foils to Generate a Quasi-Monoenergetic Deuteron Beam on the Multi-Terawatt Laser .....	59
Fully Consistent Density Functional Theory Determination of the Insulator-to-Metal Transition Boundary in Warm Dense Hydrogen .....	62
Thermal Hybrid Exchange-Correlation Density Functional for Improving the Description of Warm Dense Matter .....	64
<b>DIAGNOSTIC SCIENCE AND DETECTORS</b>	
Soft X-Ray Spectrum Unfold of K-Edge–Filtered X-Ray Diode Arrays Using Cubic Splines .....	67
<b>LASER SYSTEM SCIENCE</b>	
Optical Characterization of the OMEGA Beam Profile at High Energy Using the Full-Beam-In-Tank Diagnostic .....	71

**MATERIALS SCIENCE**

Deposition of a Discontinuous Coated Surface to Form a Phase-Stepped Reflected Wavefront ..... 74

Damage Mechanisms in Multilayer Dielectric Gratings at Different Pulse Durations ..... 77

Laser-Induced–Damage Behavior of Novel Glassy Liquid Crystal Materials at 1 ns and Multiple Wavelengths ..... 81

Morphologies and Underlying Mechanisms of Laser-Induced Damage by Model Contamination Particles on a High Reflector ..... 84

Determination of the Raman Polarizability Tensor in the Optically Anisotropic Crystal in Potassium Dihydrogen Phosphate and Its Deuterated Analog ..... 87

Long-Term Monitoring of the Damage Performance of Multilayer Dielectric Grating Samples Residing Inside the Compressor Chamber of the OMEGA EP Laser ..... 91

**LASER FACILITY REPORT**

FY20 Q2 Laser Facility Report ..... 95

**PUBLICATIONS AND CONFERENCE PRESENTATIONS**

## In Brief

This volume of LLE Review 162, covering the period January–March 2020, is sectioned among research areas at LLE and external users of the Omega Laser Facility. Articles appearing in this volume are the principal summarized results of long-form research articles. Readers seeking a more-detailed account of research activities are invited to seek out the primary materials appearing in print, detailed in the publications and presentations section at the end of this volume.

Highlights of research presented in this volume include the following:

- V. N. Goncharov *et al.* propose a new class of ignition designs for inertial confinement fusion. Hydrodynamic simulations demonstrate the feasibility of the new designs and the advantages and disadvantages of the concept compared with more-traditional ICF designs are discussed (p. 47).
- S. P. Regan *et al.* describe quantitatively measuring the amount of hot-spot mix mass in laser-direct-drive inertial confinement fusion implosions of a plastic spherical shell surrounding a layer of cryogenic deuterium–tritium for the first time (p. 50).
- D. Turnbull *et al.* use the laser-plasma simulation environment code to determine a scaling of absorption versus two-plasmon–decay threshold parameter (p. 53). This scaling will help rectify discrepancies that appear at increased intensities.
- J. R. Rygg *et al.* report details of an experimental platform implemented at the National Ignition Facility to obtain *in-situ* powder diffraction data from solids dynamically compressed to extreme pressures (p. 56).
- A. K. Schwemmlin *et al.* induce the target normal sheath acceleration mechanism in deuterated metal foils at intensities close to  $10^{19}$  W/cm<sup>2</sup> using the Multi-Terawatt Laser System (p. 59). It is reported that the total yield depends critically on the surface loading, while the shape of the spectrum is independent of it.
- J. Hinz *et al.* find the insulator-to-metal transition of warm dense fluid hydrogen over a pressure range from 50 to 300 GPa by calculating optical and structural properties from quantum-molecular-dynamics simulations (p. 62).
- D. I. Mihaylov, V. V. Karasiev, and S. X. Hu present theoretical grounds of thermal hybrid exchange-correlation functionals within the generalized Mermin–Kohn–Sham scheme for an improved description of warm dense matter (p. 64).
- D. H. Barnak *et al.* demonstrate a cubic-spline interpolation that provides an alternative analytical way of solving for the temporally and spectrally resolved x-ray flux with no free parameters, assumptions about the geometry, or material of the emitting plasma (p. 67).
- K. A. Bauer *et al.* present the results of early measurements taken with the full-beam-in-tank diagnostic (p. 71). The diagnostic gives new insight into the ability of the OMEGA Laser System to provide uniform fluence profiles that are consistent across all 60 beams in the laser.
- J. B. Oliver *et al.* develop an optical component with a wavelength-scale, stepped-surface relief (p. 74). The methods used and metrology results are shown.

- B. N. Hoffman *et al.* investigate the modifications of multilayer dielectric gratings arising from laser-induced damage using 0.6-ps and 10-ps laser pulses at 1053 nm to better understand the damage-initiation mechanisms (p. 77).
- J. U. Wallace *et al.* describe high laser-induced–damage threshold glassy liquid crystal materials for large-aperture polarization control/beam-smoothing optics that could replace current low-molar-mass liquid crystal devices on the OMEGA Laser System (p. 81).
- K. R. P. Kafka *et al.* investigate the interactions of microparticles of different materials located on the surface of a multilayer dielectric mirror with intense 1053-nm laser pulses of varying fluence and duration (10 ps and 0.6 ps) (p. 84).
- T. Z. Kosc *et al.* present a novel experimental design that enabled the determination of measurement artifacts, including polarization rotation of the pump and/or scattered light propagating through the sample and the contribution of additional overlapping phonon modes (p. 87).
- A. A. Kozlov *et al.* report the results of a damage-testing campaign that monitored representative pulse compression grating samples that were positioned inside the OMEGA EP grating compressor vacuum chamber during normal operation (p. 91).
- J. Puth *et al.* summarize operations of the Omega Laser Facility during the second quarter of FY20 (p. 95).

Katelynn Bauer  
Editor

# Novel Hot-Spot–Ignition Designs for Inertial Confinement Fusion with Liquid Deuterium–Tritium Spheres

V. N. Goncharov, I. V. Igumenshchev, D. R. Harding, S. F. B. Morse, S. X. Hu, P. B. Radha, D. H. Froula, S. P. Regan, T. C. Sangster, and E. M. Campbell

Laboratory for Laser Energetics, University of Rochester

A new class of ignition designs is proposed for inertial confinement fusion (ICF) experiments. These designs are based on the hot-spot–ignition approach, but instead of conventional targets that are comprised of spherical shells with thin frozen deuterium–tritium (DT) layers, a liquid DT sphere inside a wetted-foam shell is used, and the lower-density central region and higher-density shell are created dynamically by appropriately shaping the laser pulse. These offer several advantages, including simplicity in target production (suitable for mass production for inertial fusion energy), absence of the fill tube (leading to a more-symmetric implosion), and lower sensitivity to both laser imprint and physics uncertainty in shock interaction with the ice–vapor interface. The design evolution starts by launching an  $\sim 1$ -Mbar shock into a homogeneous DT sphere. After bouncing from the center, the reflected shock reaches the outer surface of the sphere and the shocked material starts to expand outward until its pressure drops below the ablation pressure. At this point, an adjustment shock is launched inward by supporting ablation pressure.

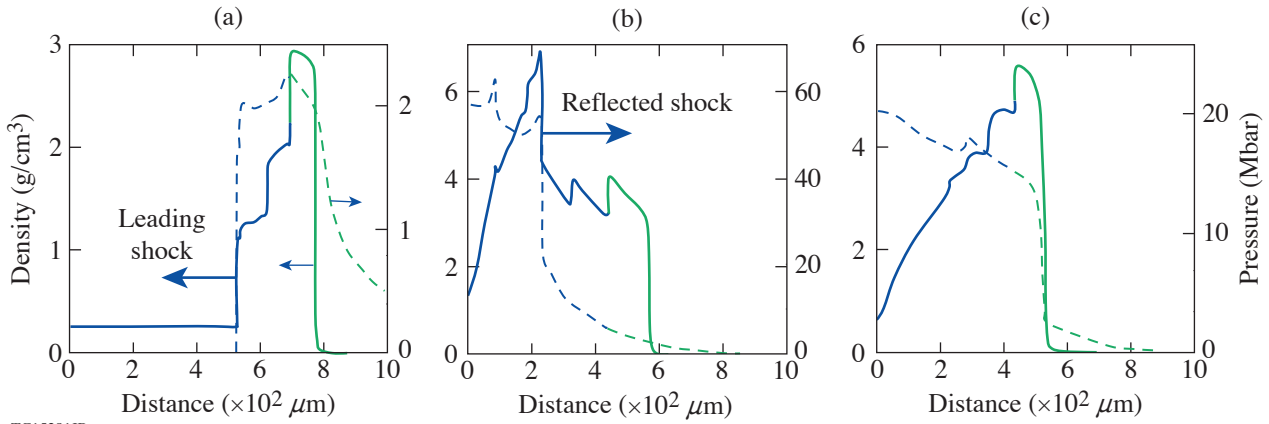
This shock compresses the ablator and fuel, forming a shell. The shell is then accelerated and compressed by appropriately shaping the drive laser pulse, similar to the conventional thin-shell, hot-spot designs. This summary demonstrates the feasibility of the new concept using hydrodynamic simulations and discusses the advantages and disadvantages of the concept compared with more-traditional ICF designs.

The thin-shell cryogenic targets currently used in ICF ignition experiments have several disadvantages: First, fabrication of highly uniform frozen DT layers is time consuming and, in some cases, not reproducible. The layer must be sufficiently uniform to prevent seeding the Rayleigh–Taylor (RT) instability<sup>1</sup> developed during shell acceleration.<sup>2</sup> Even though the beta-layering technique<sup>3</sup> optimized over the last decade has produced smoothness that meets the uniformity specification, the layering process is still time consuming, and different engineering features (such as fill tubes, stalks, and characterization windows in the hohlraum) affect the ice-layer uniformity and lead to degradation in target performance. Second, the physics of relatively strong shocks (a few megabars) interacting with solid material (ablator and DT ice) is not well known. For example, the material phase transition behind the shock could lead to chunks of different phases being present in the shocked ablator and fuel, which contributes to the nonuniformity seeding at the ablator–ice interface and the inner surface of the shell as the first shock breaks out of the shell and material starts to accelerate, forming rarefaction or release. In addition, the physics of spallation or jetting of material from the inner ice surface after shock breakout of the shell is also not well understood and its effect on target performance remains uncertain. Third, laser imprint plays a critical role in determining the nonuniformity seeding in the laser-direct-drive designs.<sup>4,5</sup> Prior to establishing a conduction zone (a region between where the laser energy is deposited and the ablation front) sufficiently large to smooth out the most-damaging modes (typically, these include mode numbers  $\ell > 10$ ), the nonuniformities seeded by laser beam speckles imprint on the target surface.<sup>6</sup> These amplify due to RT instability during acceleration that starts soon after the first shock breaks out of the shell.

Most of these shortcomings can be addressed by imploding liquid DT spheres. These spheres do not require fuel layering, do not have solid–gas interfaces, and have low acceleration during shock propagation through the sphere, preventing significant amplification of early laser imprint. Homogeneous DT spheres have been considered in the past for the volume-ignition approach.<sup>7</sup>

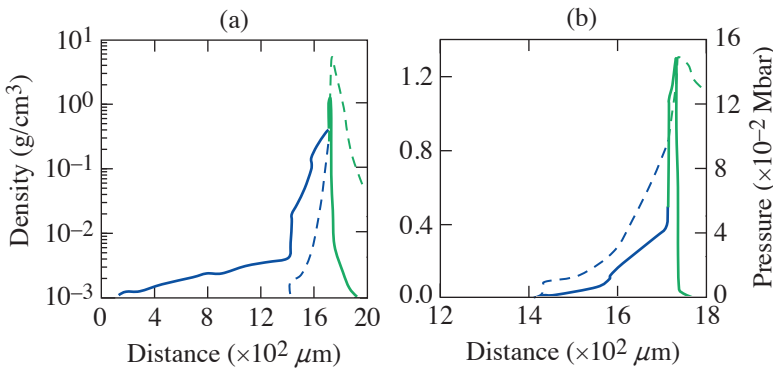
Volume ignition relies mainly on minimizing radiation losses. Such designs require either high-Z shells to trap radiation in the fuel or a large, optically thick fuel mass. The radiation trapping scheme has received a lot of attention in recent publications,<sup>8–10</sup> but the neutron yields predicted in the volume-ignition ICF approach do not significantly exceed gain  $\sim 1$  (see Ref. 11). In addition, such designs require complex targets with multiple shells and buffer layers to mitigate hydrodynamic instability growth.

To illustrate the concept of dynamic shell formation, we consider a 100- $\mu\text{m}$ -thick, 2400- $\mu\text{m}$ -OD CH shell filled with DT fuel at the triple point with a mass density of  $\rho = 0.25 \text{ g/cm}^3$ . This target is driven by a laser pulse with a constant-in-time power of  $P_L = 1 \text{ TW}$ , which corresponds to an on-target overlap incident intensity of  $I \simeq 5.5 \times 10^{12} \text{ W/cm}^2$ . Although the laser wavelength  $\lambda_L = 351 \text{ nm}$  is used in this example, any other laser frequencies will work for the dynamic shell formation since no significant laser-plasma interaction issues are expected at such low overlap intensities. According to 1-D simulations using the hydrodynamic code *LILAC*,<sup>12</sup> the ablation pressure corresponding to these drive conditions is  $P_a = 2 \text{ Mbar}$ . A sequence of hydrodynamic profiles is shown in Figs. 1(a)–1(c). A snapshot of the shell prior to being accelerated is shown in Fig. 2. Next, shell acceleration and fuel compression proceed similarly to the conventional hot-spot designs. An example of the ignition pulse shape is shown in Fig. 3: the total pulse energy is 1.15 MJ. The acceleration part of the pulse has a continuous, 25-ns rise from 0.3 TW to 250 TW. The design reaches  $v_{\text{imp}} = 3.5 \times 10^7 \text{ cm/s}$ , and, when alpha deposition is not included in the calculation, the peak areal density reaches  $\rho R_{\text{peak}} \simeq 2 \text{ g/cm}^2$  and the peak neutron-average pressure is 220 Gbar. When alpha deposition is included, the target ignites and gives a 1-D gain = 75.



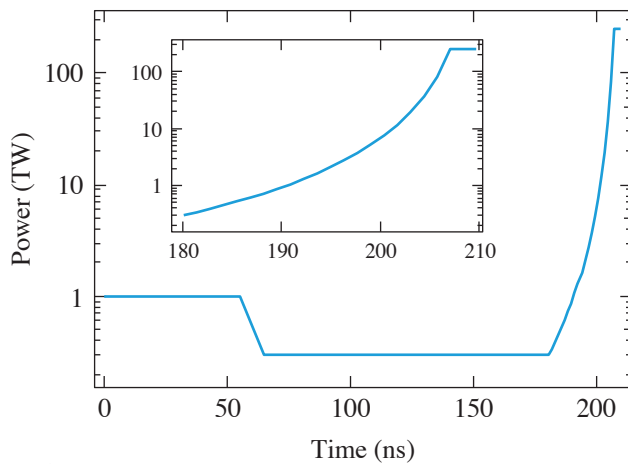
TC15281JR

Figure 1  
Snapshots of density (solid lines) and pressure (dashed lines) profiles at (a)  $t = 35 \text{ ns}$ , (b)  $t = 51 \text{ ns}$ , and (c)  $t = 61 \text{ ns}$ .



TC15283JR

Figure 2  
Dynamically formed shell profiles [(a) linear and (b) logarithmic density scales, respectively] at  $t = 180 \text{ ns}$  for the pulse shown in Fig. 3.



TC15284JR

Figure 3

Pulse shape for the  $E_L = 1.15$ -MJ ignition dynamic-shell design. The inset shows the main drive pulse.

This material is based upon work supported by the Department of Energy National Nuclear Security Administration under Award Number DE-NA0003856, the University of Rochester, and the New York State Energy Research and Development Authority.

1. S. Chandrasekhar, *Hydrodynamic and Hydromagnetic Stability*, International Series of Monographs on Physics (Dover Publications, New York, 1981), Chap. X, p. 428.
2. S. W. Haan *et al.*, *Phys. Plasmas* **18**, 051001 (2011).
3. J. K. Hoffer and L. R. Foreman, *Phys. Rev. Lett.* **60**, 1310 (1988).
4. P. W. McKenty *et al.*, *Phys. Plasmas* **8**, 2315 (2001).
5. S. X. Hu *et al.*, *Phys. Plasmas* **17**, 102706 (2010).
6. V. N. Goncharov *et al.*, *Phys. Plasmas* **7**, 2062 (2000).
7. S. Atzeni and J. Meyer-ter-Vehn, *The Physics of Inertial Fusion: Beam Plasma Interaction, Hydrodynamics, Hot Dense Matter*, 1st ed., International Series of Monographs on Physics, Vol. 125 (Oxford University Press, Oxford, 2004).
8. D. S. Montgomery *et al.*, *Phys. Plasmas* **25**, 092706 (2018).
9. S. X. Hu *et al.*, *Phys. Rev. E* **100**, 063204 (2019).
10. K. Molvig *et al.*, *Phys. Rev. Lett.* **116**, 255003 (2016).
11. M. D. Rosen, *Phys. Plasmas* **6**, 1690 (1999).
12. J. Delettrez *et al.*, *Phys. Rev. A* **36**, 3926 (1987).

# First Observation of Hot-Spot Mix in Laser-Direct-Drive Inertial Confinement Fusion

S. P. Regan,<sup>1</sup> V. N. Goncharov,<sup>1</sup> D. Cao,<sup>1</sup> S. X. Hu,<sup>1</sup> I. V. Igumenshchev,<sup>1</sup> R. Epstein,<sup>1</sup> R. Betti,<sup>1</sup> M. J. Bonino,<sup>1</sup> T. J. B. Collins,<sup>1</sup> M. Farrell,<sup>2</sup> C. J. Forrest,<sup>1</sup> V. Gopalaswamy,<sup>1</sup> V. Yu. Glebov,<sup>1</sup> D. R. Harding,<sup>1</sup> R. T. Janezic,<sup>1</sup> J. P. Knauer,<sup>1</sup> R. W. Luo,<sup>2</sup> O. M. Mannion,<sup>1</sup> J. A. Marozas,<sup>1</sup> F. J. Marshall,<sup>1</sup> D. Patel,<sup>1</sup> P. B. Radha,<sup>1</sup> M. E. Schoff,<sup>2</sup> C. Stoeckl,<sup>1</sup> T. C. Sangster,<sup>1</sup> W. Theobald,<sup>1</sup> and E. M. Campbell<sup>1</sup>

<sup>1</sup>Laboratory for Laser Energetics, University of Rochester

<sup>2</sup>General Atomics

A laser-direct-drive (LDD) inertial confinement fusion (ICF) target<sup>1</sup> has spherical concentric layers consisting of a central region of deuterium (D) and tritium (T) vapor surrounded by a cryogenic DT fuel layer and a thin plastic (CH or CD) ablator material. A spherical implosion driven via the rocket effect from laser ablation of the outer target surface by temporally shaped, high-intensity, overlapping laser beams results in the formation of central hot-spot plasma surrounded by a cold, dense DT shell. Thermonuclear fusion ( $D + T \rightarrow {}^4\text{He} + n$ ) initially occurs in the central hot spot at stagnation, liberating 17.6 MeV per reaction. A long-term goal of ICF is to capture the energy of the alpha particle in the hot spot (i.e., alpha heating) to trigger an ignition instability (i.e., launch a radially outward propagating thermonuclear wave through the surrounding high-density, compressed DT shell), where the fusion energy output is greater than or equal to the laser energy incident on the target. Ignition is predicted to occur when the hot-spot temperature exceeds 5 keV and that compressed areal density exceeds  $0.3 \text{ g/cm}^2$  (Refs. 2–4). Perturbations from the target and laser are amplified by the Richtmyer–Meshkov instability (RMI)<sup>5–7</sup> and the Rayleigh–Taylor instability (RTI),<sup>8–10</sup> which could mix the target layers, degrading the implosion compression, enhancing radiative cooling of the hot spot, and reducing the fusion yield and the compressed areal density. Understanding the physical mechanisms and the seeds of hydrodynamic mixing is of great importance to future LDD ICF targets.<sup>11–15</sup>

The amount of hot-spot mix mass in LDD ICF implosions of a plastic spherical shell surrounding a layer of cryogenic DT has been diagnosed for the first time. Layered DT cryogenic implosion experiments were conducted on the 60-beam, 351-nm, 30-kJ OMEGA laser<sup>16</sup> to determine the dependence of hot-spot mix<sup>17–21</sup> on the design adiabat. For the given target dimensions and composition, the adiabat is determined by the time history of the absorbed laser power and the levels of target preheat by either x rays or energetic electrons. The adiabat is defined as the pressure in the compressed shell divided by the Fermi-degenerate pressure at shell density ( $\alpha = P_{\text{shell}}/P_{\text{Fermi}}$ ). Evolution of instability seeds due to laser imprint<sup>22</sup> and shell and DT-ice nonuniformities, as well as RTI growth factors during shell acceleration<sup>23</sup> depend on the adiabat; therefore, changing the adiabat varies the hydrodynamic stability of the implosion. Although the OMEGA laser is not energetic enough to ignite a target, it is used to study hydrodynamically scaled ignition target designs.<sup>11–14</sup> The implosion adiabat was varied from 2.5 to 12.5 by adjusting the temporal shape of the laser-drive pulse and the Atwood number at the CH/DT material interface [ $A_T = (\rho_{\text{CH}} - \rho_{\text{DT}})/(\rho_{\text{CH}} + \rho_{\text{DT}})$ ] was varied from  $-0.14$  to  $+0.04$  by changing the amount of x-ray preheat of the ablator from the coronal plasma emission. Hot-spot mix can be seeded by debris or imperfections on the target surface,<sup>17–21,24</sup> engineering features [such as the stalk having a  $17\text{-}\mu\text{m}$  outer diameter (OD) or a fill tube with a  $10\text{-}\mu\text{m}$  OD],<sup>24</sup> and laser imprint.<sup>22</sup> These seeds are amplified by the RMI during the shock transit of the shell and are subsequently amplified by the RTI of the ablation front and possibly at the CH/DT material interface during the acceleration phase. Additional mixing of the target layers could occur as the converging shell decelerates and forms a central hot spot.

The amount of hot-spot mix mass in LDD ICF implosions of a plastic spherical shell surrounding a layer of cryogenic DT has been quantitatively measured for the first time. Perturbations from the laser and target are amplified by the RMI during the

shock transit of the shell and by the RTI at the ablation surface and the CH/DT material interface during the acceleration phase and the subsequent deceleration phase. The hydrodynamic mixing of material from the plastic ablator, having trace amounts of Ge for diagnosis, into the hot spot at stagnation was observed and quantified using x-ray spectroscopy on the OMEGA laser and was shown to depend on the implosion adiabat and the Atwood number at the CH/DT material interface, consistent with 2-D radiation-hydrodynamic simulations. Hot-spot mix could degrade implosion compression, enhance radiative cooling of the hot spot, and reduce fusion yield and the compressed areal density in future LDD ignition targets.

The inferred hot-spot mix mass versus calculated adiabat is presented in Fig. 1 with (a) showing the case where the RTI at the ablation front and the DT/CH material interface contribute to the hot-spot mix mass, and (b) showing the case where the RTI at the ablation surface is primarily responsible for the hot-spot mix mass. As can be seen in both of these figures, comparable values of mix mass were inferred on each implosion for the two x-ray spectrometers (XRS) used in the experiment: XRS1 (red symbols) and XRS2 (blue symbols). The reduction in the inferred mix mass with increasing adiabat shown in Fig. 1(b) is consistent with the expectation of a decreased level of mixing as the adiabat is increased and the implosion becomes more stable. The weaker dependence of the inferred mix mass on the adiabat and the higher level of inferred mix mass for the highest-adiabat implosion observed in Fig. 1(a) are attributed to additional mixing from instability growth at the unstable DT-ice/plastic ablator interface. The enhanced level of x-ray preheat for the uniformly doped plastic ablator preheats the plastic ablator and causes the DT-ice/plastic ablator interface to become unstable. The trends observed in the experiment are consistent with 2-D radiation-hydrodynamics simulations.

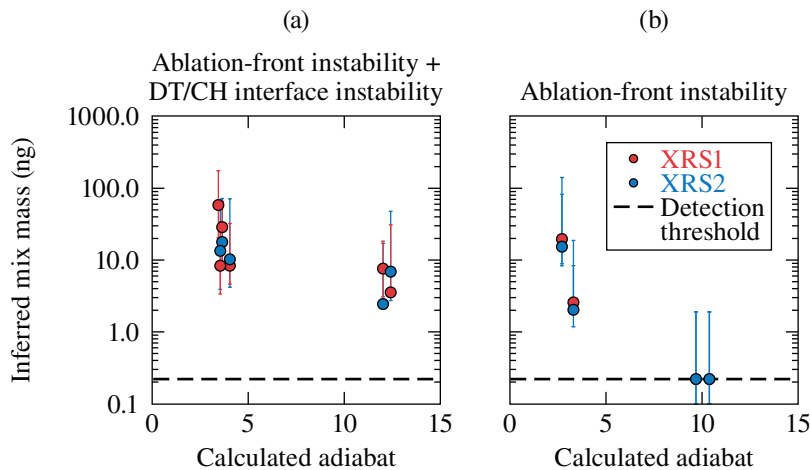


Figure 1

The inferred mix mass for OMEGA DT cryogenic implosions using (a) targets with the 8- $\mu\text{m}$ -thick plastic ablator uniformly doped with Ge, and (b) targets with the inner 3  $\mu\text{m}$  of the 8- $\mu\text{m}$ -thick plastic ablator doped with Ge versus the calculated adiabat. For comparison, the initial CH mass in the shell is 21  $\mu\text{g}$  and the calculated DT mass in the hot spot at stagnation is 1.5  $\mu\text{g}$ .

TC14591JR

This material is based upon work supported by the Department of Energy National Nuclear Security Administration under Award Number DE-NA0003856, the University of Rochester, and the New York State Energy Research and Development Authority.

1. J. Nuckolls *et al.*, *Nature* **239**, 139 (1972).
2. J. D. Lindl *et al.*, *Phys. Plasmas* **11**, 339 (2004).
3. S. Atzeni and J. Meyer-ter-Vehn, *The Physics of Inertial Fusion: Beam Plasma Interaction, Hydrodynamics, Hot Dense Matter*, 1st ed., International Series of Monographs on Physics, Vol. 125 (Oxford University Press, Oxford, 2004).
4. R. Betti *et al.*, *Phys. Plasmas* **9**, 2277 (2002).
5. R. D. Richtmyer, *Commun. Pure. Appl. Math.* **13**, 297 (1960).

6. E. E. Meshkov, *Fluid Dyn.* **4**, 101 (1969).
7. V. N. Goncharov, *Phys. Rev. Lett.* **82**, 2091 (1999).
8. J. W. S. Rayleigh, *The Theory of Sound*, 2nd ed., Vol. 2 (Dover, New York, 1945).
9. G. Taylor, *Proc. R. Soc. London Ser. A* **201**, 192 (1950).
10. A. J. Cole *et al.*, *Nature* **299**, 329 (1982).
11. V. N. Goncharov *et al.*, *Plasma Phys. Control. Fusion* **59**, 014008 (2017).
12. E. M. Campbell *et al.*, *Matter Radiat. Extremes* **2**, 37 (2017).
13. S. P. Regan *et al.*, *Nucl. Fusion* **59**, 032007 (2019).
14. V. Gopaldaswamy *et al.*, *Nature* **565**, 581 (2019).
15. T. J. B. Collins and J. A. Marozas, *Phys. Plasmas* **25**, 072706 (2018).
16. T. R. Boehly *et al.*, *Opt. Commun.* **133**, 495 (1997).
17. B. A. Hammel *et al.*, *Phys. Plasmas* **18**, 056310 (2011).
18. I. V. Igumenshchev *et al.*, *Phys. Plasmas* **20**, 082703 (2013).
19. S. P. Regan *et al.*, *Phys. Plasmas* **19**, 056307 (2012).
20. S. P. Regan *et al.*, *Phys. Rev. Lett.* **111**, 045001 (2013).
21. R. Epstein *et al.*, *AIP Conf. Proc.* **1811**, 190004 (2017).
22. V. A. Smalyuk *et al.*, *Phys. Rev. Lett.* **81**, 5342 (1998).
23. R. Betti *et al.*, *Phys. Plasmas* **5**, 1446 (1998).
24. T. Ma *et al.*, *Phys. Rev. Lett.* **111**, 085004 (2013).

# Anomalous Absorption by the Two-Plasmon–Decay Instability

D. Turnbull,<sup>1</sup> A. V. Maximov,<sup>1,2</sup> D. H. Edgell,<sup>1</sup> W. Seka,<sup>1</sup> R. K. Follett,<sup>1</sup> J. P. Palastro,<sup>1</sup> D. Cao,<sup>1</sup> V. N. Goncharov,<sup>1,2</sup>  
C. Stoeckl,<sup>1</sup> and D. H. Froula<sup>1,3</sup>

<sup>1</sup>Laboratory for Laser Energetics, University of Rochester

<sup>2</sup>Department of Mechanical Engineering, University of Rochester

<sup>3</sup>Department of Physics & Astronomy, University of Rochester

Radiation-hydrodynamic simulations of directly driven fusion experiments at the Omega Laser Facility accurately predict absorption when targets are driven at low overlapped laser intensity. Discrepancies appear at increased intensity, however, with higher-than-expected laser absorption on target. Strong correlations with signatures of the two-plasmon–decay (TPD) instability—including half-harmonic and hard x-ray emission—indicate that TPD is responsible for this anomalous absorption. Scattered-light data suggest that up to ~30% of the laser power reaching quarter-critical density can be absorbed locally when the TPD threshold is exceeded. A scaling of absorption versus TPD threshold parameter was empirically determined and validated using the laser-plasma simulation environment (*LPSE*) code.

The coupling of the laser to directly driven inertial confinement fusion targets is arguably the most fundamental ingredient of such implosions, necessitating accurate models that capture all of the primary laser-absorption processes. In radiation-hydrodynamic simulations (i.e., using the *LILAC* code), the recent transition from a flux-limited thermal transport model to a more-physical nonlocal model revealed significant errors in predicted laser absorption, with more light scattered from the target than expected. This led to the realization that resonant amplification of unabsorbed light leaving the target (i.e., cross-beam energy transfer, or CBET) significantly degrades the laser coupling. Simulation fidelity was improved by the addition of an in-line model describing the instability. This model, however, ostensibly overcompensates—increasing scattered light and reducing shell velocity beyond the level suggested by measurements.

One of the critically important laser–plasma instabilities in OMEGA-scale direct-drive implosions is the TPD instability,<sup>1</sup> in which an incident photon decays into two electron plasma waves near the quarter-critical density surface  $n_c/4$ . Here, we show that the discrepancy between predicted and observed scattered light is a signature of anomalous absorption of laser light due to the excitation of TPD. Over a wide range of laser intensities spanning the typical design space of implosions on OMEGA, the time-dependent absorption difference is shown to be strongly correlated with the time history of TPD activity, which was diagnosed using half-harmonic emission. The data suggest that ~15% to 20% of the laser light reaching  $n_c/4$  is typically absorbed when TPD is active, which significantly modifies the coronal plasma energetics of implosions on OMEGA.

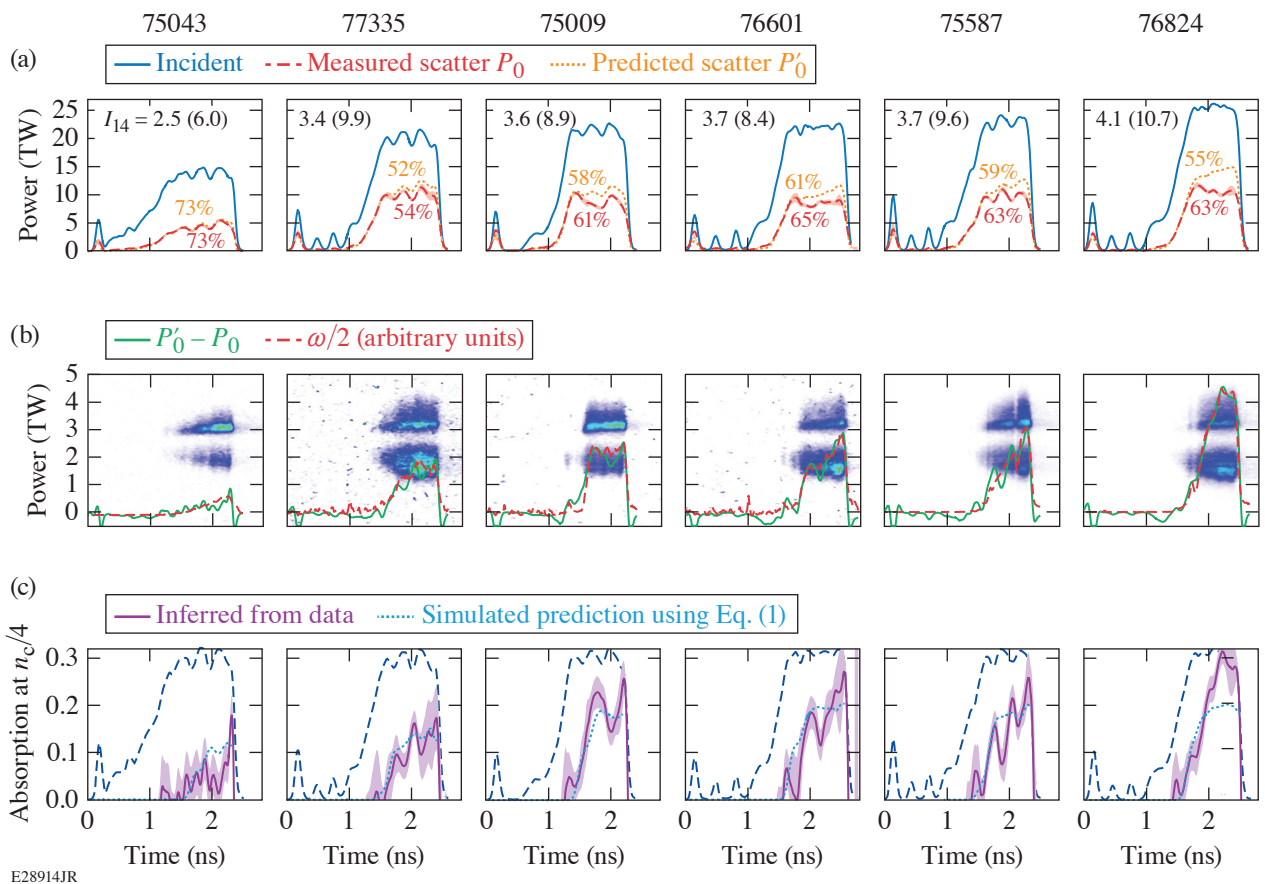
The basic mechanism is as follows: The incident lasers transfer energy to the coronal plasma through electron–ion collisions. Between approximately 10% and 50% of the critical density, the incident light is also coupled to the outgoing light by CBET. When the ingoing rays reach their turning point, the photons that have not yet been absorbed get reflected. Upon re-entering the CBET-active region, this outgoing light becomes the seed that is amplified by CBET. When some fraction of the incident laser light is absorbed near  $n_c/4$  due to TPD, the power at every point thereafter will be reduced by approximately that fraction, including the net power out.

Figure 1(a) shows the total incident laser power for six different implosions along with the scattered light predicted by *LILAC* (using the nonlocal and CBET models) and the measured scattered light. The time-integrated coupling percentage is included

for both the simulations and the experiments, with differences as large as 8% (shot 76824). Also noted is the average quarter-critical overlapped intensity during the peak according to *LILAC* (ranging from  $I_{14} = 2.5$  to 4.1 in units of  $10^{14}$  W/cm<sup>2</sup>) and the associated vacuum hard-sphere intensities (6.0 to 10.7). The examples shown are emblematic of the systematic trends evident in the broader absorption database. At low overlapped intensity (e.g., shot 75043), there is excellent agreement between predicted and observed scattered light. At higher quarter-critical intensity, however, they tend to diverge at some point during peak power.

In search of qualitative correlation between the apparent error in scattered light and TPD, the time-resolved difference between the predicted and observed scattered light was plotted [see Fig. 1(b)] against the time history of half-harmonic emission—a spectral doublet centered around 702 nm that is known to be a signature of TPD.<sup>1</sup> The agreement in terms of onset, timing, and overall shape is generally remarkable.

Assuming the decrease in total scattered power is dominated by the reduction of the unabsorbed light seed, the ratio of scattered power with TPD (i.e., the experimental result) to scattered power without TPD (i.e., the simulated result) is a direct measurement of the transmission  $T$  past  $n_c/4$ , and absorption is simply  $A_{n_c/4} = 1 - T$  [Fig. 1(c)]. Typical incident power levels yield absorption in the range of 10% to 25%. Such levels are consistent with the conclusions drawn from electron-temperature measurements of the quarter-critical region based on half-harmonic emission.<sup>2</sup>



E28914JR

Figure 1

Use of scattered light data to infer anomalous absorption due to TPD. (a) From left to right, peak power increases along with overlapped intensity at quarter-critical density. During peak power, scattered-light data are increasingly divergent from the simulated predictions as quarter-critical intensity increases. (b) The difference between predicted and observed scattered light correlates extremely well with half-harmonic emission, indicating the discrepancy is associated with TPD. (c) Assuming that anomalous absorption by TPD primarily reduces the unabsorbed light seed for CBET, absorption at  $n_c/4$  due to TPD is typically found to be in the range of ~10% to 25%. The absorption time dependence can be predicted inline using parameters in *LILAC* along with Eq. (1).

It would be useful to have an in-line model for enhanced TPD absorption that does not rely on experimental measurements *a posteriori*; inferring an appropriate scaling for such a reduced model is a main goal of this work. TPD activity has previously been shown to scale with the Simon threshold parameter  $\eta = I_{14}L/(233 T_e)$ , with the density gradient scale length  $L$  in  $\mu\text{m}$ , electron temperature  $T_e$  in keV, and laser intensity specified at  $n_c/4$ . For each of the shots in Fig. 1 (highlighted in blue) as well as 11 other shots from the same 2014–2015 time period,  $\eta(t)$  was extracted from the *LILAC* simulations and plotted against the inferred absorption. Figure 2 shows the inferred scaling of anomalous TPD absorption versus TPD threshold parameter. Above a threshold at  $\eta = 0.71$ , the data are well fit by the power law

$$A_{n_c/4} = 0.248 - 0.061\eta^{-4}. \quad (1)$$

Convolving the simulated Simon threshold parameter with an appropriate response function and then applying the above scaling yields an estimated absorption using the code parameters for direct comparison to the data on an individual shot. The results, included in Fig. 1(c), generally track the data well. This should, therefore, be a good starting point for a reduced model that can be included inline in radiation-hydrodynamic simulations.

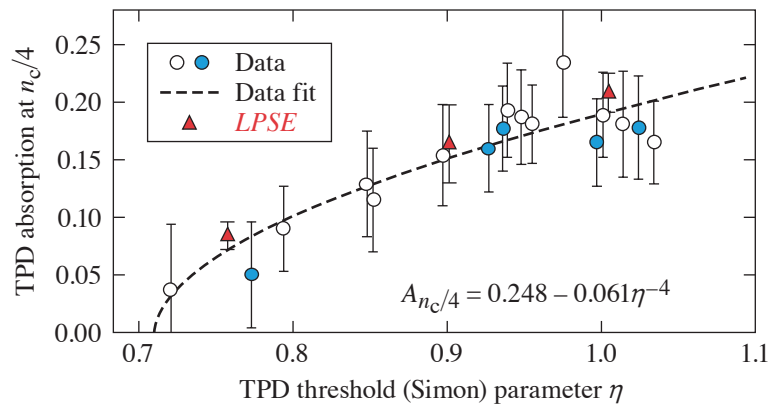


Figure 2

A trend of inferred absorption versus the Simon threshold parameter extracted from simulations is found using the average values from a wide range of shots with differing drive conditions. Typically, conditions during peak power are  $\sim 20\%$  to  $30\%$  above the TPD threshold, resulting in  $\sim 15\%$  to  $20\%$  local absorption at  $n_c/4$ . Two-dimensional *LPSE* simulations accurately reproduce both the threshold and the scaling above threshold.

To validate the empirical scaling, 2-D simulations were run using *LPSE*. Notably, a new pump-depletion model was used that self-consistently evolves the electromagnetic field of the laser as power is pumped into electron plasma waves. Figure 2 shows that *LPSE*'s predictions for TPD absorption are in very good agreement with the data. The use of a speckled beam was found to be essential in reproducing both the threshold and the scaling above threshold because individual intense speckles become unstable below  $\eta = 1$ , while other parts of the beam remain below threshold. Critically, the simulations found that  $5\times$  to  $8.3\times$  more power is dissipated by collisional (rather than Landau) damping, which explains why such large laser absorption does not result in undue levels of hot electrons—most of the power is thermalized around  $n_c/4$ .

This material is based upon work supported by the Department of Energy National Nuclear Security Administration under Award Number DE-NA0003856, the University of Rochester, and the New York State Energy Research and Development Authority.

1. W. Seka *et al.*, Phys. Plasmas **16**, 052701 (2009).
2. W. Seka *et al.*, Phys. Rev. Lett. **112**, 145001 (2014).

## X-Ray Diffraction at the National Ignition Facility

J. R. Rygg,<sup>1,2,3,4</sup> R. F. Smith,<sup>4</sup> A. E. Lazicki,<sup>4</sup> D. G. Braun,<sup>4</sup> D. E. Fratanduono,<sup>4</sup> R. G. Kraus,<sup>4</sup> J. M. McNaney,<sup>4</sup> D. C. Swift,<sup>4</sup> C. E. Wehrenberg,<sup>4</sup> F. Coppari,<sup>4</sup> M. F. Ahmed,<sup>4</sup> M. A. Barrios,<sup>4</sup> K. J. M. Blobaum,<sup>4</sup> G. W. Collins,<sup>1,2,3,4</sup> A. L. Cook,<sup>4</sup> P. Di Nicola,<sup>4</sup> E. G. Dzenitis,<sup>4</sup> S. Gonzales,<sup>4</sup> B. F. Heidl,<sup>4</sup> M. Hohenberger,<sup>4</sup> A. House,<sup>4</sup> N. Izumi,<sup>4</sup> D. H. Kalantar,<sup>4</sup> S. F. Khan,<sup>4</sup> T. R. Kohut,<sup>4</sup> C. Kumar,<sup>4</sup> N. D. Masters,<sup>4</sup> D. N. Polsin,<sup>1</sup> S. P. Regan,<sup>1,2</sup> C. A. Smith,<sup>4</sup> R. M. Vignes,<sup>4</sup> M. A. Wall,<sup>4</sup> J. Ward,<sup>4</sup> J. S. Wark,<sup>5</sup> T. L. Zobrist,<sup>4</sup> A. Arsenlis,<sup>4</sup> and J. H. Eggert<sup>4</sup>

<sup>1</sup>Laboratory for Laser Energetics, University of Rochester

<sup>2</sup>Department of Mechanical Engineering, University of Rochester

<sup>3</sup>Department of Physics & Astronomy, University of Rochester

<sup>4</sup>Lawrence Livermore National Laboratory

<sup>5</sup>Department of Physics, Clarendon Laboratory, University of Oxford

The behavior of matter depends strongly on the particular structure or arrangement of the constituent atoms, which provides a fundamental basis for understanding the mechanical, electronic, magnetic, and thermodynamic properties. For over a century, x-ray diffraction (XRD) has been a workhorse technique to measure the atomic arrangement of matter, leading to numerous scientific discoveries and materials understanding. The powder x-ray diffraction image plate (PXRDIP) platform<sup>1</sup>—first deployed at the Omega Laser Facility in 2009—brought XRD to the frontier of high-pressure research at large laser facilities. It has been used on over 100 OMEGA and OMEGA EP campaigns to record x-ray diffraction from matter compressed to extreme pressures and discover new phases in a variety of materials.<sup>2–7</sup>

A variant of the OMEGA XRD platform, now implemented at the National Ignition Facility (NIF) [Fig. 1(a), Ref. 8], takes advantage of the additional energy and longer pulse durations to compress samples to even more extreme conditions up to 2 TPa (1 TPa = 10 Mbar  $\approx$  10 million atm), and to flash even brighter x-ray sources for x-ray diffraction on thicker samples and with shorter wavelengths.

Common to the XRD platforms at both the Omega Laser Facility and the NIF, a sample of interest is sandwiched between tamper layers and compressed to a uniform, high-pressure state by direct laser drive of the sample assembly. The pressure history in the sample is measured using high-precision velocimetry [velocity interferometer system for any reflector (VISAR)]. The sample is then irradiated while at peak pressure by up to two bursts of K-shell emission from separate laser-driven foils. The angular distribution of x rays scattered from a portion of the sample restricted by a pinhole aperture is recorded on x-ray-sensitive detectors covering approximately  $1.5\pi$  steradians [Fig. 1(b)].

Several improvements to the platform setup and data analysis have been implemented, many of which are applicable to both the OMEGA and NIF diffraction platforms. Pressure uniformity better than 3% ( $1\sigma$ ) in both the longitudinal and transverse dimensions has been demonstrated for compressed samples at the time of exposure to x rays. The mean sample pressure during exposure can be determined in some cases with 1% precision, depending mostly on the velocimeter sensitivity, and 3% accuracy, depending mostly on the high-pressure characterization of the VISAR-side tamper layer. The diffracted signal is determined with a typical  $2\theta$  x-ray scattering angle precision of about  $0.2^\circ$  and resolution of about  $1^\circ$ . Analytic expressions have been derived for systematic corrections to  $2\theta$  due to finite pinhole size and sample offset. A density accuracy of better than six parts per thousand has been demonstrated on the NIF using an undriven lead sample.

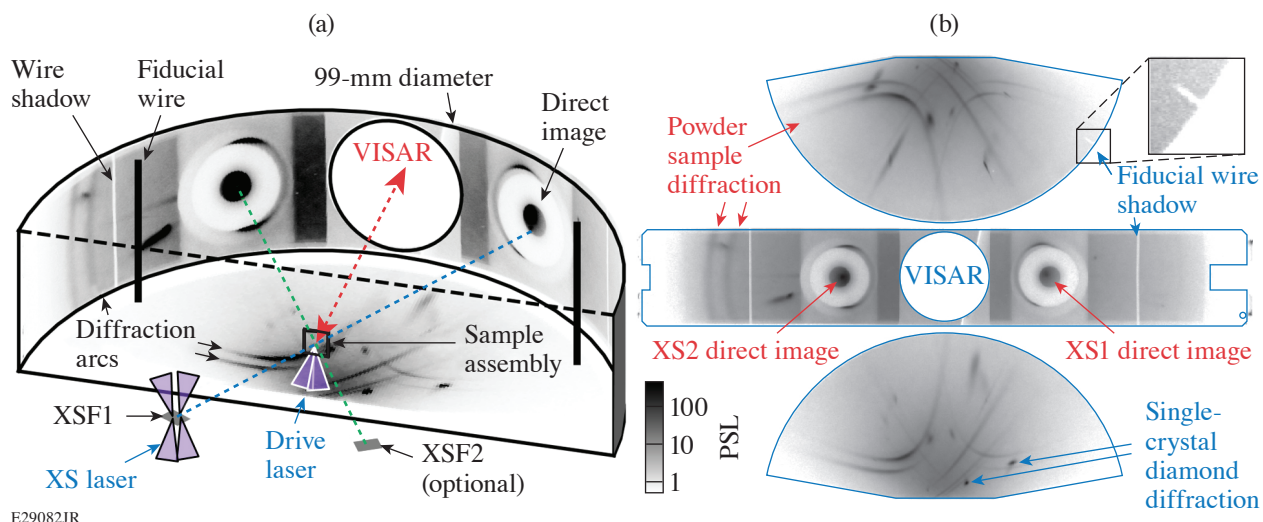


Figure 1

(a) The NIF x-ray diffraction platform involves ramp compression of the sample assembly using temporally shaped NIF laser drive beams. One, or optionally two, x-ray source foils (XSF's) are driven by additional (XS) beams to generate an x-ray pulse that diffracts from the compressed sample and is recorded on image plates lining the inside of a 99-mm-diam cylinder. A hole-in-one image plate allows for simultaneous velocimetry of the sample assembly using the VISAR diagnostic, and fiducial wires are used to cross-register the location of the image plates for improved precision. (b) Image plate scans for N160517-003, a dual-XS exposure of platinum compressed to 200 GPa.

The high laser energy (up to 200 kJ) used on the NIF for driving the target and the x-ray sources leads to an extremely high background on the image-plate detectors, particularly for drive pressures exceeding 1 TPa. Significant shielding improvements were implemented on the NIF, some of which were adapted to Omega's PXRDIIP platform. In addition, a recently developed variant of a nonlinear 2-D background subtraction algorithm has been used to isolate and detect diffraction lines at signal-to-background ratios as low as a few percent. This background subtraction method may be useful for other diagnostics that have a high and nonuniform background.

An improved model for the system response over the detector area has been constructed to permit compensation of the data signal based on local sensitivity in order to obtain accurate diffraction line intensities. This system response calculation includes a new analytic approximation for image-plate sensitivity as a function of photon energy (up to 100 keV) and incident angle that can be directly applied to other diagnostics using image plates at non-normal incidence angle.

These x-ray diffraction platforms have been used to (1) measure the density-pressure equation of state and determine the crystal structure of a variety of materials, including discovery of several new phases; (2) evaluate the strain-induced texturing or de-texturing after some phase transitions; and (3) verify solidity and observe liquid phases, thereby examining the melt line at high pressure. Dual x-ray probes unlock new exploration of the kinetics of phase transitions at nanosecond time scales, including hysteresis and the strain-rate dependence of phase boundaries. Manuscripts describing new diffraction results on several materials compressed up to 2 TPa are currently in preparation. Over the last century, x-ray diffraction has been an invaluable tool for probing and understanding materials, and we are pleased to push this capability toward the current frontier of high-pressure science.

This work was largely performed under the auspices of the U.S. Department of Energy by Lawrence Livermore National Laboratory under Contract No. DE-AC52-07NA27344. A portion of this material is based upon work supported by the Department of Energy National Nuclear Security Administration under Award Number DE-NA0003856, the University of Rochester, and the New York State Energy Research and Development Authority.

1. J. R. Rygg *et al.*, *Rev. Sci. Instrum.* **83**, 113904 (2012).
2. F. Coppari *et al.*, *Nat. Geosci.* **6**, 926 (2013).
3. A. Lazicki *et al.*, *Phys. Rev. Lett.* **115**, 075502 (2015).
4. J. Wang *et al.*, *Phys. Rev. B* **94**, 104102 (2016).
5. D. N. Polsin *et al.*, *Phys. Rev. Lett.* **119**, 175702 (2017).
6. J. K. Wicks *et al.*, *Sci. Adv.* **4**, eaao5864 (2018).
7. M. Millot *et al.*, *Nature* **569**, 251 (2019).
8. J. R. Rygg *et al.*, *Rev. Sci. Instrum.* **91**, 043902 (2020).

# Optimizing Deuterated Metal Foils to Generate a Quasi-Monoenergetic Deuteron Beam on the Multi-Terawatt Laser

A. K. Schwemmlin,<sup>1,2</sup> C. Stoeckl,<sup>1</sup> W. T. Shmayda,<sup>1</sup> and W. U. Schröder<sup>1,2,3</sup>

<sup>1</sup>Laboratory for Laser Energetics, University of Rochester

<sup>2</sup>Department of Physics and Astronomy, University of Rochester

<sup>3</sup>Department of Chemistry, University of Rochester

The Multi-Terawatt (MTW) Laser System at LLE was used to study the target normal sheath acceleration (TNSA) mechanism in deuterated metal foils at intensities close to  $10^{19}$  W/cm<sup>2</sup>. Deuteron beams were previously generated with this mechanism using either plastic<sup>1</sup> or heavy-water<sup>2,3</sup> targets. While plastic targets promise simple handling, they offer poor beam quality; on the other hand, heavy-water targets yield higher beam quality but require careful handling. Deuterated metal foils provide a reasonable compromise between ease of handling and beam quality. In addition, certain metals such as titanium have a high capacity for storing hydrogen in the form of hydrides.<sup>4</sup>

A first batch of targets was prepared by exposing  $500 \times 500 \times 25\text{-}\mu\text{m}^3$  titanium foils to 1 mTorr of atomic deuterium ( $D^0$ ) generated by a glowing tungsten filament in a deuterium atmosphere for varying amounts of time. The second batch was formed by depositing titanium onto titanium substrates in a deuterium atmosphere.

A total of 50 deuterated metal targets were shot to create a survey of deuteron beam characteristics as a function of surface loading. The spectra of all emitted ions were measured using the Thomson parabola ion spectrometer.<sup>5</sup> Remarkably, the deuterons had a quasi-monoenergetic spectrum well approximated by a Gaussian (see Fig. 1). This unusual TNSA spectrum was predicted in literature<sup>6</sup> for heavy target substrates. Heavy atoms remain almost stationary during the TNSA process, generating a nearly static electric field that uniformly accelerates light ions. All fielded targets produced this Gaussian energy spectrum, regardless of loading type, with a very consistent mean beam energy and width of  $0.8 \pm 0.6$  MeV.

Total yields ranged from low- $10^{10}$  to mid- $10^{11}$  deuterons per shot, depending critically on the surface loading. Figure 2 shows that there is an increase in deuterium yield with titanium thickness for targets onto which titanium was evaporated under a  $D^0$  atmosphere. On the other hand, there was no increase in yield with  $D^0$  exposure time for targets that were simply exposed to  $D^0$ . Comparing yields across the batches, simple  $D^0$  exposure for 22 h proved more effective than condensing  $1\ \mu\text{m}$  of titanium on titanium in the presence of  $D^0$ . Consequently, the total deuterium yield of an evaporatively loaded target increases with TiD thickness, but diffusively loaded targets always produce higher yields within the parameter space evaluated. However, this higher yield cannot be increased further by longer exposure times. In future experiments, titanium targets will be exposed to atomic tritium ( $T^0$ ) for 24 h to produce a tritium beam that will be used to study nuclear reaction rates relevant for stellar nucleosynthesis.

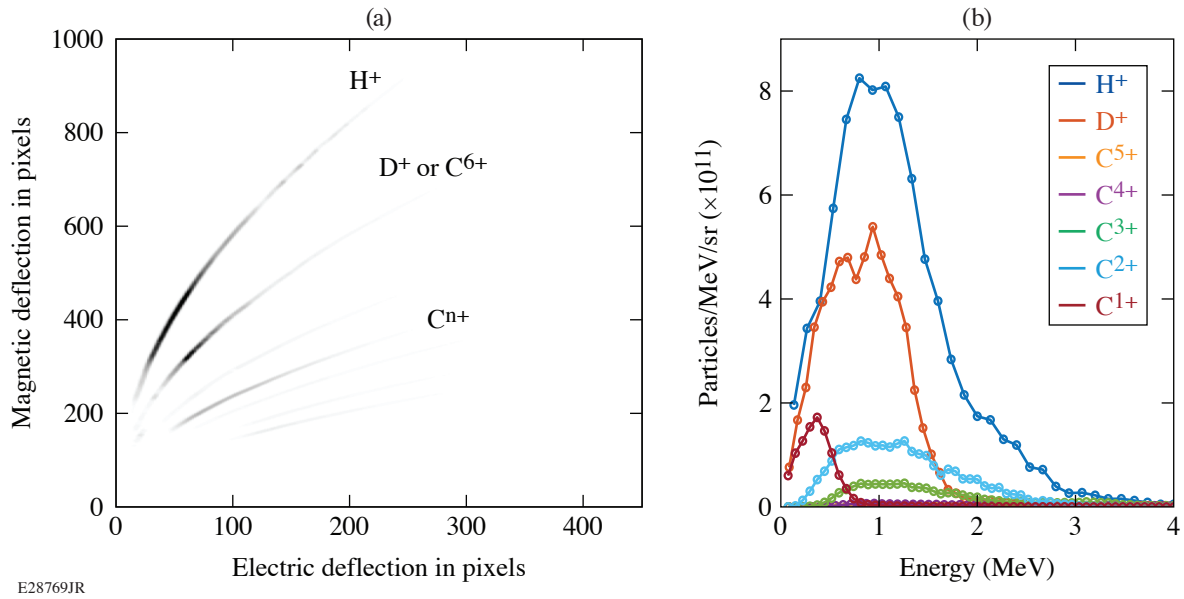


Figure 1  
Data for one shot using a Ti-backed target exposed to D<sup>0</sup> for 98 h: (a) the digitized image plate and (b) the corresponding Thomson parabola spectra for each trace. Note the peaked deuteron spectrum.

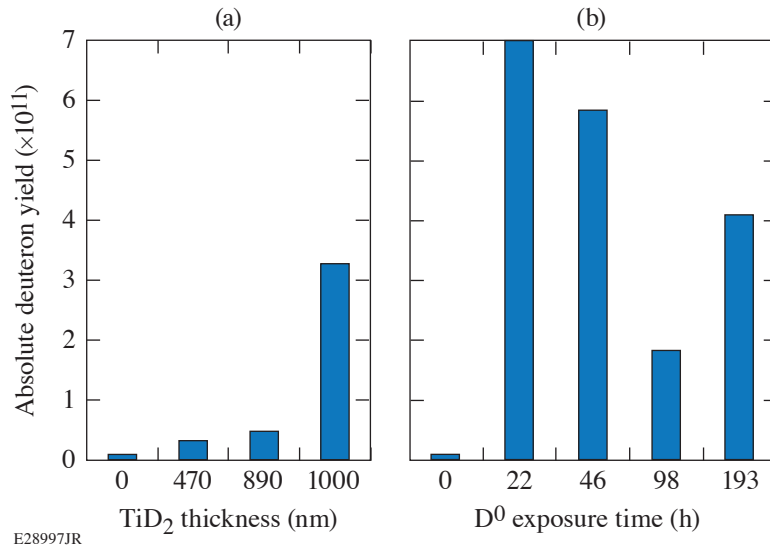


Figure 2  
The absolute deuteron yields for the two different batches. (a) Targets onto which Ti was evaporated under a D<sup>0</sup> atmosphere. An increase of yield with thickness is evident. (b) Targets exposed to a D<sup>0</sup> atmosphere. Since there is no increase in yield with exposure time, it is concluded that saturation occurs quickly. Atomic deuterium exposure is clearly the more-effective loading method.

This material is based upon work supported by the Department of Energy National Nuclear Security Administration under Award Number DE-NA0003856, the University of Rochester, and the New York State Energy Research and Development Authority.

1. L. Torrisi *et al.*, Phys. Scr. **T161**, 014026 (2014).
2. J. T. Morrison *et al.*, Phys. Plasmas **19**, 030707 (2012).
3. S. Karsch *et al.*, Phys. Rev. Lett. **91**, 015001 (2003).
4. W. M. Mueller, J. P. Blackledge, and G. G. Libowitz, *Metal Hydrides* (Academic Press, New York, 1968).
5. C. C. Freeman *et al.*, Rev. Sci. Instrum. **82**, 073301 (2011).
6. T. Zh. Esirkepov *et al.*, Phys. Rev. Lett. **89**, 175003 (2002).

# Fully Consistent Density Functional Theory Determination of the Insulator-to-Metal Transition Boundary in Warm Dense Hydrogen

J. Hinz,<sup>1</sup> V. V. Karasiev,<sup>1</sup> S. X. Hu,<sup>1</sup> M. Zaghoo,<sup>1</sup> D. Mejía-Rodríguez,<sup>2</sup> S. B. Trickey,<sup>2</sup> and L. Calderín<sup>3</sup>

<sup>1</sup>Laboratory for Laser Energetics, University of Rochester

<sup>2</sup>Quantum Theory Project, Department of Physics, University of Florida

<sup>3</sup>Department of Materials Science and Engineering, University of Arizona

The liquid–liquid insulator-to-metal transition (IMT) of warm dense hydrogen isotopes is a crucial phenomenon for giant planet structure and dynamics. Because hydrogen has the highest relative abundance in the universe, accurate determination of the IMT is key to modeling the interior dynamics and evolution of these Jovian-like planets.<sup>1</sup> An essential prerequisite for quantitative models is an accurate equation of state (EOS) that correctly describes both the onset and character of the IMT.<sup>2</sup> Independent of planetary physics, an accurate EOS for hydrogen and its isotopes is also essential for progress in inertial confinement fusion research.<sup>3</sup>

Despite its importance, accurate determination of the IMT boundary remains an experimental and theoretical/computational challenge. In this work we make a major step forward on the theory/computation side by providing a single, conceptually consistent density functional theory (DFT) treatment, with the best-balanced modern approximate exchange–correlation (XC) functional, namely SCAN-L with the nonlocal correlation correction rVV10. We provide results both with and without nuclear quantum effects (NQE's) that are mostly consistent with experimental findings and with best-available combinations of DFT and stochastic methods.

With the use of quantum molecular dynamic simulations, we probe warm dense fluid hydrogen from 60 to 320 GPa across a temperature range of 600 to 3000 K. Both classical nuclei, within the Born–Oppenheimer approximation, and quantum nuclei, as treated within the path integral formalism, are considered. In all cases the electrons are treated quantum mechanically within the finite temperature extension of DFT. The bulk system of fluid hydrogen is approximated with the use of a 256-atom system in a periodic cubic supercell maintained in a canonical ensemble with fixed particle number, temperature, and volume.

Analysis of the dc conductivity and reflectivity, calculated via the Kubo–Greenwood formalism, along with the extraction of the indirect band gap and ionic pair correlation function, shows concurrent abrupt changes at the onset of a minimum metallic behavior of 2000 S/cm. With the inclusion of nuclear quantum effects, the molecular character of the system is significantly diminished prior to the onset of metallization. This in turn sharpens the abrupt changes in the aforementioned properties and produces a shift in excess of 250 K in the IMT boundary location. Furthermore, the inclusion of NQE's produces an explicit isotope effect in the form of clear splitting in the hydrogen and deuterium IMT boundaries (see Fig. 1).

In summary, we have re-examined the problem of determining the IMT boundary of warm dense fluid hydrogen with consistent use of what is arguably the best approximate XC functional currently available for treating both molecular and condensed phase systems evenhandedly. The resulting hydrogen IMT boundary is in good agreement with experimental measurements across a wide range of pressures and temperatures. Our analysis supports the notion of a metallic transition driven by an abrupt band-gap closure associated with the dissociation of molecular to atom hydrogen.

This work was supported by the Department of Energy National Nuclear Security Administration Award Number DE-NA0003856 and U.S. National Science Foundation PHY Grant No. 1802964. D. Mejía-Rodríguez and S. B. Trickey acknowledge support by U.S. Department of Energy grant DE-SC 0002139. All computations were performed on the LLE high-performance computing systems.

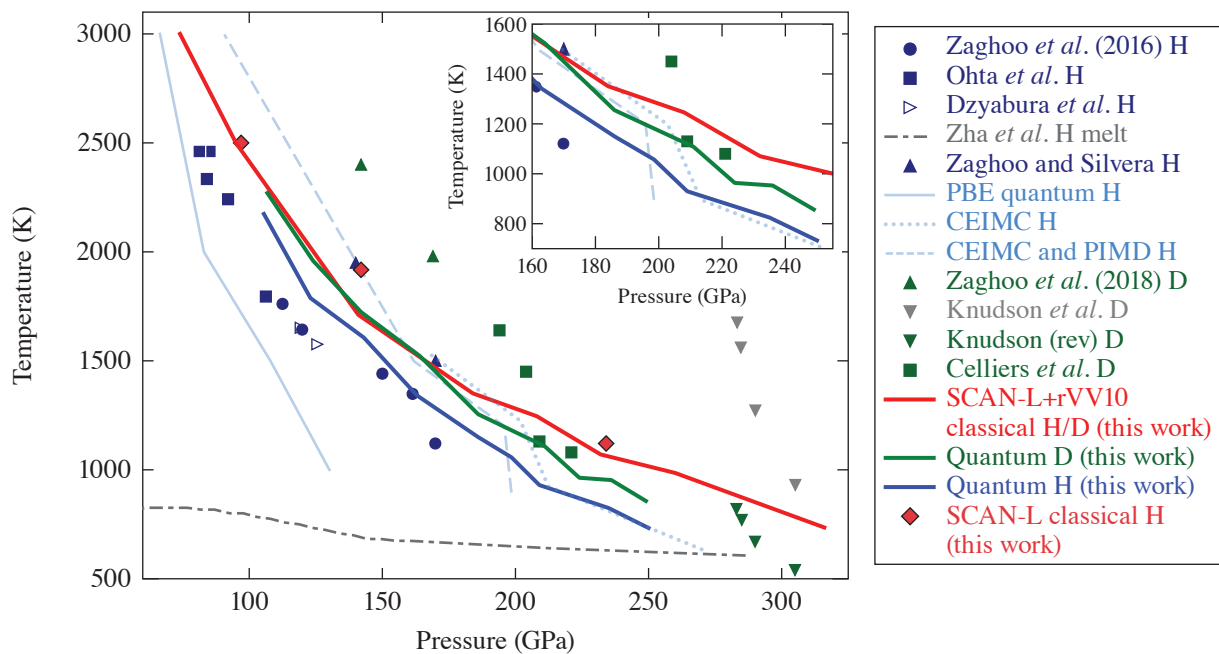


Figure 1

Emerging picture of the hydrogen and deuterium IMT. Blue symbols show experimental results for hydrogen.<sup>2–5</sup> Upright blue triangles are the IMT from measured reflectivities.<sup>5</sup> All others are from the laser-heating curve plateau. Green symbols show reflectivity results for deuterium.<sup>6–8</sup> The dashed–dotted gray curve is the melt line based on Ref. 9. All other solid IMT curves are theoretical predictions. The red curve is the SCAN-L + rVV10 prediction with classical nuclei, and the red diamonds are three of the same classical nuclei predictions without the rVV10 correction. The corresponding blue and green curves are the predictions with NQE's for hydrogen and deuterium, respectively. Inset: With NQE inclusion, an apparent step in the IMT boundary appears. This feature has not been seen previously in DFT studies. Further analysis is required to ascertain the underlying cause of that feature.

1. G. Mazzola, R. Helled, and S. Sorella, Phys. Rev. Lett. **120**, 025701 (2018).
2. K. Ohta *et al.*, Sci. Rep. **5**, 16560 (2015).
3. M. Zaghoo, A. Salamat, and I. F. Silvera, Phys. Rev. B **93**, 155128 (2016).
4. V. Dzyabura, M. Zaghoo, and I. F. Silvera, Proc. Natl. Acad. Sci. **110**, 8040 (2013).
5. M. Zaghoo and I. F. Silvera, Proc. Natl. Acad. Sci. **114**, 11,873 (2017).
6. M. Zaghoo, R. J. Husband, and I. F. Silvera, Phys. Rev. B **98**, 104102 (2018).
7. M. D. Knudson *et al.*, Science **348**, 1455 (2015).
8. P. M. Celliers *et al.*, Science **361**, 677 (2018).
9. C. S. Zha *et al.*, Phys. Rev. Lett. **119**, 075302 (2017).

# Thermal Hybrid Exchange-Correlation Density Functional for Improving the Description of Warm Dense Matter

D. I. Mihaylov, V. V. Karasiev, and S. X. Hu

Laboratory for Laser Energetics, University of Rochester

The warm-dense-matter (WDM) regime is too hot for standard condensed-matter approaches; however, quantum many-body effects are strong and classical plasma physics are not applicable. An established standard approach for accurate treatment of WDM is *ab initio* molecular dynamics (AIMD), when classical treatment for ions is combined with finite-temperature density functional theory (FT-DFT) for electronic degrees of freedom. Currently, all available exchange-correlation (XC) functionals in commonly used DFT software packages are ground-state functionals that do not explicitly depend on  $T$  but are evaluated at the  $T$ -dependent self-consistent density, i.e.,  $F_{XC}[n(T), T] \approx E_{XC}[n(T)]$ —an approach known as the ground-state approximation (GSA). Previously developed thermal functionals belong to the local density approximation (LDA) and generalized gradient approximation (GGA) level of refinement. At the LDA level, Karasiev *et al.* developed the nonempirical, thermal functional KSDT<sup>1</sup> (and its corrected version, corrKSDT; see Ref. 2), which is based on parameterized path-integral Monte Carlo data for the homogeneous electron gas at finite  $T$  and, in the zero- $T$  limit, reduces to the ground-state Perdew–Zunger (PZ) functional. Subsequently, driven by the need to incorporate density-gradient effects and thereby account for the nonhomogeneity of the system, Karasiev *et al.* developed the GGA-level thermal functional KDT16 (Ref. 2) by analyzing the gradient expansion of weakly inhomogeneous electrons at finite  $T$  and defining appropriate  $T$ -dependent reduced variables for  $X$  and  $C$ . KDT16 is, by construction, nonempirical and reduces to the popular Perdew–Burke–Ernzerhof (PBE) functional in the zero- $T$  limit. An example of the improved accuracy provided by the KDT16 functional was recently reported in Ref. 3, where KDT16-based AIMD studies of shocked deuterium showed improved agreement with experimental measurements of Hugoniot, reflectivity, and dc conductivity at elevated  $T$ . While it is clear that corrKSDT and KDT16 provide an apparent improvement over their ground-state counterparts PZ and PBE, they suffer from an inherent fundamental drawback—underestimating the electronic band gap. Hybrid XC functionals such as PBE0<sup>4</sup> are constructed by mixing DFT XC functionals with Hartree–Fock (HF) exact exchange (EXX) and are known to be superior to GGA’s in predicting quantities such as  $E_{\text{gap}}$ , atomization energy, bond length, and vibrational frequency. In this work we present the KDT0 thermal hybrid model, which is based on a mixture of finite- $T$  HF  $X$  and thermal KDT16 GGA XC:

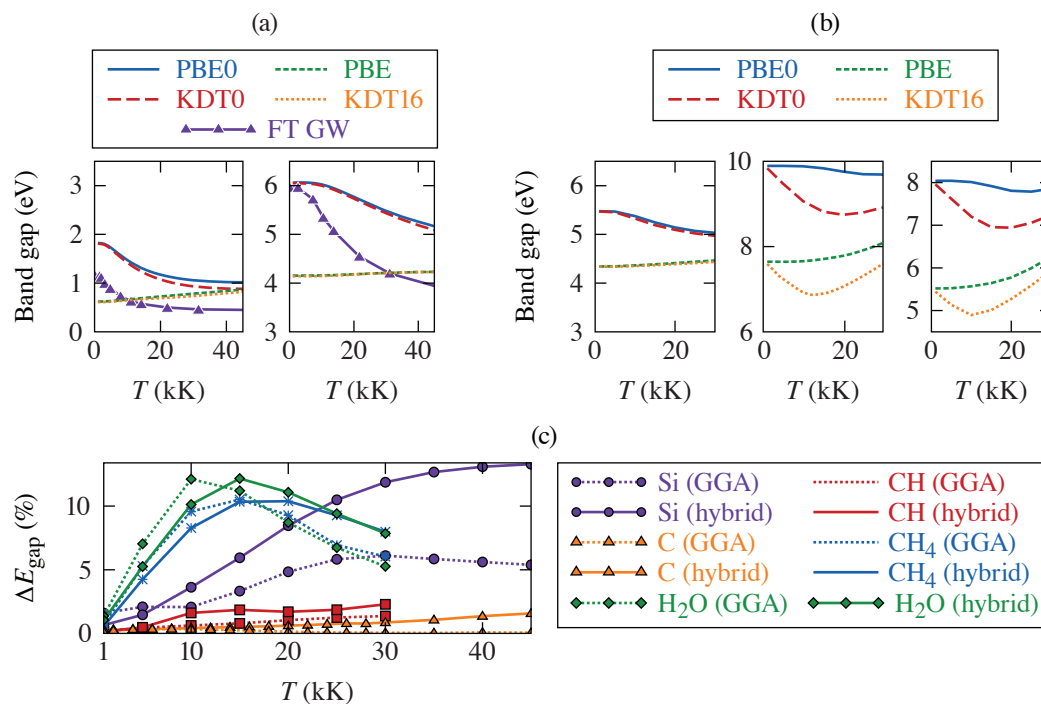
$$F_{XC}^{\text{hyb}}[n, T] = F_{XC}^{\text{DFA}}[n, T] + a(F_X^{\text{HF}}[n, T] - F_X^{\text{DFA}}[n, T]),$$

where  $F_{X[C]}^{\text{DFA}}[n, T]$  is the KDT16  $X[C]$  free-energy density functional,  $F_X^{\text{HF}}[n, T]$  is HF EXX free energy, and  $a = 1/4$  is a parameter that is rationalized in Ref. 4 and gives a zero- $T$  limit consistent with the PBE0 model. To compare performance between KDT0 and PBE0, we perform static calculations of the band gap as a function of electronic temperature  $E_{\text{gap}}(T)$  when the positions of ions are fixed at near-ambient conditions. This corresponds to a two-temperature model, cold ions  $T_i \approx 0$  K, and  $T$  is temperature of electrons  $T_e = T$ . The systems of choice are Si, C, CH<sub>4</sub>, polystyrene (CH), and H<sub>2</sub>O. The choice of Si and C was motivated by the need to compare the KDT0 functional to the highly accurate finite- $T$   $GW$  (Ref. 5) (FT  $GW$ ) calculations, which is a high-precision, first-principles, many-body perturbation theory approach but is prohibitively expensive for AIMD. CH, CH<sub>4</sub>, and H<sub>2</sub>O calculations were performed so that our choice of model systems spans a wide range of densities and magnitudes for the zero- $T$  gaps and also due to their relevance to high-energy-density physics (HEDP) and planetary science.

Figure 1 shows  $E_{\text{gap}}(T)$  results for Si and diamond, which are two of the systems addressed in Ref. 5. Let us first compare the GSA functionals PBE and PBE0 in the case of Si. At low  $T$ , they both give an approximately equally wrong value for the

$E_{\text{gap}}(T)$ , with PBE underestimating it and PBE0 overestimating it. At higher  $T$ , PBE0 predicts the same qualitative behavior as FT  $GW$ , monotonically decreasing  $E_{\text{gap}}(T)$ , while PBE predicts a monotonically increasing  $E_{\text{gap}}(T)$ , which is in direct contrast with FT  $GW$  predictions. The correct qualitative trend for  $E_{\text{gap}}(T)$  predicted by PBE0 is a direct result of including  $T$  effects in XC through the  $T$ -dependent HF  $X$  and serves as an indication of the importance of thermal effects in XC. The same improvement in the qualitative behavior of  $E_{\text{gap}}(T)$  provided by PBE0 is seen in diamond [Fig. 1(a) right]. Next, we turn our attention to results obtained with the thermal functionals KDT16 and KDT0. Most importantly, in both systems thermal XC effects lower the  $E_{\text{gap}}(T)$  curve toward the more-accurate FT  $GW$  results, thereby improving qualitative behavior for all temperatures considered. We stress, however, two important observations: (1) the thermal corrections are strongly system dependent, with the relative difference in the gaps predicted by PBE0 and KDT0 reaching a maximum of 12.7% in Si and only 1.5% in diamond at  $T = 45$  kK [see Fig. 1(c)]; (2)  $\Delta E_{\text{gap}}(T)$  for hybrid-level functionals is larger than that for GGA's, which is a result of the different treatment of thermal effects in the  $X$  interaction between the hybrid and GGA levels of approximation. Motivated by these observations, we apply KDT0 and KDT16 to other systems of drastically different properties, such as density  $\rho$  and  $E_{\text{gap}}$  at near-ambient conditions. Results for  $E_{\text{gap}}(T)$  in CH, CH<sub>4</sub>, and H<sub>2</sub>O for  $T$  up to 30 kK are shown in Fig. 1(b). In CH,  $\rho = 1.06$  g/cm<sup>3</sup>, relative differences in  $E_{\text{gap}}(T)$  predicted by PBE0 and KDT0 [see Fig. 1(b)] are small (<2.5%) and comparable to those in diamond. For CH<sub>4</sub>,  $\rho = 0.43$  g/cm<sup>3</sup>, and for H<sub>2</sub>O,  $\rho = 0.96$  g/cm<sup>3</sup>;  $\Delta E_{\text{gap}}(T)$  reaches values comparable to those in Si at 45 kK, although the peaks occur at much lower  $T$ .

In conclusion, we have presented a thermal hybrid XC functional based on the KDT16 GGA XC free-energy density as density functional approximation for  $X$  and  $C$  free-energy terms and thermal HF  $X$  free energy, which leads to a finite- $T$  extension of the PBE0 model, named here KDT0. Results for  $E_{\text{gap}}(T)$  in various systems of interest to HEDP show that KDT16 could provide significant improvement to calculations of electronic properties for  $T$  within the WDM regime. We also see significant thermal



TC15407JR

Figure 1

(a) Band gaps of Si (left) and diamond (right) as a function of electronic temperature calculated with ground-state PBE and PBE0 and thermal KDT16 and KDT0 functionals. The green curve (FT  $GW$ ) was extracted from Ref. 5. (b) Band gaps as a function of electronic temperature calculated with thermal (KDT0 and KDT16) and ground-state (PBE0 and PBE) functionals. (c) Relative difference between  $E_{\text{gap}}(T)$  predicted by GSA and thermal XC. Dotted lines correspond to GGA-level, and solid lines correspond to hybrid-level thermal corrections. Colors correspond to different systems, the absolute values of the gaps for which are shown in (a) and (b).

XC effects on the entire band structure of studied systems, meaning that the accuracy of optic properties calculated via the Kubo–Greenwood formalism depends on accounting for those effects via thermal hybrid XC functionals. Also, we show that the importance of XC thermal effects depends strongly on the type of system and  $T$  range and that taking XC thermal effects into account at the hybrid level of approximation can lead to larger corrections compared to those at the GGA level, which further warrants the need for the development of advanced thermal *free-energy* density functionals.

This material is based upon work supported by the U.S. Department of Energy National Nuclear Security Administration under Award Number DE-NA0003856 and U.S. National Science Foundation PHY Grant No. 1802964. This research used resources of the National Energy Research Scientific Computing Center, a DOE Office of the Science User Facility supported by the Office of Science of the U.S. Department of Energy under Contract No. DE-AC02-05CH11231.

1. V. V. Karasiev *et al.*, Phys. Rev. Lett. **112**, 076403 (2014).
2. V. V. Karasiev, J. W. Dufty, and S. B. Trickey, Phys. Rev. Lett. **120**, 076401 (2018).
3. V. V. Karasiev *et al.*, Phys. Rev. B **99**, 214110 (2019).
4. J. P. Perdew, M. Ernzerhof, and K. Burke, J. Chem. Phys. **105**, 9982 (1996).
5. S. V. Faleev *et al.*, Phys. Rev. B **74**, 033101 (2006).

# Soft X-Ray Spectrum Unfold of K-Edge-Filtered X-Ray Diode Arrays Using Cubic Splines

D. H. Barnak,<sup>1</sup> J. R. Davies,<sup>1</sup> J. P. Knauer,<sup>1</sup> and P. M. Kozlowski<sup>2</sup>

<sup>1</sup>Laboratory for Laser Energetics, University of Rochester

<sup>2</sup>Los Alamos National Laboratory

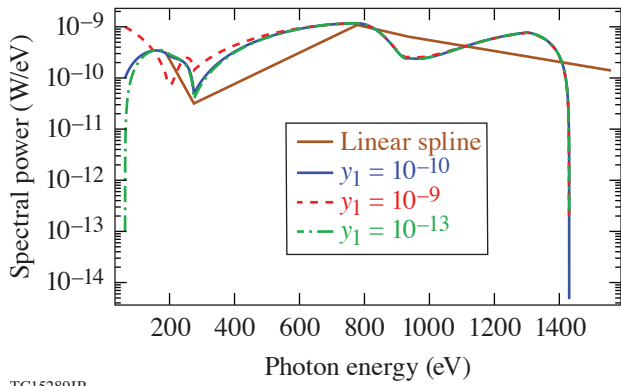
Spectrally integrated x-ray diagnostics<sup>1–3</sup> such as the ones fielded at the Omega Laser Facility and the National Ignition Facility make it possible to estimate radiation temperatures and spectral power without the need for crystal spectrometers. An array of x-ray diodes with different K-edge filters samples finite areas of the spectrum in question to determine the radiated power in that band. X-ray mirrors are also used as filters for high-energy photons for K-edge filters at lower-photon-energy bands. The filter components, x-ray diode, cable chain, attenuators, and digitizing oscilloscope form what is commonly referred to as a channel of the array. A typical array of diodes is capable of spanning the soft spectral range from 60 to 3000 eV.

Many methods<sup>4</sup> have been employed in the past to recover the x-ray spectrum from the channel signal traces, some of which require assumptions or measurements for the spectral shape<sup>5,6</sup> or considerations about the geometry<sup>7</sup> of the source. These methods are accurate but can suffer from complications such as insufficient signal-to-noise ratios or lack of signal due to overattenuation, or if the method is used outside of its intended purpose. Several methods have been previously published utilizing B splines<sup>8</sup> for spectral deconvolution,<sup>9,10</sup> along with proposed improvements on such methods utilizing intervals weighted with the relative intensity.<sup>11</sup> Cubic-spline interpolation was also used to obtain unfolded x-ray flux using *a priori* knowledge and several iterations to refine the interpolation.<sup>12</sup> Cubic-spline interpolation provides an alternative analytical way of solving for the temporally and spectrally resolved x-ray flux with no free parameters, assumptions about the geometry, or material of the emitting plasma.

The cubic spline is well known, and several derivations and codes are available as resources.<sup>13–15</sup> Much of the derivation follows the same notation found in Ref. 13 and a brief look at the derivation can be found in Ref. 12. The x-ray flux is interpolated across the entire spectral range with a series of piecewise cubic functions. The boundary of each cubic function lies between the K edges of each channel's response function. The voltages of each diode is then related to the interpolated x-ray flux by

$$V_i = \int_0^\infty (\mathbf{M}_y + 3\mathbf{M}_D \chi_1^{-1} \chi_2) \mathbf{y} R_i(E) \Omega_i dE, \quad (1)$$

where  $(\mathbf{M}_y + 3\mathbf{M}_D \chi_1^{-1} \chi_2)$  represents the framework of the cubic function which depends on photon energy,  $E$ ;  $\mathbf{y}$  is the vector of unknown values of the cubic function at the knot points, which are the independent variables for which to solve, and  $R_i(E)\Omega_i$  are the response functions and solid angle of the detector of the  $i$ th channel. The piecewise function is represented as a matrix to illustrate the linear system of equations that need to be solved in order to complete the reconstruction of the x-ray flux. The unknown values of the spline,  $\mathbf{y}$ , do not depend on photon energy and therefore do not contribute to the integral. Each row of the matrix is integrated over photon energy, and the matrix is then inverted to find the values of  $\mathbf{y}$ . Each row of the matrix refers to a channel of the x-ray diode array, and each column represents an interval of the spline. For  $n$  channels, there are  $n + 1$  unknowns for which to solve; therefore, either the initial value  $y_1$  or the final value  $y_{n+1}$  must be arbitrarily specified for the system to be solvable. For the specific implementation shown in this summary,  $y_1$  is calculated by solving for the flat channel contributions similar to previous methods and then using linear interpolation to find the value of  $y_1$ . Ultimately, the cubic spline solution is insensitive to the value chosen for  $y_1$  as shown in Fig. 1.



TC15289JR

Figure 1

The initial estimate of the first knot point value of the spline is the only part of the spline that is arbitrary. However, a linear spline calculation that can be solved with no free parameters can provide a good estimate of the initial value of the spline and thereby eliminate this free parameter. In the case where  $y_1 = 10^{-9}$ , even a slight overestimation of the spectral power can have a drastic impact and can even break the spline by giving non-physical results. The case inspired by the linear spline solution,  $y_1 = 10^{-10}$ , is equivalent to a gross underestimation of the initial value,  $y_1 = 10^{-13}$ .

Two sources of possible error propagate from measurement uncertainty: (1) measurement and calibration of the response functions<sup>16</sup> of each channel in the array; and (2) uncertainty and variation in the signal voltages digitized on the oscilloscope. Since the cubic spline is solved exactly from these quantities, an analytical expression for the uncertainty of the spline can be obtained. Each element of the matrix  $\int_0^\infty (\mathbf{M}_y + 3\mathbf{M}_D \mathcal{X}_1^{-1} \mathcal{X}_2) R_i(E) \Omega_i dE$  has an associated error from the response functions. Matrix inversion operations compound these error covariances enough to make even small covariances matter in the calculation. Finding an analytical solution in simple cases like a  $2 \times 2$  matrix is easy, but it still differs from the results calculated via Monte Carlo when errors cause the matrix to be close to singular.<sup>17</sup> Therefore, error propagation for matrix inversion must be done via Monte Carlo.

After the Monte Carlo error propagation, all of the error analysis can be done analytically. The error for all  $y_i$  values can be calculated from the matrix inverse  $\mathbf{S}$ :

$$\sigma_{y_i} = \left\{ \sum_j (S_{i,j} V_j)^2 \left[ \left( \frac{\sigma_{S_{i,j}}}{S_{i,j}} \right)^2 + \left( \frac{\sigma_{V_j}}{V_j} \right)^2 \right] \right\}^{1/2}, \quad (2)$$

where  $S_{i,j}$  is an element of the matrix inverse,  $\sigma_{S_{i,j}}$  is the associated error of that matrix element calculated via Monte Carlo, and  $\sigma_{V_j}$  is the random error associated with the measured voltage  $V_j$  of the  $j$ th channel. From here the rest of the cubic spline error can be calculated analytically.

A simple blackbody model and a detailed atomic model demonstrate how accurately cubic-spline interpolation recovers the temporally and spectrally resolved x-ray flux. A sample radiation temperature curve was used to generate synthetic diode voltage traces by convolving the blackbody spectrum with the channel response functions. These synthetic voltage traces were then used as input to the cubic-spline interpolation, and the solutions are then compared to the inputs as in Fig. 2. The cubic spline is able to solve for the blackbody spectrum and the radiation temperature accurately.

A detailed atomic model of a CNOFNe plasma was also used as an input to the cubic-spline interpolation to test the capability of the method to resolve an x-ray flux that is dominated by line emission (see Fig. 3). The input x-ray spectrum is compared visually to the output of the cubic-spline interpolation, and the spectral power in three different sections of the spectrum is compared numerically. The worst part of the spectrum overestimates the spectral power by a factor of 2, whereas the other two parts of the spectrum recover the spectral power exactly. Overall, the systematic error in the spectral power from the entire unfold is 20% from the cubic spline's inability to resolve the line structure, which corresponds to a 5% error in the radiation temperature. The systematic error is much smaller than the error that stems from the combination of the random error in the voltage trace and the error in measuring the response function in this case, so the conclusion is that the cubic-spline method can adequately recover line-dominated spectra.

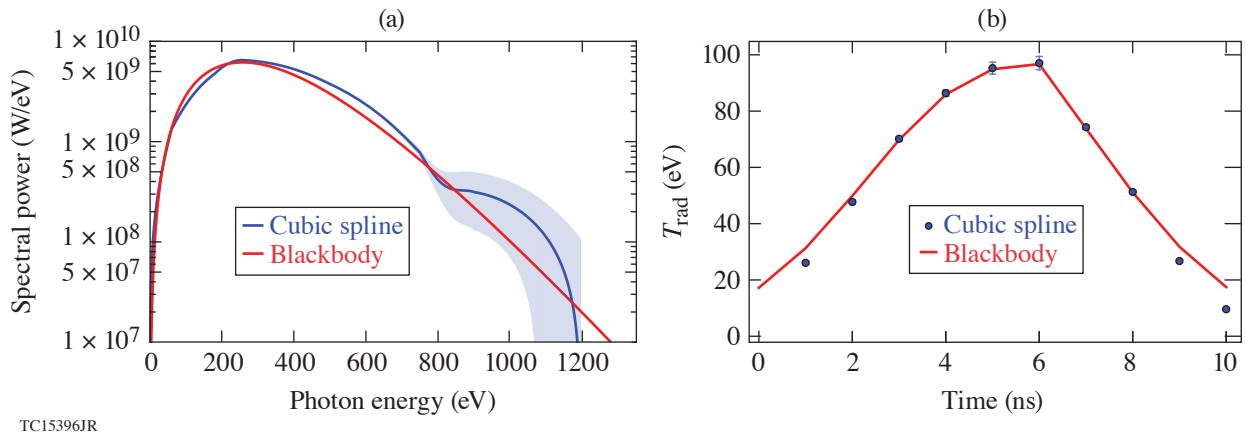


Figure 2

(a) The cubic spline is able to accurately reconstruct the blackbody spectrum at peak radiation flux. The shaded region around the spline solution represents a typical error associated with calibrated response functions. (b) The input radiation temperature curve used to generate the blackbody spectra and synthetic voltage traces plotted with the radiation temperature solution of the cubic spline at every nanosecond.

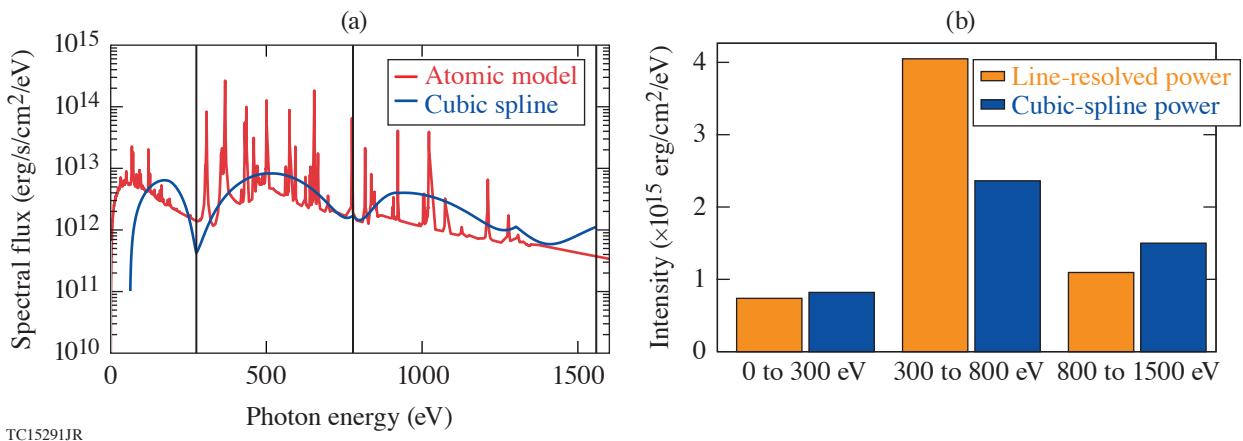


Figure 3

An atomic model of a CNOFNe plasma is convolved with the channel response functions. The resulting numbers are then used as signal inputs to the cubic-spline unfold algorithm. (a) The recovered cubic-spline spectrum is compared graphically to the atomic model. (b) The spectrum is divided into three line groups, and the integrated intensity of each line group is compared between the atomic model and the cubic spline. The cubic spline is able to conserve spectral power to within a factor of 2 or better in cases where the emission is extremely line dominated.

This material is based upon work supported by the Department of Energy National Nuclear Security Administration under Award Number DE-NA0003856, the University of Rochester, and the New York State Energy Research and Development Authority.

1. J. L. Bourgade *et al.*, *Rev. Sci. Instrum.* **72**, 1173 (2001).
2. E. L. Dewald *et al.*, *Rev. Sci. Instrum.* **75**, 3759 (2004).

3. C. Sorce *et al.*, Rev. Sci. Instrum. **77**, 10E518 (2006).
4. A. Seifter and G. A. Kyrala, Rev. Sci. Instrum. **79**, 10F323 (2008).
5. R. E. Marrs *et al.*, Rev. Sci. Instrum. **86**, 103511 (2015).
6. M. J. May *et al.*, Rev. Sci. Instrum. **87**, 11E330 (2016).
7. M. J. May *et al.*, Rev. Sci. Instrum. **83**, 10E117 (2012).
8. R. Goldman, *Pyramid Algorithms: A Dynamic Programming Approach to Curves and Surfaces for Geometric Modeling*, 1st ed. (Elsevier, Paris, 2003), pp. 347–443.
9. J. Li *et al.*, Rev. Sci. Instrum. **80**, 063106 (2009).
10. D. L. Fehl *et al.*, Rev. Sci. Instrum. **71**, 3072 (2000).
11. S. Tianming, Y. Jiamin, and Y. Rongqing, Rev. Sci. Instrum. **83**, 113102 (2012).
12. J. P. Knauer and N. C. Gindele, Rev. Sci. Instrum. **75**, 3714 (2004).
13. R. H. Bartels, J. C. Beatty, and B. A. Barsky, *An Introduction to Splines for Use in Computer Graphics and Geometric Modeling*, 1st ed. (Morgan Kaufmann Publishers, San Mateo, CA, 1987), pp. 9–17.
14. R. L. Burden and J. D. Faires, *Numerical Analysis*, 6th ed. (Brooks/Cole, Pacific Grove, CA, 1998), pp. 120–121.
15. W. H. Press *et al.*, *Numerical Recipes in FORTRAN: The Art of Scientific Computing*, 2nd ed. (Cambridge University Press, Cambridge, England, 1992), pp. 107–110.
16. K. M. Campbell *et al.*, Rev. Sci. Instrum. **75**, 3768 (2004).
17. M. Lefebvre *et al.*, Nucl. Instrum. Methods Phys. Res. A **451**, 520 (2000).

# Optical Characterization of the OMEGA Beam Profile at High Energy Using the Full-Beam-In-Tank Diagnostic

K. A. Bauer, M. Heimbueger, J. Kwiatkowski, S. Sampat, L. J. Waxer, E. C. Cost, J. H. Kelly, V. Kobilansky, S. F. B. Morse, D. Nelson, D. Weiner, G. Weselak, and J. Zou

Laboratory for Laser Energetics, University of Rochester

The OMEGA Laser System performs direct-drive inertial confinement fusion implosion experiments by using 60 ultraviolet (UV) beams focused onto a target in the center of a spherical target chamber.<sup>1</sup> Target-physics simulations suggest that the total on-target intensity (power per unit area) nonuniformity, with all 60 beams overlapped, must be less than 1% rms for optimum performance. The laser diagnostics used to assess on-target uniformity are located upstream of the target chamber and comprise a spatially integrated energy diagnostic (the harmonic energy diagnostic) and a temporal pulse-shape diagnostic (a P510 UV streak camera), both of which provide measurements of all 60 beams on each OMEGA shot. Experiments that independently estimate the on-target uniformity using measurements of x-ray production on metal targets suggest, however, that the balance is worse than the laser diagnostics indicate.<sup>2</sup> There is a limited capability for measuring the fluence distributions in the far field on OMEGA—the UV equivalent target plane (UV-ETP) diagnostic.<sup>3</sup> The ETP measurement does not include the full-energy effects of the final optics in the system, and beam-to-beam variations in target-plane fluence distributions cannot be effectively investigated using this setup. A new diagnostic, known as the full-beam-in-tank (FBIT) diagnostic<sup>4–6</sup> has therefore been developed to more accurately characterize the beam-to-beam variation in target-plane fluence.

The FBIT diagnostic is capable of measuring the on-shot, on-target focal spot of multiple beams inside the OMEGA target chamber. A direct measurement of a full-energy OMEGA beam ( $\sim 500$  J/beam) at target chamber center (TCC) presents a significant challenge. To overcome this, a small sample ( $\sim 0.9$  mJ) of the full-energy beam (Fig. 1) is collected by the FBIT diagnostic in the target chamber. To obtain the attenuated beam for characterization, the vacuum window and debris shield are altered. The standard vacuum window is replaced by one with a 7.5-arcmin wedge. This uncoated optic allows the light to undergo multiple Fresnel reflections, each emerging at a slightly different angle. The fourth-order reflection (with  $\sim 0.0003\%$  of the incident beam energy) is the one that enters the FBIT diagnostic. The debris shield, placed after the vacuum window, serves as a compensating wedge to address the aberrations introduced by the propagation of a focusing beam through the wedged vacuum window. Two

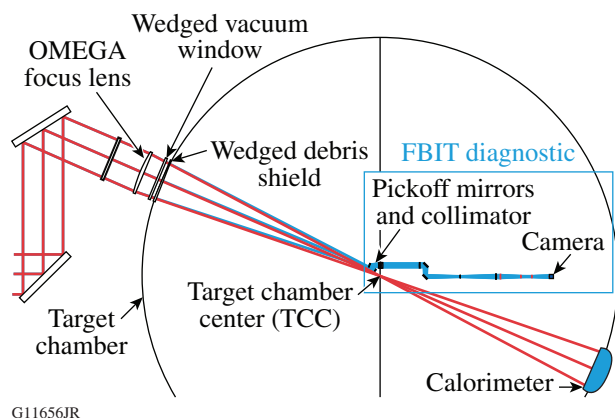


Figure 1

A schematic of the FBIT diagnostic. The main OMEGA beam is shown in red; the light blue rays indicate the fourth-order reflection from the wedged vacuum window that enters the FBIT diagnostic.

small mirrors at the front end of the FBIT diagnostic, aligned close to TCC, are designed to receive the Fresnel reflection of the main OMEGA beam for imaging onto a scientific-grade charge-coupled-device (CCD) camera, which is housed in a bubble since the target chamber is at vacuum. The remainder of the main beam propagates through TCC and is terminated at a calorimeter mounted in the opposing port, which measures the on-target energy. In addition to providing a direct measurement of a beam's fluence in the target chamber, the front end of the FBIT system rotates to characterize multiple beamlines within a single shot day.<sup>4</sup>

Initial experiments using the fourth-order reflection from the vacuum window had significant background light that made detailed characterization of a smoothed OMEGA focal spot difficult. Through modeling and laboratory measurements, it became clear that the source of the background light is scatter from the main beam. An upgrade was proposed for the FBIT diagnostic, referred to as FBIT 2.0, to address the background light issues. The primary design change was to utilize the second-order reflection from the wedged vacuum window, instead of the fourth-order reflection. Use of the second-order reflection increases the signal-to-background ratio since the increase in signal is much greater than the increase in background light as a result of collecting a solid angle that is in closer proximity to the main beam.

To maintain consistent intensities within FBIT for the upgrade, the first two mirrors in the diagnostic are replaced by uncoated NG-9 filter glass. There is a Fresnel reflection off of the first surface of the filter glass, and the remaining energy is absorbed by the filter. The attenuated second-order reflection from the wedged vacuum window then travels down the same path as the original FBIT diagnostic to the CCD.

Initial measurements taken with the FBIT 2.0 diagnostic indicate that the dynamic range of the smoothed far-field focal spots has been improved from the original design. Figure 2 shows an azimuthal average fit of one of the smoothed focal-spot images from the FBIT 2.0 diagnostic. The red vertical line indicates the  $R_{1/e}$  point on the azimuthal average fit curve, which is  $364\ \mu\text{m}$  for this beam. The fitting is much improved compared to the original FBIT diagnostic.<sup>6</sup> The fit, as expected, trends toward zero at the tail, whereas the data do not, even though a threshold is applied to the data at 0.5%. Some residual background light present in the images is currently being investigated.

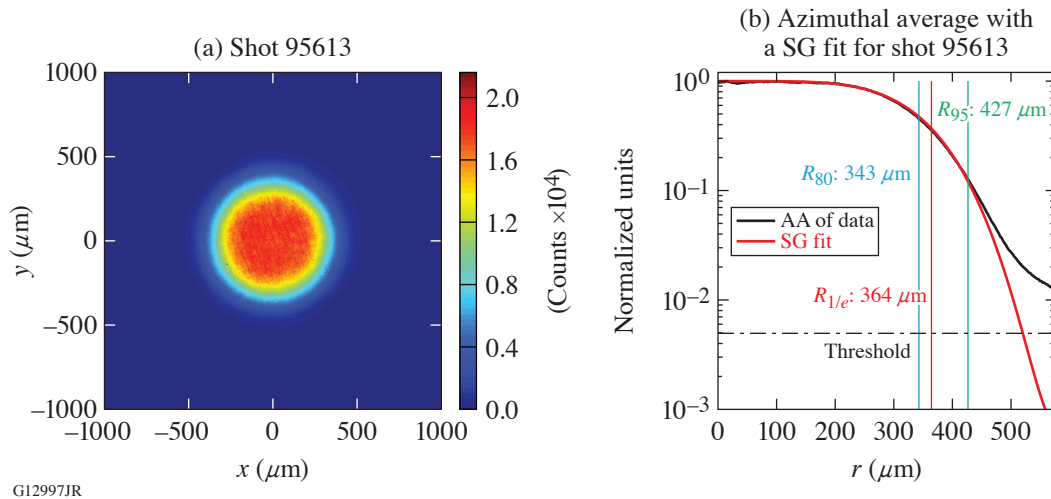


Figure 2

(a) A smoothed focal spot image taken with the FBIT 2.0 diagnostic; (b) The black curve is the azimuthal average (AA) of the smoothed focal spot data shown in (a), and the red curve is the super-Gaussian (SG) fit to the azimuthal average of the data. A threshold is applied to the image at 0.5% of maximum. The  $R_{80}$  of the AA of the data is shown by a blue vertical line; the  $R_{95}$  of the AA of the data is shown by a green vertical line.

The FBIT diagnostic was developed to measure the on-target beam-to-beam focal-spot variation on the OMEGA Laser System. With the FBIT 2.0 upgrade, signal-to-background levels were significantly increased, allowing for precise characterization of

on-shot OMEGA focal spots. Further aberration correction and background light mitigation will further improve measurement fidelity as the FBIT is used to characterize up to 31 of OMEGA's 60 beams.

This material is based upon work supported by the Department of Energy National Nuclear Security Administration under Award Number DE-NA0003856, the University of Rochester, and the New York State Energy Research and Development Authority.

1. T. R. Boehly *et al.*, *Opt. Commun.* **133**, 495 (1997).
2. F. J. Marshall *et al.*, *Phys. Plasmas* **11**, 251 (2004).
3. S. P. Regan *et al.*, *J. Opt. Soc. Am. B* **17**, 1483 (2000).
4. L. J. Waxer *et al.*, *Proc. SPIE* **10898**, 108980F (2019).
5. K. A. Bauer *et al.*, *Proc. SPIE* **10898**, 108980G (2019).
6. K. A. Bauer *et al.*, "Optical Characterization of the On-Target OMEGA Focal Spot at High Energy Using the Full-Beam In-Tank Diagnostic," to be published in *Applied Optics*.

# Deposition of a Discontinuous Coated Surface to Form a Phase-Stepped Reflected Wavefront

J. B. Oliver, J. Spaulding, B. Charles, D. Coates, and D. H. Froula

Laboratory for Laser Energetics, University of Rochester

Advancements in spatiotemporal control of laser intensity have enabled new approaches to manipulating laser–plasma interactions and applying these developments in unique ways.<sup>1–4</sup> The “flying focus” scheme uses a chromatic focusing system together with chirped laser pulses to create a laser focus that can propagate at a speed that is decoupled from the group velocity of the laser light.<sup>5,6</sup> The spectral separation of this system extends, however, the minimum pulse duration and limits its usefulness for applications that require ultrashort laser pulses.<sup>7</sup> Recently, a novel achromatic concept was proposed to overcome this limitation.<sup>8</sup> This “achromatic flying focus” uses a radial echelon together with an axiparabola<sup>9</sup> to generate a small focal spot that can propagate over extended distances while maintaining an ultrashort temporal duration.

The goal of this effort is to develop an optical component with a wavelength-scale stepped-surface relief; the axiparabola and the reflective echelon together can produce a focal spot that propagates at the speed of light over a distance of 1 cm without temporally stretching a 15-fs laser pulse. Deposition of a silicon-dioxide thin film via electron-beam evaporation through a mask<sup>10</sup> was used to form the surface structure shown in Fig. 1(a), followed by dc magnetron sputtering of a reflective aluminum layer. The deposited surface structure was formed on a 100-mm-diam × 9-mm-thick glass substrate rotating behind the mask shown in Fig. 1(b) to create an azimuthally uniform thickness.

The mask design uses 23 concentric annular rings with progressively larger angular widths as a function of the radial position on the optic to achieve the profile shown in Fig. 1(a). This required a deposited thickness of 24.2  $\mu\text{m}$  since the maximum open

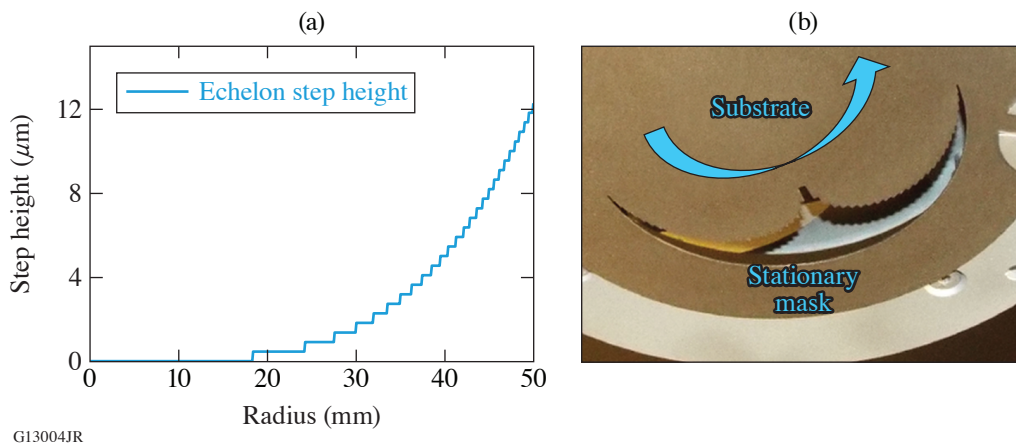


Figure 1

(a) Desired deposition profile to achieve discrete steps of 0.53  $\mu\text{m}$  over the surface of the component. Such a physical step on the surface yields a phase step of  $\pi$  or  $2\pi$  in reflection. (b) The mask placed in front of the rotating optic has a series of discrete, discontinuous steps to yield the specified profile, with thinner layers near the optic center and thicker layers near the periphery.

space in the mask design is 50%. Each successive mask opening was designed to provide a stepped surface with  $0.526\ \mu\text{m}$  less height, using a mask-design scheme similar to the design for continuous surface profiles.<sup>11</sup> The optic center, which is coincident with the substrate-rotation axis, has no deposited thickness. The aluminum layer deposited over the structured surface was limited to approximately 20-nm thickness to minimize degradation of the surface profile while achieving >90% reflectance.

The substrate surface relief was measured using stitching white-light interferometry as shown in Fig. 2. The flatness and transitions of the steps indicate that an accurate duplication of the desired surface profile was achieved with minimal blurring between steps in a manner that should quickly diverge light incident on the transitions out of the optical system. The transitions are of the order of  $150\ \mu\text{m}$  in width, representing 5% to 10% of the total substrate area.

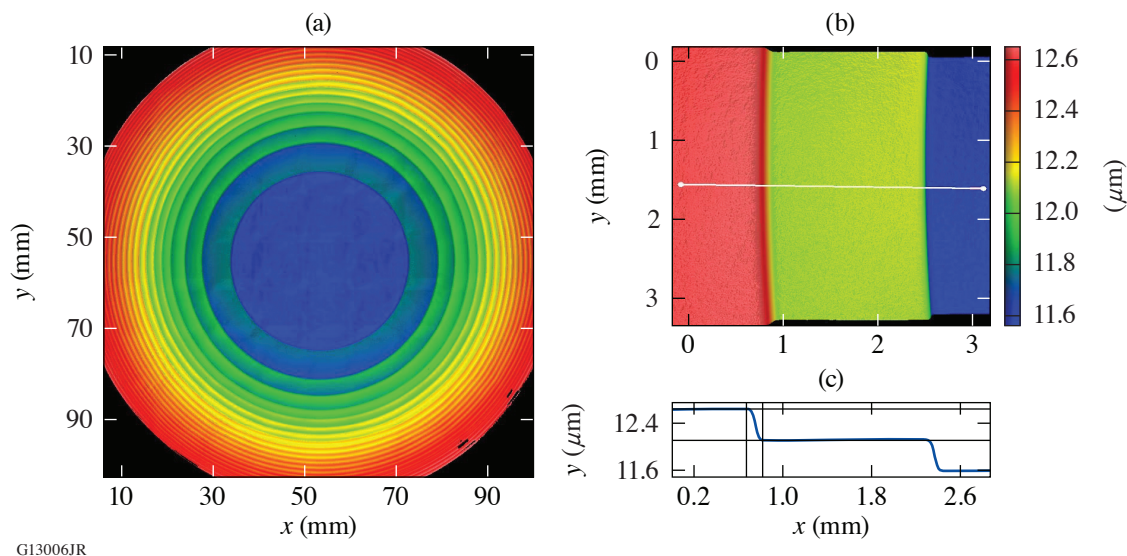


Figure 2

The surface profile of the echelon component as measured with a Zygo NexView white-light interferometer. (a) The overall optic surface is based on a series of stitched measurements. The (b) higher-magnification image and (c) corresponding lineout provide greater detail on the step shape and linear extent of the transition between steps. The step heights differ from nominal by <3%, while the transitions between steps are of the order of 0.15 mm.

This work showed it is possible to vapor deposit a reflective echelon component for use in an achromatic flying focus. The resulting film structure provides accurate steps to yield the desired discontinuous reflected-wavefront phase profile. Future work may focus on reducing the lateral extent of the transitions by increasing the source-to-substrate distance and further shrinking the mask/substrate separation. Alternative deposition materials may potentially be explored, as well as collimation of the vapor source.<sup>12</sup>

This material is based upon work supported by the U.S. Department of Energy Office of Fusion Energy Sciences under Contract No. DE-SC0016253 and the U.S. Department of Energy National Nuclear Security Administration under Award Number DE-NA0003856, the University of Rochester, and the New York State Energy Research and Development Authority.

1. D. Turnbull *et al.*, Phys. Rev. Lett. **120**, 024801 (2018).
2. D. Turnbull *et al.*, Phys. Rev. Lett. **120**, 225001 (2018).
3. P. Franke *et al.*, Opt. Express **27**, 31,978 (2019).

4. D. H. Froula *et al.*, Nat. Photonics **12**, 262 (2018).
5. A. Howard *et al.*, Phys. Rev. Lett. **123**, 124801 (2019).
6. A. Sainte-Marie, O. Gobert, and F. Quéré, Optica **4**, 1298 (2017).
7. D. H. Froula *et al.*, Phys. Plasmas **26**, 032109 (2019).
8. J. P. Palastro *et al.*, Phys. Rev. Lett. **124**, 134802 (2020).
9. S. Smartsev *et al.*, Opt. Lett. **44**, 3414 (2019).
10. J. B. Oliver and D. Talbot, Appl. Opt. **45**, 3097 (2006).
11. J. B. Oliver, J. Spaulding, and B. Charles, Appl. Opt. **59**, A54 (2020).
12. J. B. Oliver *et al.*, presented at SVC Techcon 2014, Chicago, IL, 3–8 May 2014.

# Damage Mechanisms in Multilayer Dielectric Gratings at Different Pulse Durations

B. N. Hoffman,<sup>1</sup> A. A. Kozlov,<sup>1</sup> N. Liu,<sup>2</sup> H. Huang,<sup>1</sup> J. B. Oliver,<sup>1</sup> A. L. Rigatti,<sup>1</sup> T. J. Kessler,<sup>1</sup> A. Shestopalov,<sup>1,2</sup> and S. G. Demos<sup>1</sup>

<sup>1</sup>Laboratory for Laser Energetics, University of Rochester

<sup>2</sup>Department of Chemical Engineering, University of Rochester

Multilayer dielectric (MLD) diffraction gratings typically consist of an etched layer of SiO<sub>2</sub> that resides on top of a multilayer dielectric high-reflector stack composed of alternating layers of SiO<sub>2</sub> and HfO<sub>2</sub> to form a periodic structure of lines and trenches with a predetermined line density and line width. This design allows for higher laser-induced-damage thresholds (LIDT's) compared to their metal grating predecessors.<sup>1,2</sup> The LIDT of optical components incorporated in high-power, short-pulse laser systems is of critical importance since it affects the maximum laser output and/or the operational cost. The current generation of MLD gratings has a LIDT that is limited by defects embedded in the coating, which can be separated into two general categories. The first category is atomic defects and nanoscale defect structures introduced during coating that cause localized absorption. The second category is the defects introduced during the photolithographic and etching stages of grating manufacturing.<sup>3,4</sup> Determining the laser-damage-initiation mechanisms in MLD gratings has been elusive mainly because it is associated with the removal of grating pillars, thereby erasing any characteristic signatures. To study the laser-damage signatures, we created 5-mm grating-like structures that simulate the magnitude of the electric-field-intensity (EFI) enhancement observed in MLD gratings. The macroscopic lateral scale of the pillars in the structure allow for spatially targeted damage testing, while the inherent mechanical stability of the structure enables the preservation of damage signatures for postmortem study. The results from the grating-like structures can subsequently elucidate the damage morphology and associated laser-damage mechanisms in actual MLD gratings.

The grating-like structures were etched into a SiO<sub>2</sub> coating using processes similar to those used for MLD gratings. The grating-like structures are 700 nm in height, which is of the order of the MLD grating pillar height [see Fig. 1(a)]. The pillar height of the grating-like structures results in a 3× internal EFI enhancement factor, which is similar to that observed near the

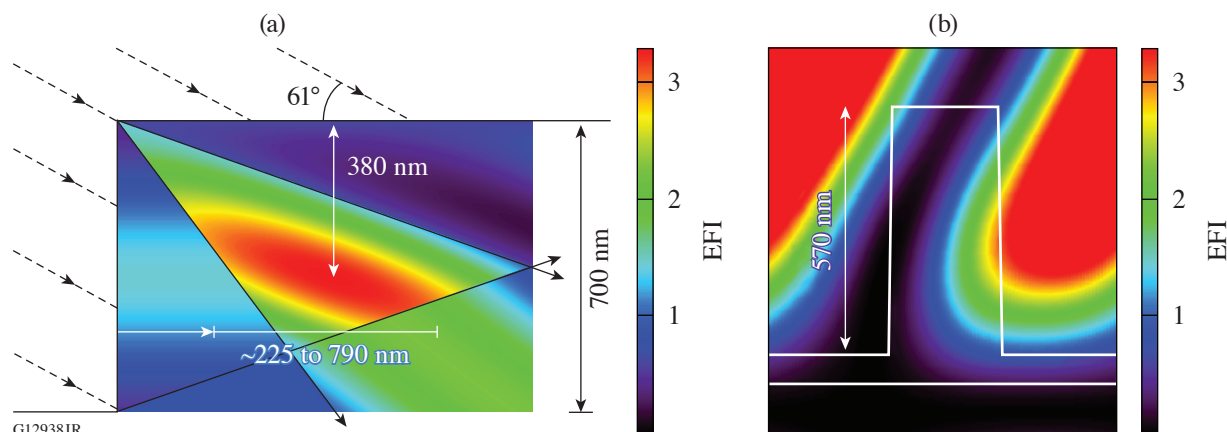


Figure 1

The EFI enhancement (a) near the millimeter-pitch pillar wall region and (b) for the MLD grating design used in this work. The laser excitation is incident on the samples at a 61° angle from the left side.

right side of the MLD grating pillars [see Fig. 1(b)]. The grating-like structure and the MLD grating samples were damage tested in vacuum at 0.6 ps and 10 ps.

Previous work by Kozlov *et al.*<sup>5</sup> demonstrated that there are three types of laser-induced–damage mechanisms in multilayer dielectric coatings. Type-I damage is driven by the EFI enhancements within the most vulnerable material layer and involves removal of the overlying material over the area of peak laser intensity. Type-I damage occurs with pulse widths shorter than 2.5 ps. The damage mechanisms of the pillar wall of the grating-like structure for 0.6-ps laser pulses showed distinct signatures of the type-I damage mechanisms, such as a removal of coating sections within the area of the peak laser-beam intensity [see Fig. 2(a)] and a damage crater depth similar to the depth of the EFI enhancement [see Fig. 2(b)]. The morphology of the crater involves melted nanoscale projections from the explosive boiling process and the sharp crater edges, which are reminiscent of type-I craters observed with MLD high-reflector coatings [see Fig. 2(a), right inset image].

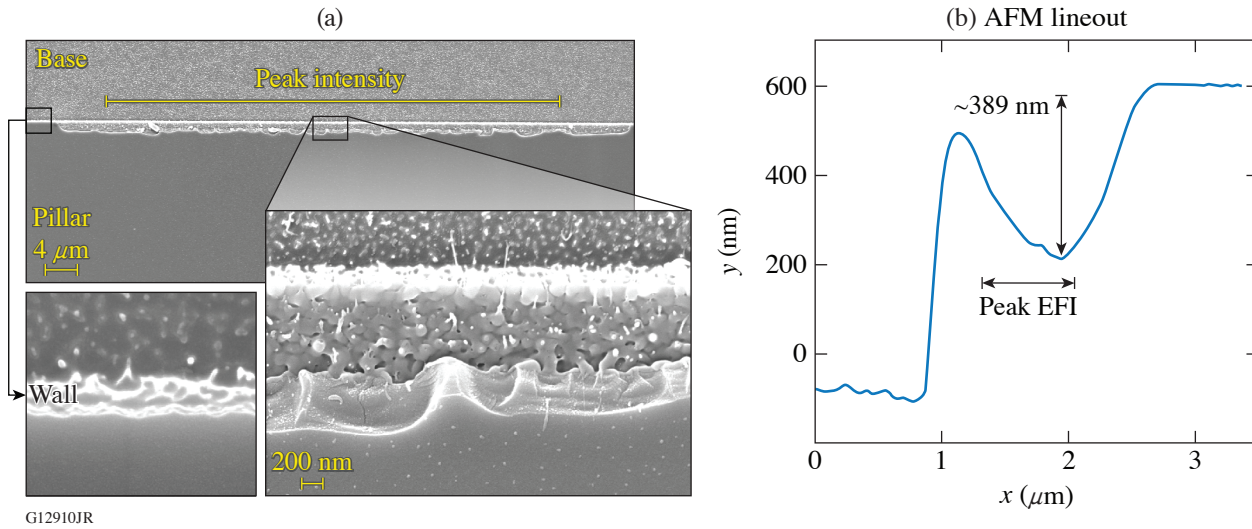
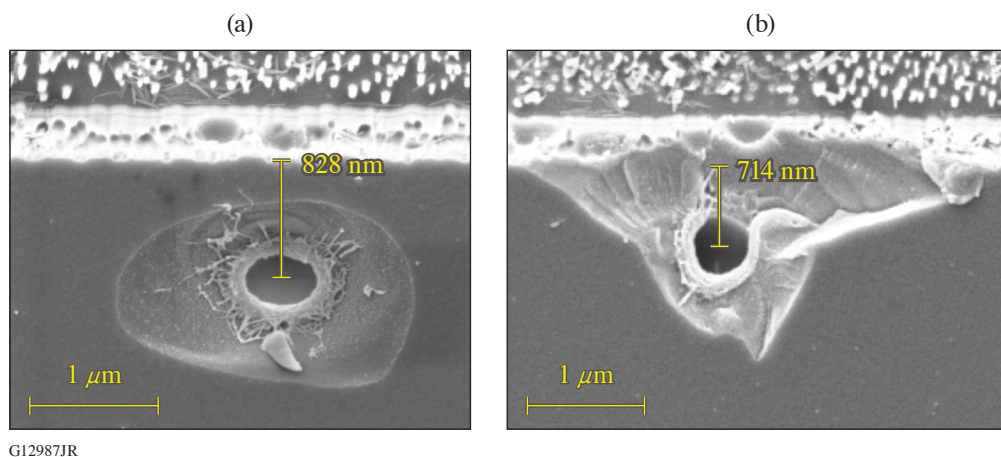


Figure 2

(a) Scanning electron microscope (SEM) images of the wall region in millimeter-pitch grating-like structures containing a damage site generated with a 0.6-ps pulse. The left inset shows in higher magnification the undamaged part of the wall region, and the right inset shows a section of the damage region. The laser beam impinges from the top at 61°. (b) A cross-sectional lineout of the damage region obtained with atomic force microscopy imaging reveals the depth and exact position of the damage site.

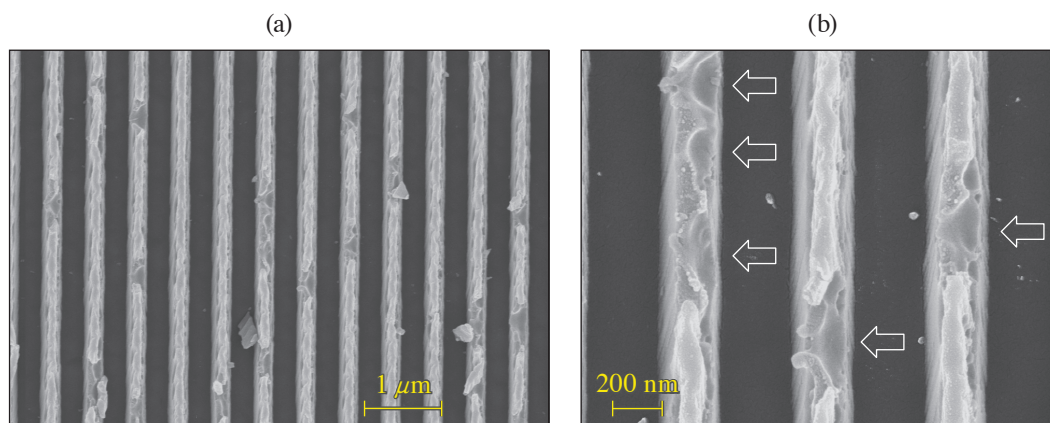
The type-II and type-III damage initiation processes in MLD coatings occur with laser pulses longer than 2.5 ps and are defect driven, resulting in the formation of micrometer-size craters. It was previously discussed that the temperature and pressure relaxation pathways following plasma formation at the defect location govern the morphology of the type-II damage.<sup>5</sup> The damage mechanisms observed on the grating-like pillar wall irradiated by 10-ps laser pulses (see characteristic examples in Fig. 3) are consistent with defect-driven damage near the EFI maximum enhancement, which is analogous to the type-II damage observed with MLD coatings.

Although damage in MLD gratings includes pillar removal, thereby concealing the primary signatures of the damage mechanisms, the use of grating-like structures helped us to recognize fingerprint signatures on which to draw correlations. MLD grating damage sites generated with 0.6-ps pulses exhibit modification on the pillar wall, primarily on the right side where the EFI enhancement is known to be maximum [see Figs. 1(b) and 4] along with melted nanoparticles between damage pillars [see Fig. 4(b)]. These observations are consistent with the mechanisms and signatures observed with the grating-like structures seen in Fig. 2. Specifically, damage causes removal of sections of the pillar at the locations of maximum EFI while melted nanoparticles are observed between the pillars, which correspond to the nanoscale projections observed at the bottom of the type-I crater for the grating-like structures (separation of nanodroplets from the superheated material).



G12987JR

Figure 3  
SEM images of damage sites generated under 10-ps pulses in the wall region in a millimeter-pitch grating.



G12985JR

Figure 4  
SEM images of areas of an MLD grating where (a) laser-induced damage was initiated under a single 0.6-ps laser pulse and (b) the image of the central region at a higher magnification shows nanoparticle distribution. The laser excitation impinges on the samples at a 61° angle of incidence from the left side.

The primary morphology of laser damage in MLD gratings under 10-ps irradiation also involves removal of pillars, but there are characteristic differences from the pillar damage observed with 0.6-ps pulses. First, pillar removal often involves the entire pillar, not just the side. Second, the 10-ps damage consists of isolated sites that often span multiple pillars [see Fig. 5(a)]. Lastly, a larger number of melted nanoparticles [see Fig. 5(b)] as well as fragments [see Fig. 5(a)] are present within or near damage sites. This type of damage is suggestive of the type-II damage as also observed with the grating-like structures. However, the boundary conditions due to the small size of the grating pillars must be considered. Specifically, since the depth of the damage-initiating defect can vary, damage can initiate at different locations within the pillars. This gives rise to a variability on the damage morphology, including the height of the removed sections of the pillars as well as the number of pillars involved for each individual damage site. However, the distribution of generated nanoparticles within the trenches provides a fingerprint of the exact locations of the pillar involving the explosive boiling (damage).

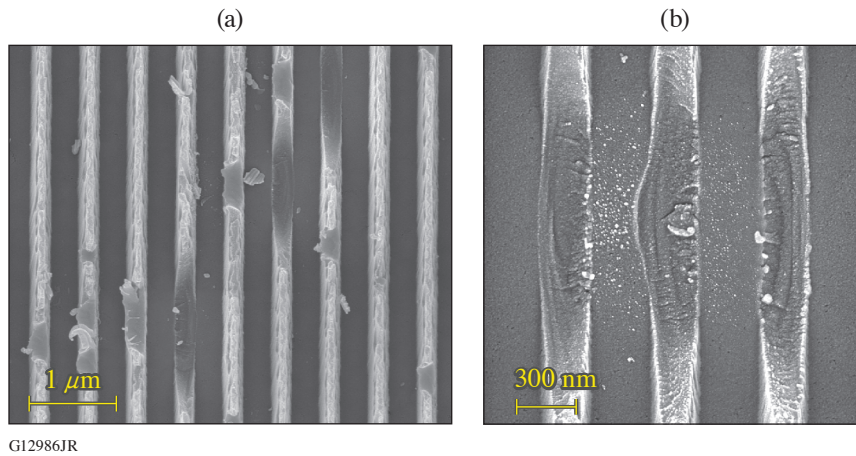


Figure 5

SEM images of areas of an MLD grating where (a) laser-induced damage was initiated under a single 0.6-ps laser pulse and (b) the image of the central region at a higher magnification shows nanoparticle distribution. The laser irradiation impinges on the samples at a 61° angle of incidence from the left side.

In summary, by studying the damage mechanisms and signatures of grating-like structures, we were able to better understand the damage mechanisms for MLD gratings. This information will help advance our ability to design and fabricate the next-generation gratings that will exhibit a significantly higher damage threshold.

This material is based upon work supported by the Department of Energy National Nuclear Security Administration under Award Number DE-NA0003856, the University of Rochester, and the New York State Energy Research and Development Authority.

1. B. W. Shore *et al.*, *J. Opt. Soc. Am. A* **14**, 1124 (1997).
2. J. A. Britten *et al.*, *Proc. SPIE* **2714**, 511 (1996).
3. H. P. Howard *et al.*, *Appl. Opt.* **52**, 1682 (2013).
4. W.-J. Kong *et al.*, *Chin. Phys. Lett.* **22**, 1757 (2005).
5. A. A. Kozlov *et al.*, *Sci. Rep.* **9**, 607 (2019).

# Laser-Induced–Damage Behavior of Novel Glassy Liquid Crystal Materials at 1 ns and Multiple Wavelengths

J. U. Wallace, K. L. Marshall, T. Z. Kosc, D. J. Batesky, B. N. Hoffman, S. Papernov, L. Garrett, J. Shojaie, and S. G. Demos

Laboratory for Laser Energetics, University of Rochester

Low-molar-mass (LMM) liquid crystal (LC) fluids have demonstrated a proven track record of high-peak-power performance on the OMEGA Nd:glass laser at LLE since 1985. Over 320 large-aperture LC circular polarizers (LCP's) and wave plates were installed during OMEGA's upgrade to 351-nm, 60-beam, 40-TW capability in 1994. Notably, a few LCP devices installed at that time are still functional after 25 years of service. Such LC devices offer large-aperture scalability (200 mm), high optical quality and contrast with low insertion loss, precision retardance (tune by blending), broad angular tolerance, and excellent laser-damage resistance ( $>30 \text{ J/cm}^2$ , 1 ns, 1053 nm). In certain operational environments (e.g., such as in vacuum or where accidental fluid leakage can have additional adverse consequences), liquid materials are generally deemed unsuitable. Glassy liquid crystals (GLC's) offer the unique optical properties of LMM LC fluids, but the anisotropic ordering of LC phases is frozen into the solid state through vitrification. As a result, GLC's offer significant additional advantages such as resistance to mechanical disturbance, elimination of fluid leakage risk, and alleviation or reduction in the need for thick substrates.

To explore the potential benefits of GLC materials, this work is focused on designing high laser-induced–damage threshold (LIDT) GLC materials for large-aperture polarization control/beam-smoothing optics that could replace current LMM LC devices on OMEGA as well as offering the potential for use in other inertial confinement fusion (ICF)-class laser systems in future upgrades. A recent detailed study of LIDT in LC's performed at LLE indicated that reducing the absorption edge of LC materials significantly improves their damage thresholds for high-peak-power laser applications.<sup>1</sup> Based on that effort, a series of increasingly saturated (less aromatic) GLC's was synthesized with the goal of preserving their desirable optical and morphological properties while improving their endurance under irradiation by UV laser pulses and continuous-wave (cw), broadband UV light. This study explores an array of materials, ranging from an unsaturated aromatic GLC to highly saturated GLC's. The highly saturated GLC's show promising damage resistance under both irradiation conditions and offer considerable potential for application in both high-peak-power laser systems and aerospace optical systems.

The GLC material synthesis effort was complemented by examining the LIDT of these materials using both classical 1-on-1 and *N*-on-1 tests (yielding the 1-on-1 LIDT and the *N*-on-1 LIDT) as well as a 100-shot protocol. The latter was introduced in order to probe the long-term behavior and stability of the materials under continued exposure. Each site was shot at a given fluence at 0.1 Hz (once every 10 s) for either 100 shots *or* until damage was observed. The highest fluence at which a site survives 100 shots was defined as the 100-shot LIDT for the sample. A series of GLC's with progressively lower unsaturation and lower UV absorbance were synthesized, in which a stable cholesteric GLC phase can be generated by quench-cooling on substrates coated with rubbed alignment layers. Table I provides details on the materials synthesized and their characteristic properties. Purification by semi-automated flash chromatography was employed to remove trace contaminants and significantly improve LIDT's as compared to conventional purification methods (e.g., crystallization or precipitation from organic solvents).

The robustness of these materials to high-peak-power laser pulses as a function of unsaturation is evidenced by the LIDT data shown in Table I for three GLC materials tested at the three Nd:glass laser harmonic wavelengths and 1- to 1.5-ns pulse lengths. Test samples of 22- $\mu\text{m}$ -thick GLC films, which are within the useful thickness regime for LC polarization control devices, were melt processed on fused-silica substrates and quenched into unaligned, nearly isotropic states to examine the intrinsic damage

Table I: Properties and LIDT values of GLC materials synthesized with differing levels of saturation in their respective molecular structures under exposure to laser pulses at 351, 523, and 1053 nm having durations of about 1 ns, 1.2 ns, and 1.5 ns, respectively.

GLC material	Aromatic rings	Absorption cutoff	1-on-1 (J/cm <sup>2</sup> ) 351/532/1053 nm	N-on-1 (J/cm <sup>2</sup> ) 351/532/1053 nm	100 shot (J/cm <sup>2</sup> ) 351/532/1053 nm
GLC-Bz3ChN2R	10	340 nm	0.61/-/-	0.43/-/-	-/-/-
GLC-Bz3CholC5	1	310 nm	4.9/16.1/38.9	-/-/-	1.0/4.3/22.3
GLC-CCH3CholC3	0	250 nm	5.9/-/16.4	3.9/-/9.7	0.88/-/5.2

resistance of each material independent of alignment conditions. For this set of materials (and particularly at 351 nm), the LIDT increases as they become more saturated and have deeper UV absorption edges [Fig. 1(a)]. For example, at 351 nm the most-unsaturated material, GLC-Bz3ChN2R, has only a meager 1-on-1 LIDT of 0.61 J/cm<sup>2</sup>, which rises to 4.9 J/cm<sup>2</sup> for the more-saturated GLC-Bz3CholC5 and reaches 5.9 J/cm<sup>2</sup> for the highly saturated GLC-CCH3CholC3. These results follow the observed trend for LMM LC's, where LIDT values increase with increasing saturation and decreasing absorption edges.<sup>1</sup> As was seen in that study, reducing the  $\pi$ -electron delocalization and increasing the effective material band gaps appears to be quite beneficial in increasing the LIDT in GLC materials as well. While this principle holds true within experimental error at 351 nm, more-subtle details in the vibronic and electronic structures could potentially account for the different ordering seen in the 1053-nm LIDT values.

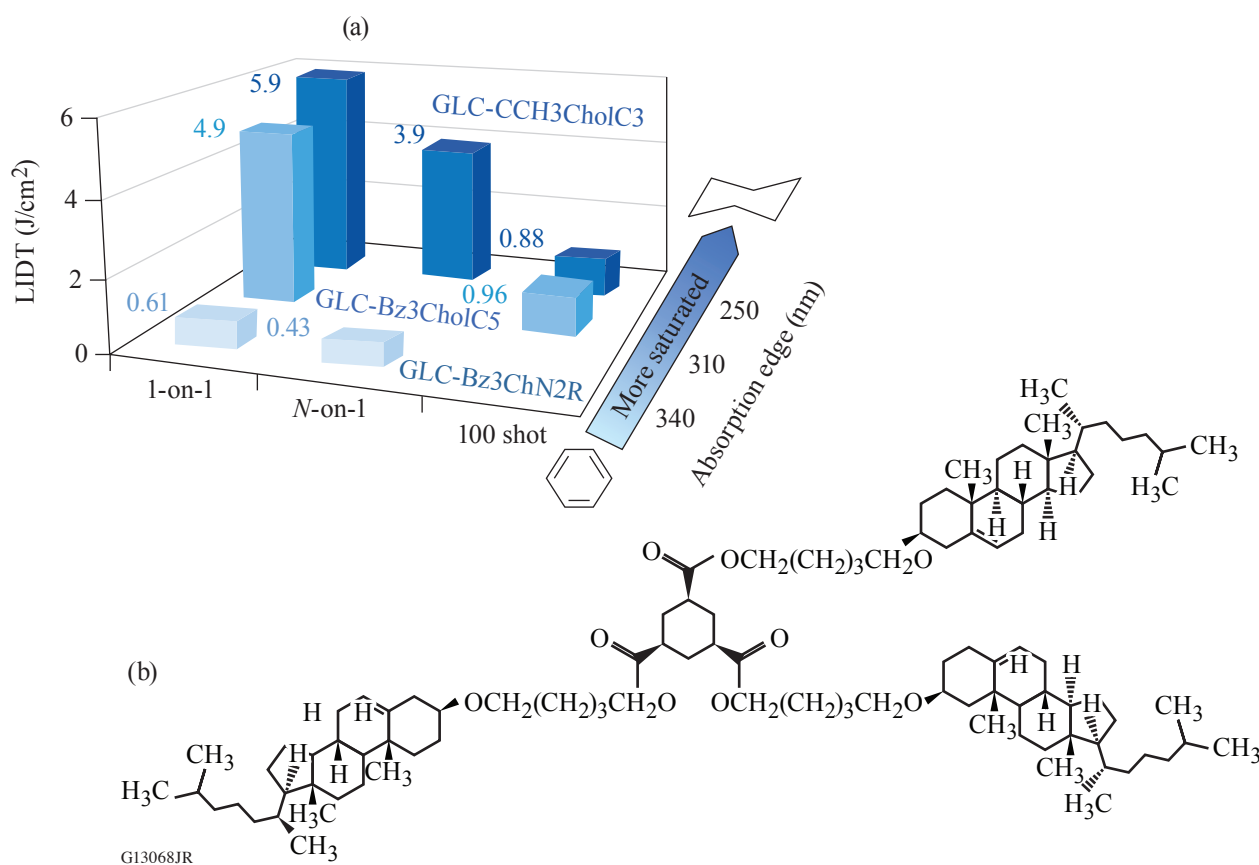


Figure 1

(a) LIDT values for 22- $\mu$ m-thick films of highly purified GLC materials sandwiched between two fused-silica substrates obtained with 351-nm, 1-ns pulses; (b) the molecular structure of GLC-Bz3CholC5.

Among this set of GLC materials, GLC-Bz3CholC5 shows the best overall performance for high-peak-power laser applications, particularly in the infrared (IR) spectral region, where its 100-shot LIDT was over 20 J/cm<sup>2</sup>. These results make GLC-Bz3CholC5 a promising candidate for use in polarization control or isolation elements for near-IR (NIR) lasers. A key behavior that remains of issue in all GLC materials synthesized to date is the degradation of the LIDT with continued exposure to laser pulses. This effect is observed for all damage-testing wavelengths, but it is more prominent for UV pulses. Specifically, the reduction of the 100-shot LIDT at 1053 nm in the best-performing GLC-Bz3CholC5 is approximately twofold compared to the 1-on-1 LIDT at the same wavelength, but it is about fivefold at 351 nm. To further understand the cumulative effects in the laser-damage behavior of these GLC's and explore them for use in cw UV environments, such as in aerospace applications as optical elements,<sup>2</sup> GLC films were subjected to broadband UV irradiation at 250 to 400 nm and their absorbance spectra were monitored as a function of exposure time. These exposure conditions increased the absorption coefficient in the UV region, which in turn contributes to lowering the LIDT values. Further understanding and development of mitigation strategies for this effect will be the subject of future work.

In conclusion, a series of increasingly saturated GLC's synthesized in multigram quantities and evaluated for their laser-induced-damage behavior at wavelengths relevant to OMEGA operations (1053 nm, 532 nm, and 351 nm) demonstrated promising performance. Reducing the  $\pi$ -electron delocalization in GLC molecules by employing saturated pendants, along with unconventional materials purification techniques, results in GLC's with improved LIDT's with 1-on-1 thresholds as high as 5.8 J/cm<sup>2</sup> at 351 nm, 16.1 J/cm<sup>2</sup> at 532 nm, and 38.9 J/cm<sup>2</sup> at 1053 nm. The results also demonstrate the potential for fabricating single-substrate GLC optical elements, especially for NIR laser applications where the 100-shot LIDT exceeds the current operational fluence of major ICF-class laser systems.

This material is based upon work supported by the Department of Energy National Nuclear Security Administration under Award Number DE-NA0003856, the University of Rochester, and the New York State Energy Research and Development Authority.

1. T. Z. Kosc *et al.*, *Sci. Rep.* **9**, 16435 (2019).
2. E. Otón *et al.*, *IEEE Photonics J.* **7**, 6900909 (2015).

# Morphologies and Underlying Mechanisms of Laser-Induced Damage by Model Contamination Particles on a High Reflector

K. R. P. Kafka, B. N. Hoffman, H. Huang, and S. G. Demos

Laboratory for Laser Energetics, University of Rochester

Due to the significant cost to replace optics that have sustained laser-induced damage in large-aperture laser systems, management strategies aim to maintain laser-damage performance over long time durations by (a) preventing the generation of new damage sites and (b) arresting the growth of existing damage sites. Contamination of optical elements during installation and from the operational environment has been recognized for nanosecond-class lasers as an important contributor toward these problems.<sup>1–6</sup> Specifically, contamination particles can become the source of damage initiation via a number of mechanisms, depending on the contamination material (such as metal or dielectric) and optical substrate properties (such as reflective or transmissive). Furthermore, the laser-induced–damage process with nanosecond pulses has been shown to eject particles from the affected optics that can transport onto adjacent optics and become the source of additional damage initiation.<sup>7</sup>

The potential for analogous processes occurring in short-pulse laser systems has received much less attention, although there have been reports of degradation of laser-induced–damage thresholds (LIDT’s). The LIDT-degradation of the LFEX (laser for fast ignition experiment) laser pulse compressor was attributed to organic contamination,<sup>8</sup> and the cause of degradation of OMEGA EP compression gratings is not yet resolved.<sup>9</sup> We recently demonstrated, using model contamination particles (including metal, glass, and plastic spherical particles) dispersed on the surface of a multilayer dielectric mirror, that exposure to 0.6-ps and 10-ps pulses at 1053 nm can introduce damage and spread secondary contamination at fluences that are significantly lower than that of the pristine surface.<sup>10</sup> Here we expand on that work, with a primary objective to investigate the laser–particle interactions that lead to these damage initiations and/or secondary contamination depositions. Several interaction mechanisms leading to material modification and damage are identified, including localized field intensification by multibeam interference and particle-induced microlensing, plasma-induced scalding, and secondary contamination via nanoparticle generation and particle melting. The secondary objective of this work is to investigate the impact of additional pulses irradiating these sites. A second pulse irradiating damaged sites caused damage growth at fluences significantly below the initiation threshold, and a second pulse irradiating secondarily contaminated sites could not significantly remove that contamination without initiating additional damage.

The reduction of LIDT in the presence of the particles was caused by intensification of the electric field locally, as shown in Fig. 1. For reflective particles (steel in this work), a multibeam interference pattern between the particle and mirror is generated, leading to sickle-shaped ripples of intensification on the laser-incident side of the microsphere. The peak value of intensity or fluence enhancement ( $4.3 \times$  the incident value) calculated by coherent ray-tracing simulation is consistent with the LIDT reduction factor measured in experiments (4.6 and 4.0 for 0.6-ps and 10-ps pulses, respectively). On the other hand, transparent particles act as a microlens, focusing the laser onto the optic surface and leading to an ablation crater of a few- $\mu\text{m}$  diameter. Due to the symmetry of the microspheres, a strong local fluence enhancement factor of approximately 200 was observed for glass microspheres. This damage can occur even without removal of the particle, as demonstrated by Fig. 1(e).

These intensification mechanisms were also responsible for energy deposition and ablation from the surface of the particle itself, leading to dispersal of secondary contamination onto the optic. The multibeam interference mechanism occurring for the steel particles produced fringes of similar amplitude on the particle as well and generated nanoparticles that could be deposited over a large area of the optic [Fig. 2(a)]. Although the peak intensification of the microlensing mechanism occurs outside the particle,

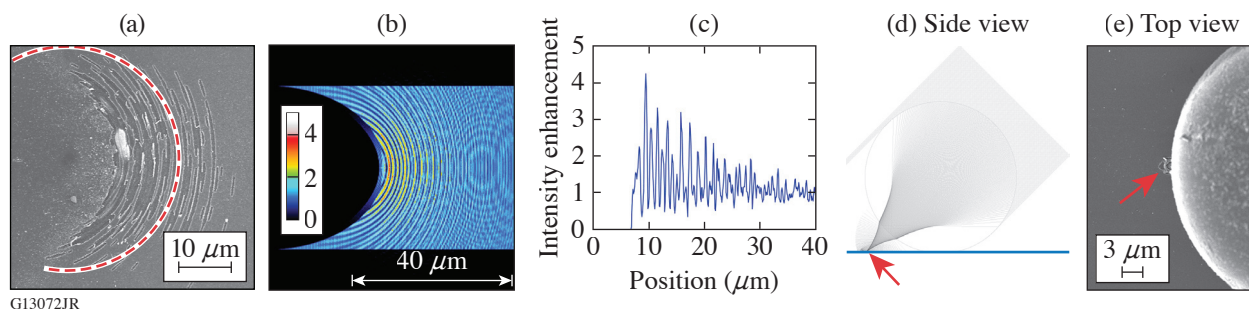


Figure 1

Mechanisms of laser intensification that lead to damage initiation. Optical interference from a steel microsphere: (a) damage morphology for 0.6 ps, 1.1 J/cm<sup>2</sup>, with initial particle location shown (dashed line), (b) corresponding calculated intensity pattern with (c) central horizontal lineout. Microlensing by a glass microsphere: (d) ray-tracing diagram and (e) damage morphology for 0.6 ps, 32 mJ/cm<sup>2</sup>, with damage indicated by an arrow. Laser is incident at 45° incidence from the right.

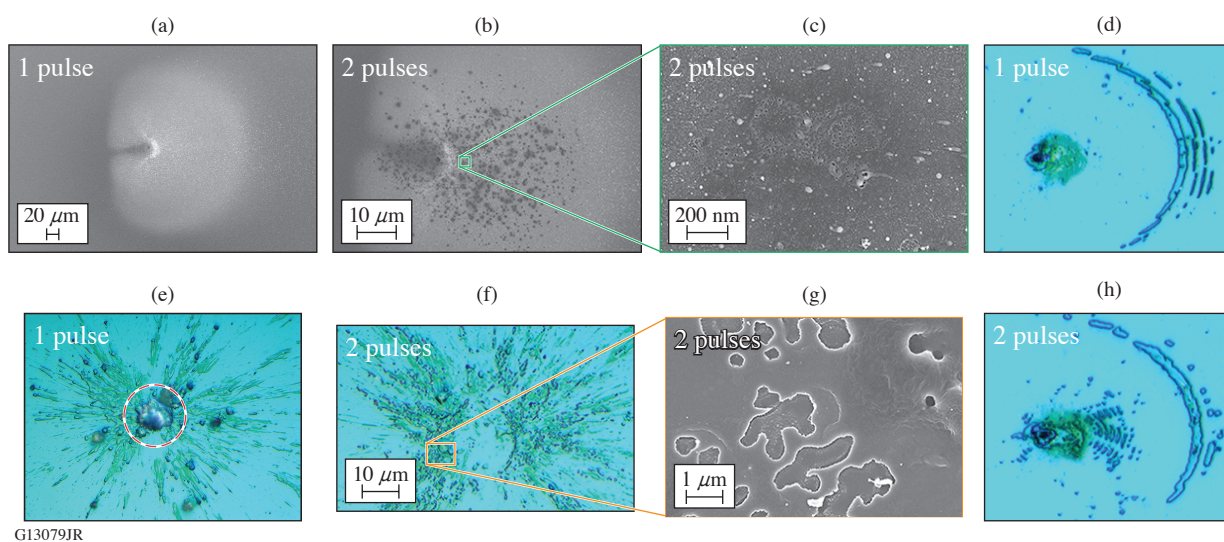


Figure 2

Morphological effects compared between one and two laser pulses incident on a microparticle. Parameters: [(a)–(c)] steel microsphere, 10 ps, 1.4 J/cm<sup>2</sup>; [(e)–(g)] polyethylene microsphere, 0.6 ps, 0.8 J/cm<sup>2</sup>; [(d),(h)] glass microsphere, 0.6 ps, 0.9 J/cm<sup>2</sup>. For comparison, pristine LIDT was 1.4 J/cm<sup>2</sup> and 6.7 J/cm<sup>2</sup> for 0.6-ps and 10-ps pulses, respectively.

the partial beam convergence inside the bulk of the particle leads to intensification of up to one order of magnitude. This causes absorption in the bulk, leading to localized ablation accompanied by secondary contamination by liquefied jets and fragments [shown for polyethylene in Fig. 2(e)].

An additional pulse irradiating these sites did not cause favorable results. For steel particles [Figs. 2(b) and 2(c)], the nanoparticle contamination was partially removed (“laser cleaning”), but that process created plasma scalds (permanently modifying the surface). For polyethylene particles [Figs. 2(f) and 2(g)], the contamination removal process generated ablation sites in the coating. For all particle types, the second pulse could also cause the growth of any existing damage, as shown in Figs. 2(d) and 2(h) with glass particle morphology as an example. In this case, the fluence was high enough with the first pulse to generate damage by both interference and microlensing mechanisms. The second laser pulse caused all craters to grow in area and additionally generated new ripples of damage.

This work demonstrates that the contamination microparticles can be a potent precursor for optical damage with short pulses, causing damage initiation far below the pristine LIDT, and thereby exposing optics to the potential for damage growth. It is therefore important to better understand the role of such mechanisms in the operation of laser systems such as OMEGA EP and to devise proper management or mitigation strategies.

This material is based upon work supported by the Department of Energy National Nuclear Security Administration under Award Number DE-NA0003856, the University of Rochester, and the New York State Energy Research and Development Authority.

- 1 C. J. Stolz *et al.*, Proc. SPIE **10691**, 106910W (2018).
2. M. J. Matthews *et al.*, J. Opt. Soc. Am. B **30**, 3233 (2013).
3. R. N. Raman *et al.*, Opt. Express **24**, 2634 (2016).
4. S. G. Demos *et al.*, Opt. Express **24**, 7792 (2016).
5. S. R. Qiu *et al.*, Appl. Opt. **54**, 8607 (2015).
6. S. G. Demos *et al.*, Opt. Express **27**, 23,515 (2019).
7. S. G. Demos and R. A. Negres, Opt. Eng. **56**, 011016 (2017).
8. T. Jitsuno *et al.*, Proc. SPIE **8786**, 87860B (2013).
9. A. A. Kozlov *et al.*, “Long-Term Monitoring the Damage Performance of Multilayer Dielectric Grating Samples Residing Inside the Compressor Chamber of the OMEGA EP Laser,” submitted to Optical Engineering, Special Section on Laser Damage V.
10. K. R. P. Kafka and S. G. Demos, Opt. Lett. **44**, 1844 (2019).

# Determination of the Raman Polarizability Tensor in the Optically Anisotropic Crystal Potassium Dihydrogen Phosphate and Its Deuterated Analog

T. Z. Kosci,<sup>1</sup> H. Huang,<sup>1</sup> T. J. Kessler,<sup>1</sup> R. A. Negres,<sup>2</sup> and S. G. Demos<sup>1</sup>

<sup>1</sup>Laboratory for Laser Energetics, University of Rochester

<sup>2</sup>Lawrence Livermore National Laboratory

Potassium dihydrogen phosphate (KDP) and its deuterated analog (DKDP) crystals are widely used nonlinear optical materials in laser applications. They exhibit excellent UV transmission, high damage thresholds and birefringence, and can be grown to large sizes. These properties make them uniquely suited for use in large-aperture inertial confinement fusion (ICF)-class laser systems such as the OMEGA and OMEGA EP lasers and the National Ignition Facility,<sup>1,2</sup> where they are currently used for frequency conversion,<sup>3</sup> polarization control, and beam smoothing.<sup>4</sup> In large-aperture plates, however, the relatively high Raman scattering cross-section of KDP/DKDP supports the generation and transfer of energy to parasitic beams arising from transverse stimulated Raman scattering (TSRS). This effect is of concern in ICF-class lasers due to the high incident laser intensities and long pulse durations that support the exponential increase of the TSRS signal as it traverses the aperture of the crystal plate<sup>5,6</sup> and ultimately leads, if not properly managed, to damage to the optic and the surrounding hardware during laser operation.<sup>7</sup> The TSRS Raman-gain coefficient can be calculated from the propagation length (optic size), the laser intensity and pulse duration, and a complete description of the spontaneous Raman scattering cross section (Raman polarizability tensor).<sup>8,9</sup> The latter is of critical importance to enable one to model TSRS for suitable crystal-cut configurations to help optimize designs. Theory mandates that the Raman tensor is diagonal,<sup>10</sup> but extensive previous efforts yielded results suggesting contributions by off-axis elements.<sup>11,12</sup> This issue has hindered an accurate modeling of TSRS.

In this work, we determine the form of the Raman tensor and identify artifacts that have interfered in previous studies. A unique experimental system developed at LLE employs spherical samples, which enable one to “directly” measure tensor elements through rotation of the sphere to the required scattering geometries.<sup>13</sup> Data were acquired by rotating the sphere through 360° in the azimuthal plane, which is defined as the laboratory  $x$ - $z$  plane and contains both the pump-beam propagation and the Raman signal observation directions (Fig. 1). The azimuthal angle  $\phi = 0^\circ$  is defined along the laboratory  $z$  axis. Laboratory coordinates are defined by lower-case italicized letters  $x$ ,  $y$ , and  $z$ , while upper-case letters  $X$ ,  $Y$ , and  $Z$  designate crystallographic axes. The experimental notation  $k_p [e_p e_s] k_s$ , designates the propagation direction of the pump  $k_p$ , and scattered light  $k_s$  as well as the unit electric polarization vectors of the pump  $e_p$  and scattered light  $e_s$ . For clarity, we define the notation for each trace, or set of measurements while the sample is rotated ( $\phi = 0^\circ$  to  $360^\circ$ ), based on the initial orientation of the sample for  $\phi = 0^\circ$  in reference to the crystal axes. Square brackets are omitted in the trace labels in order to differentiate the notation of a data set and specific Raman scattering configurations within that data set.

Three data sets acquired with the crystallographic  $Z$  axis, or the optic axis (OA), found in the azimuthal laboratory  $x$ - $z$  plane are shown in Fig. 1. The trace labeled ZYYX provides data for scattering in the Z[YY]X configuration at azimuthal angles  $\phi = 0^\circ$  and  $180^\circ$ , while scattering data for the X[YY]Z configuration are collected at  $\phi = 90^\circ$  or  $270^\circ$ . The polarization orientations of both the pump laser and the Raman scattering signal (and analyzer) for trace ZYYX are perpendicular to the azimuthal plane. A corresponding trace acquired when (a) the analyzer is rotated by  $90^\circ$  (in the azimuthal plane) is shown as ZYZX, and (b) the pump polarization rotated  $90^\circ$  is shown as ZXYX. The signal of the  $A_1$  mode of KDP,<sup>11</sup> centered at  $915 \text{ cm}^{-1}$ , is integrated between  $860$  and  $960 \text{ cm}^{-1}$ . Unexpected features such as double peaks and valleys are detected at the specific angles of importance for determining the matrix elements.

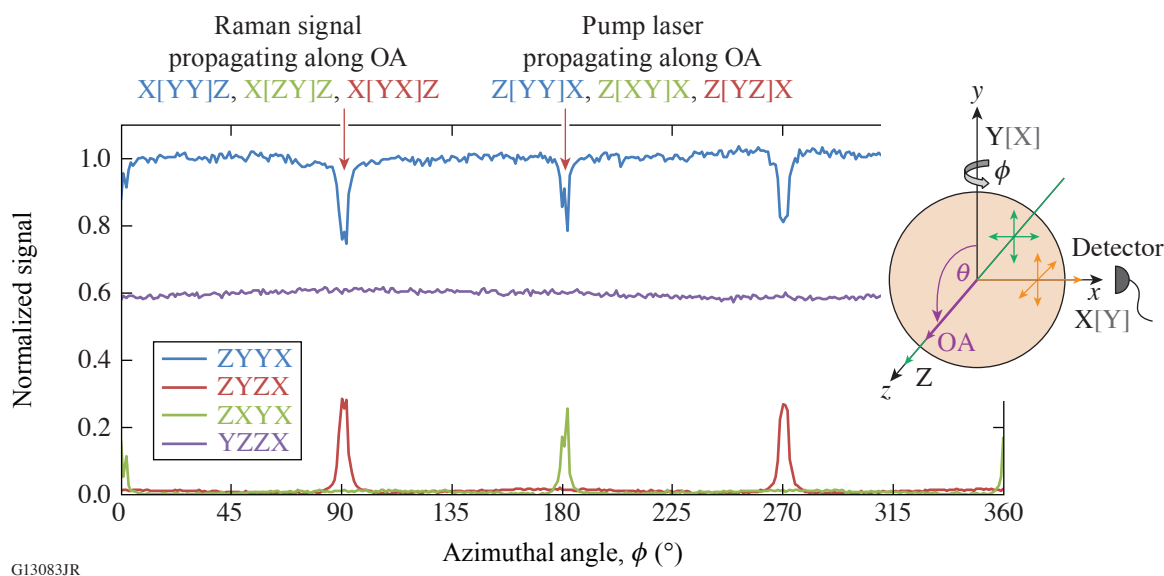


Figure 1

The experimental geometry for Raman scattering measurements is based on a spherical sample (inset). Three traces in which the pump laser and/or the scattering signal propagating along the optic axis experience depolarization are shown. Depolarization artifacts in the form of peaks and valleys arise at azimuthal angles that correspond to configurations at which tensor element values are determined. Data were acquired with an  $\sim 1.0^\circ$  collection half-angle.

These features were reproduced by a ray-trace model that does not consider off-axis tensor elements. The model does consider, however, that in the actual measurement, there is a finite solid angle for the focused laser beam and for the collected Raman scattering. The converging pump laser and the diverging Raman scattering undergo a change of polarization state as a function of propagation length inside the material and orientation of the OA leading to the depolarization of the propagating light. The effect is exacerbated when rays converge or diverge along the OA (because the differential phase between the ray components experiencing the ordinary and extraordinary indices of refraction is the greatest) and increases with the solid angle involved.

Polarization rotation is responsible for the peaks and valleys at critical scattering geometries shown in Fig. 1. The ZYYX trace (blue curve), acquired with the OA lying in the azimuthal plane, should be flat. The polarization, rotation effects observed at  $\phi = 0^\circ$  and  $180^\circ$  (Z|YY|X configuration) occur, however, because the vertical polarization of the pump light is altered (i.e., a horizontally polarized component is produced), reducing the amount of Raman signal generated by vertically polarized pump light. An analogous condition exists at  $\phi = 90^\circ$  and  $270^\circ$  (X|YY|Z configuration), where the Raman scatter signal propagates along the OA. The Raman scattering signal “lost” to polarization rotation effects appears in configurations for which there should be no Raman scattering from the  $A_1$  mode. Specifically, the slightly wider peaks observed in the ZYZX trace (red) at  $\phi = 90^\circ$  and  $270^\circ$  (X|YX|Z configuration) correspond to the polarization rotation of the X|YY|Z configuration exhibiting valleys in the Raman intensity at the same angles. Similarly, the corresponding “lost” signal of the Z|YY|X configuration appears as sharp narrow peaks in the ZXYX trace (green) at the same azimuthal angles (Z|XY|X configuration). Here the polarization rotation of the pump light generates a Z|YY|X component that gives rise to the observed signal where no signal should be found. Note, that data were collected at the smallest-possible collection angle to minimize polarization rotation artifacts.

A closer examination of the Raman scattering spectral profile in the  $860\text{- to }960\text{-cm}^{-1}$  integration region for all spectra within each data set led to the identification of additional Raman modes whose spectral profiles partially overlap into the wave number range considered for the determination of the intensity of the  $915\text{-cm}^{-1}$  mode. Spectra for the YZZX trace, which includes both Y|ZZ|X and X|ZZ|Y configurations, all show the same strong  $915\text{-cm}^{-1}$  peak (Fig. 2). Configurations corresponding to the ZYXY trace, Z|YX|Y and Y|ZX|Z, determine off-axis tensor elements and should not generate a scattering signal. Spectral analysis confirmed that the strong peaks at  $\phi = 0^\circ$  and  $180^\circ$  in the ZYYX trace are due to a  $915\text{-cm}^{-1}$  peak arising from depolarization effects. The spectrum for the X|ZY|Z configuration reveals that Raman scattering from additional low-intensity modes adjacent

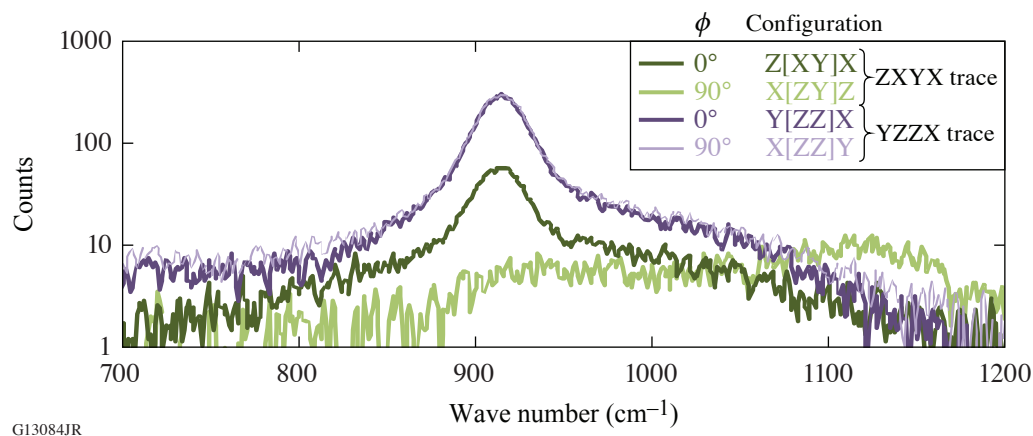


Figure 2

Selected spectra at 0° and 90° demonstrate the presence of Raman scattering from the dominant  $A_1$  mode of KDP (trace YZZX) and the depolarization and the overlap of neighboring modes (trace ZXYX). Data acquired with an  $\sim 0.5^\circ$  focusing half-angle and  $1.0^\circ$  collection half-angle.

to the  $915\text{-cm}^{-1}$  mode overlap with the integration region and give rise to erroneous signals that can be misinterpreted as arising from nondiagonal matrix elements.

The theoretical description of the Raman tensor  $R$  for the  $A_1$  mode is represented by a diagonal matrix.<sup>13</sup> In the following analysis, all other tensor elements are normalized to the value of  $A$ , which is assigned the maximum value of trace ZYXX (or ZXXY). The matrix element  $B$  is determined solely by averaging of the entire trace YZZX. The examination of spectra for all experimental configurations confirmed that the Raman tensor for the dominant  $A_1$  mode contains no off-axis terms. The same analysis was performed for both KDP and 70% DKDP samples tested in an experimental setup using a  $1.0^\circ$  collection half-angle. Future work will explore the dependence of the collection aperture on the tensor element values more carefully.

$$R(A_1) = \begin{pmatrix} A & 0 & 0 \\ 0 & A & 0 \\ 0 & 0 & B \end{pmatrix} \quad R_{\text{KDP}} = \begin{pmatrix} 1 & 0 & 0 \\ 0 & 1 & 0 \\ 0 & 0 & 0.79 \pm 0.01 \end{pmatrix} \quad R_{70\% \text{ DKDP}} = \begin{pmatrix} 1 & 0 & 0 \\ 0 & 1 & 0 \\ 0 & 0 & 0.76 \pm 0.02 \end{pmatrix}.$$

This material is based upon work supported by the Department of Energy National Nuclear Security Administration under Award Number DE-NA0003856, the University of Rochester, and the New York State Energy Research and Development Authority.

1. J. D. Lindl *et al.*, Phys. Plasmas **11**, 339 (2004).
2. N. Fleurot, C. Cavailler, and J. L. Bourgade, Fusion Eng. Des. **74**, 147 (2005).
3. W. Seka *et al.*, Opt. Commun. **34**, 469 (1980).
4. T. R. Boehly *et al.*, J. Appl. Phys. **85**, 3444 (1999).
5. C. E. Barker *et al.*, Proc. SPIE **2633**, 501 (1995).
6. S. N. Dixit *et al.*, J. Phys. IV France **133**, 717 (2005).
7. K. R. Manes *et al.*, Fusion Sci. Technol. **69**, 146 (2016).

8. Y. R. Shen and N. Bloembergen, *Phys. Rev.* **137**, A1787 (1965).
9. A. Z. Grasiuk and I. G. Zubarev, *Appl. Phys.* **17**, 211 (1978).
10. R. Loudon, *Adv. Phys.* **13**, 423 (1964).
11. W. L. Smith, M. A. Hennesian, and F. P. Milanovich, *Laser Program Annual Report 1983*, 6-61, Lawrence Livermore National Laboratory, Livermore, CA, Report UCRL-50021-83 (1984).
12. S. G. Demos *et al.*, *Opt. Express* **19**, 21050 (2011).
13. T. Z. Kosc *et al.*, *Rev. Sci. Instrum.* **91**, 015101 (2020).

# Long-Term Monitoring of the Damage Performance of Multilayer Dielectric Grating Samples Residing Inside the Compressor Chamber of the OMEGA EP Laser

A. A. Kozlov, S. G. Demos, D. Canning, B. N. Hoffman, B. E. Kruschwitz, A. L. Rigatti, and L. J. Waxer

Laboratory for Laser Energetics, University of Rochester

The laser-induced-damage threshold (LIDT) of the final transport optics is a critical factor limiting the output energy in ultrahigh-power lasers (e.g., OMEGA EP) based on chirped-pulse amplification. The multilayer dielectric (MLD) gratings in such laser systems are expensive, hard to manufacture/replace, and highly susceptible to laser-induced damage.<sup>1</sup> Two pulse compressors on OMEGA EP are stacked vertically in a single grating compression chamber (GCC) having internal dimensions of 4.57 m × 4.57 m × 21.34 m (15 ft × 15 ft × 70 ft) and operating under nominal vacuum of  $2 \times 10^{-6}$  Torr. The GCC is populated with over 100 optomechanical structures, control devices, and optical components and vented for quarterly maintenance. Although all materials and manufacturing processes used in the OMEGA EP vacuum systems are subject to approval through a qualification process,<sup>2</sup> it is necessary to monitor in-vacuum LIDT for optical components residing inside the GCC to ensure the failure-free and cost-effective operation of the laser. Since the OMEGA EP Laser System is designed to operate in a wide range of pulse durations (from about 500 fs up to 100 ps), the recent discovery that more than one type of defect species can initiate damage in regimes<sup>3</sup> of different pulse lengths has made the continuous evaluation of the LIDT more complex than originally anticipated.

A special protocol for a long-term damage testing campaign was established on OMEGA EP from the beginning of GCC population to monitor the damage performance of representative optics under exposure to the vacuum chamber environment. A set of small-size optics samples was selected and placed inside the GCC during normal operation, and routinely tested for damage on every quarterly GCC vent using the in-house short-pulse damage testing system. The samples were positioned near the most-critical optical elements and in areas undergoing the most intense maintenance activities. Over the last ten years, the long-term campaign was divided into three smaller campaigns.

The Round I Campaign (2007–2010) started using a set of development MLD gratings. Damage testing at a 600-fs pulse length showed no changes in the damage performance. The damage testing results at a 10-ps pulse length showed no significant change for 15 of the grating samples used during the GCC population period. A decline was observed, however, for three gratings. Due to the extensive damage testing schedule, only one grating sample remained under monitoring for the remainder of the Round I Campaign. This grating showed a 30% decline in the 10-ps damage testing results after three years of vacuum exposure inside the GCC.

The Round II Campaign (2010–2016) utilized three production witness grating samples (denoted as II-1, II-2, and II-3) and involved damage testing at a 10-ps pulse length in vacuum. The damage testing results for this round are summarized in Fig. 1(a). Variations in the LIDT values, observed over this six-year test period, may be separated into two regimes: (1) during the first three years where changes were small and (2) during the following three years where a considerable decline was observed. These results must be evaluated, taking into account that the system was in full operational mode during the period of the most LIDT decline. Overall, the 1-on-1 and *N*-on-1 thresholds dropped by ~40% concurrently. In addition, the online grating inspection system<sup>4</sup> on OMEGA EP detected damage onset during operation at a 100-ps pulse length at a fluence level significantly below the initial damage threshold measured using the production witness grating samples. Near the end of Round II testing, the LIDT's of all grating samples at 100 ps were similar to those at a 10-ps pulse length.

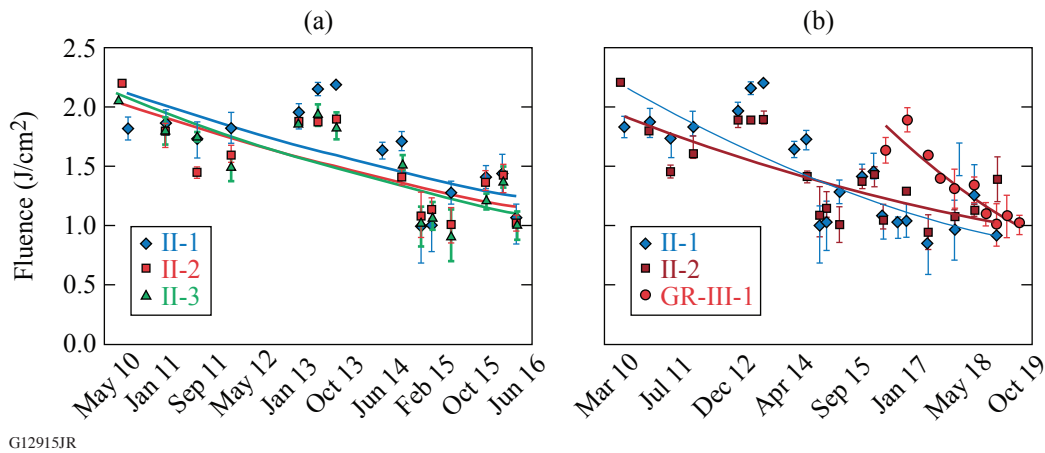


Figure 1  
 (a) The Round II and (b) Round III, *N*-on-1 damage testing results.

The Round III Campaign (2016–2019) encompassed an expanded protocol to monitor damage testing at a 100-ps pulse length. A “fresh” grating sample (GR-III-1) and the representative grating high-reflector (GHR) coating (HR-III-1) were included in the experiment to study potential differences in the vacuum performance between the MLD gratings and regular coatings. The representative grating high reflector is identical to the regular grating MLD coating with the exception of the top silica layer, which has a reduced thickness (609 nm to 440 nm) and no etched grating structure. To separate the vacuum effects from the aging-related changes in the optics performance, the fresh grating and coating samples had an equivalent twin (GR-III-2 and HR-III-2, respectively) that was stored in air throughout the campaign. Furthermore, one sample (II-3) from the Round II Campaign was removed from the study and stored in air.

Figure 1(b) summarizes the 10-ps-pulse-length damage testing results obtained during the Round III campaign combined (to enable direct comparison) with the data from Round II. Both 1-on-1 and *N*-on-1 damage thresholds for the fresh grating sample GR-III-1 were reduced by 40% over three years. This decline is exactly the same as the reduction of the damage threshold experienced by the gratings II-1 and II-2 during Round II, but it occurred twice as fast. The 10-ps damage thresholds for these two remaining Round II grating samples continued to decline during Round III with the 1-on-1 and *N*-on-1 LIDT reduced by 20% and 10%, respectively. However, the damage thresholds for the Round II gratings II-1 and II-2 showed no further measurable decline at the 100-ps pulse length.

Damage testing results at a 100-ps pulse length of Round III, GCC-stored fresh grating GR-III-1 are presented in Fig. 2, combined for comparison with the 10-ps data for the same sample. The damage testing results at a 100-ps pulse length for the fresh grating GR-III-1 declined significantly faster in comparison with the 10-ps data. Specifically, the 100-ps 1-on-1 and *N*-on-1 damage thresholds dropped by ~50% and ~70%, respectively. As a result, the damage threshold at 10 ps and 100 ps converged. On the other hand, no convergence between 10-ps and 100-ps damage thresholds was observed for grating GR-III-2, which was stored in air.

The GHR coating sample HR-III-1, stored inside the GCC, showed no change in damage thresholds at 10 ps, but the damage behavior changed significantly at a 100-ps pulse length. The 1-on-1 damage threshold at 100 ps dropped by ~50% after three years in vacuum, while the *N*-on-1 remained unchanged.

The overall percentage decline in the damage thresholds in all, GCC and in-air stored, samples (Fig. 3) depicts a clear difference in the vacuum damage performance between the MLD gratings and GHR coatings. The damage thresholds of the MLD’s grating were reduced in vacuum by up to 70%, depending on the pulse length. For the GHR coatings, only the 1-on-1 damage threshold at a 100-ps pulse length was affected by the environment inside the GCC. Both grating and GHR-coating samples revealed no change in the damage performance after three years of aging in ambient air.

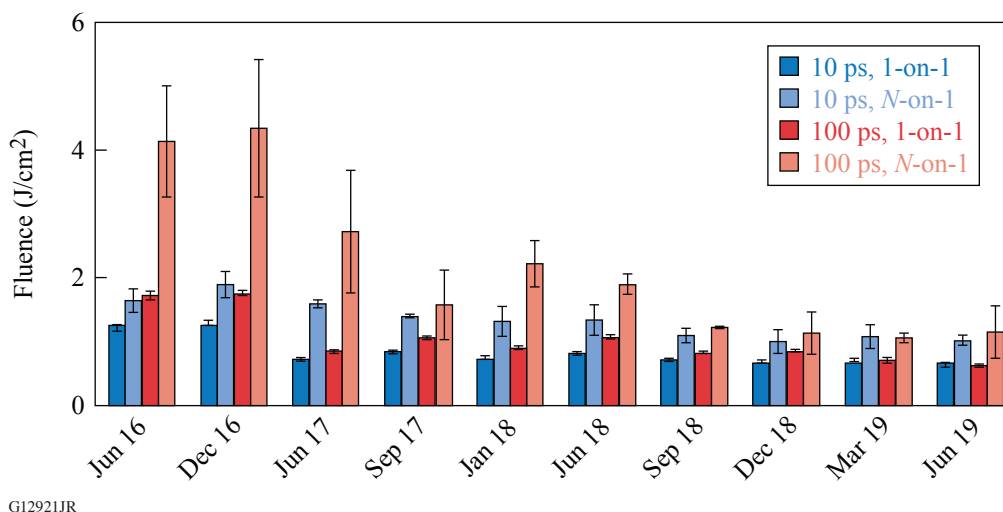


Figure 2  
Round III, “fresh” grating GR-III-1: The 10-ps and 100-ps damage thresholds converged under vacuum exposure inside the GCC.

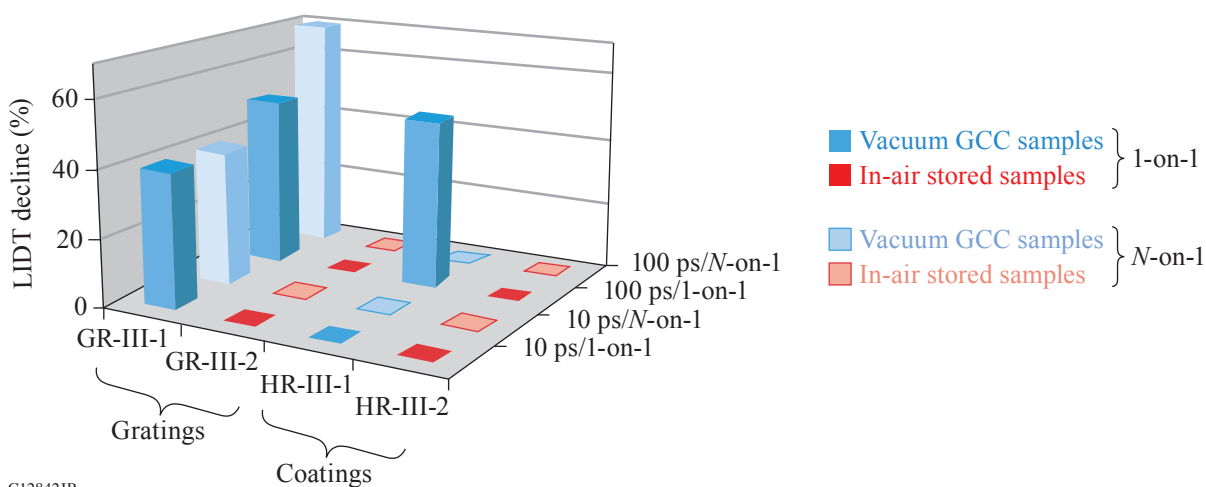


Figure 3  
The evolution of the damage performance of the MLD-grating and GHR-coating samples during Round III.

Surface plasma cleaning was used on grating sample II-3 to target potential organic volatile contaminants, presumably accumulated on the grating surface under vacuum inside the GCC.<sup>5</sup> The results indicated that the air–plasma cleaning method did not improve the damage performance of the grating. This suggests that the degradation of the grating damage performance under vacuum conditions inside the GCC is not related to volatile organic contamination.

Particles that attach to the surface of optics (contaminants) can be precursors for damage initiation on these optics at significantly lower fluences than the corresponding pristine optical elements. Offline studies have shown that particles on the surface can significantly lower the damage thresholds.<sup>6</sup> It is currently unclear, however, what types of particles may be present inside

the GCC and if they correlate with the reduced damage performance of the compression gratings discussed in this work. In an effort to perform a preliminary analysis of the contamination load inside the OMEGA EP GCC, particles were collected from seven locations near optical elements during the December 2019 vent period. The initial analysis was focused on determining the particle composition and was limited to the larger particles ( $>50 \mu\text{m}$  diameter). Particles were found at every collection location with the most frequently observed type being metallic particles and fibers, for the subset of particles that were chemically characterized. Several different metal particles were identified, including aluminum, stainless steel, silver, and copper. Plastic (PVC) particles were also found near the compressor grating and the lower compressor deformable mirror. Glass particles were less commonly observed.

Differences in damage degradation behavior between the MLD grating and corresponding GHR coating may arise from the different damage initiation mechanisms. As reported in Ref. 3, the damage of  $\text{HfO}_2/\text{SiO}_2$ -based HR's by laser pulses longer than 10 ps is defect-driven Type II or Type III, originating at depths around 600 nm and  $>100$  nm, respectively. Conversely, damage initiation in gratings with picosecond pulses originates in the pillars (the location of peak electric-field intensity enhancement) and is associated with defect-induced localized absorption.<sup>7</sup> Therefore, damage in the MLD grating and the GHR coating occurs at different locations. The damage-initiation mechanisms described above apply for the case of the "pristine" optic (grating or GHR coating). Assuming there is contamination involved, the problem becomes more complex and would require additional studies to resolve. However, the existing results may help obtain insight into the possible processes.

Recent work that considered the interaction of model contamination particles (metal, plastic, and glass) located on the surface on an MLD mirror with pulses at 0.6 and 10 ps revealed that the threshold for metal particle ejection and secondary contamination (via nanodroplets) is largely dependent on only the fluence.<sup>6</sup> These processes take place at fluences below the particle-induced LIDT of the mirror. If we further consider that damage is initiated by the generated (secondary contamination) nanoparticles, due to their small size, heat diffusion would be limited and damage would be only a function of total fluence. This would explain the convergence of the 100-ps 1-on-1 LIDT toward the 10-ps 1-on-1 LIDT (as depicted in Fig. 2). Regarding the behavior of the grating samples, the introduction of metal contamination particles would alter the localized electric-field distribution near the pillars creating "hot" spots with higher electric-field intensity. This in turn would facilitate a reduction of the LIDT. Additional work would be required to validate the above hypothetical.

This material is based upon work supported by the Department of Energy National Nuclear Security Administration under Award Number DE-NA0003856, the University of Rochester, and the New York State Energy Research and Development Authority.

1. N. Bonod and J. Neauport, *Adv. Opt. Photon.* **8**, 156 (2016).
2. B. Ashe *et al.*, *Proc. SPIE* **7069**, 706902 (2008).
3. A. A. Kozlov *et al.*, *Sci. Rep.* **9**, 607 (2019).
4. J. Qiao *et al.*, *Opt. Express* **18**, 10,423 (2010).
5. H. P. Howard *et al.*, *Appl. Opt.* **52**, 1682 (2013).
6. K. R. P. Kafka and S. G. Demos, *Opt. Lett.* **44**, 1844 (2019).
7. B. N. Hoffman *et al.*, "Mechanisms of Picosecond Laser-Induced Damage in Common Multilayer Dielectric Gratings," to be published in *Optics Express*, see also, this issue of LLE Review Quarterly Report **162**, 77.

## FY20 Q2 Laser Facility Report

J. Puth, M. Labuzeta, D. Canning, and R. T. Janezic

Laboratory for Laser Energetics, University of Rochester

During the second quarter of FY20, the Omega Laser Facility conducted 285 target shots on OMEGA and 218 target shots on OMEGA EP for a total of 503 target shots (see Tables I and II). OMEGA averaged 11.4 target shots per operating day, averaging 93.2% Availability and 94.4% Experimental Effectiveness.

OMEGA EP was operated extensively in Q2 FY20 for a variety of user experiments. OMEGA EP averaged 9.1 target shots per operating day, averaging 98.2% Availability and 95.6% Experimental Effectiveness.

Table I: OMEGA Laser System target shot summary for Q2 FY20.

<b>Program</b>	<b>Laboratory</b>	<b>Planned Number of Target Shots</b>	<b>Actual Number of Target Shots</b>
ICF	LLE	93.5	92
	LLNL	22	21
ICF Subtotal		115.5	113
HED	LLE	11	8
	LANL	22	23
	LLNL	38.5	41
HED Subtotal		71.5	72
LBS	LLNL	16.5	19
LBS Subtotal		16.5	19
NLUF		44	49
LLE Calibration	LLE	0	32
<b>Grand Total</b>		<b>247.5</b>	<b>285</b>

Table II: OMEGA EP Laser System target shot summary for Q2 FY20.

<b>Program</b>	<b>Laboratory</b>	<b>Planned Number of Target Shots</b>	<b>Actual Number of Target Shots</b>
ICF	LLE	31.5	44
	LLNL	7	11
	NRL	7	10
<b>ICF Subtotal</b>		<b>45.5</b>	<b>65</b>
HED	LLE	28	41
	LANL	14	15
	LLNL	28	38
<b>HED Subtotal</b>		<b>70</b>	<b>94</b>
LBS	LLE	7	14
	LANL	7	5
	Princeton University	7	7
<b>LBS Subtotal</b>		<b>21</b>	<b>26</b>
NLUF		7	7
LaserNetUS		7	14
LLE Calibration	LLE	0	12
<b>Grand Total</b>		<b>150.5</b>	<b>218</b>

## Publications and Conference Presentations

### Publications

- M. Bailly-Grandvaux, J. Kim, C. M. Krauland, S. Zhang, M. Dozières, M. S. Wei, W. Theobald, P. E. Grabowski, J. J. Santos, Ph. Nicolaï, P. McKenna, M. P. Desjarlais, and F. N. Beg, “Transport of kJ-Laser-Driven Relativistic Electron Beams in Cold and Shock-Heated Vitreous Carbon and Diamond,” *New J. Phys.* **22**, 033031 (2020).
- X. Bian, H. Aluie, D. Zhao, H. Zhang, and D. Livescu, “Revisiting the Late-Time Growth of Single-Mode Rayleigh–Taylor Instability and the Role of Vorticity,” *Physica D* **403**, 132250 (2020).
- S. Depierreux, C. Neuville, V. Tassin, M.-C. Monteil, P.-E. Masson-Laborde, C. Baccou, P. Fremerye, F. Philippe, P. Seytor, D. Teychenné, J. Katz, R. Bahr, M. Casanova, N. Borisenko, L. Borisenko, A. Orekhov, A. Colaitis, A. Debayle, G. Duchateau, A. Heron, S. Huller, P. Loiseau, P. Nicolai, C. Riconda, G. Tran, C. Stoeckl, W. Seka, V. Tikhonchuk, D. Pesme, and C. Lobaune, “Experimental Investigation of the Collective Stimulated Brillouin and Raman Scattering of Multiple Laser Beams in Inertial Confinement Fusion Experiments,” *Plasma Phys. Control. Fusion* **62**, 014024 (2020).
- C. Dorrer, E. M. Hill, and J. D. Zuegel, “High-Energy Parametric Amplification of Spectrally Incoherent Broadband Pulses,” *Opt. Express* **28**, 451 (2020).
- M. Dozières, S. Hansen, P. Forestier-Colleoni, C. McGuffey, D. Kawahito, M. Bailly-Grandvaux, K. Bhutwala, C. M. Krauland, M. S. Wei, P. Gourdain, J. R. Davies, K. Matsuo, S. Fujioka, E. M. Campbell, J. L. Peebles, J. J. Santos, D. Batani, S. Zhang, and F. N. Beg, “Characterization of an Imploding Cylindrical Plasma for Electron Transport Studies Using X-Ray Emission Spectroscopy,” *Phys. Plasmas* **27**, 023302 (2020).
- M. Gatu Johnson, P. J. Adrian, K. S. Anderson, B. D. Appelbe, J. P. Chittenden, A. J. Crilly, D. Edgell, C. J. Forrest, J. A. Frenje, V. Yu. Glebov, B. M. Haines, I. Igumenshchev, D. Jacobs-Perkins, R. Janezic, N. V. Kabadi, J. P. Knauer, B. Lahmann, O. M. Mannion, F. J. Marshall, T. Michel, F. H. Séguin, R. Shah, C. Stoeckl, C. A. Walsh, and R. D. Petrasso, “Impact of Stalk on Directly Driven Inertial Confinement Fusion Implosions,” *Phys. Plasmas* **27**, 032704 (2020).
- M. J. Guardalben, M. Barczys, B. E. Kruschwitz, M. Spilatro, L. J. Waxer, and E. M. Hill, “Laser-System Model for Enhanced Operational Performance and Flexibility on OMEGA EP,” *High Power Laser Sci. Eng.* **8**, e8 (2020).
- B. M. Haines, R. C. Shah, J. M. Smidt, B. J. Albright, T. Cardenas, M. R. Douglas, C. Forrest, V. Yu. Glebov, M. A. Gunderson, C. E. Hamilton, K. C. Henderson, Y. Kim, M. N. Lee, T. J. Murphy, J. A. Oertel, R. E. Olson, B. M. Patterson, R. B. Randolph, and D. W. Schmidt, “Observation of Persistent Species Temperature Separation in Inertial Confinement Fusion Mixtures,” *Nat. Commun.* **11**, 544 (2020).
- K. D. Humbird, J. L. Peterson, B. K. Spears, and R. G. McClaren, “Transfer Learning to Model Inertial Confinement Fusion Experiments,” *IEEE Trans. Plasma Sci.* **48**, 61 (2020).
- V. V. Ivanov, A. V. Maximov, A. L. Astanovitskiy, I. A. Begishev, R. Betti, J. R. Davies, C. Mileham, J. D. Moody, C. Stoeckl, K. J. Swanson, N. L. Wong, and J. Bromage, “Study of Laser-Driven Magnetic Fields with a Continuous Wave Faraday Rotation Diagnostic,” *Phys. Plasmas* **27**, 033102 (2020).
- T. Z. Kosc, H. Huang, T. J. Kessler, A. Maltsev, and S. G. Demos, “Measurement of the Angular Dependence of the Spontaneous Raman Scattering in Anisotropic Crystalline Materials Using Spherical Samples: Potassium Dihydrogen Phosphate as a Case Example,” *Rev. Sci. Instrum.* **91**, 015101 (2020).
- N. S. Krasheninnikova, M. J. Schmitt, K. Molvig, S. C. Hsu, B. S. Scheiner, D. W. Schmidt, V. Geppert-Kleinrath, P. W. McKenty, D. T. Michel, D. H. Edgell, F. J. Marshall, and H. Huang, “Development of a Directly Driven Multi-Shell Platform: Laser Drive Energetics,” *Phys. Plasmas* **27**, 022706 (2020).

- L. S. Leal, A. V. Maximov, R. Betti, A. B. Sefkow, and V. V. Ivanov, "Modeling Magnetic Confinement of Laser-Generated Plasma in Cylindrical Geometry Leading to Disk-Shaped Structures," *Phys. Plasmas* **27**, 022116 (2020).
- J. Li, S. Zhang, C. M. Krauland, H. Wen, F. N. Beg, C. Ren, and M. S. Wei, "Pump Depletion and Hot-Electron Generation in Long-Density-Scale-Length Plasma with Shock-Ignition High-Intensity Laser," *Phys. Rev. E* **101**, 033206 (2020).
- Y. Lu, S. Li, H. Li, K. A. Flippo., D. Barnak, A. Birkel, B. Lahmann, C. K. Li, A. M. Rasmus, K. Kelso, A. Zylstra, E. Liang, P. Tzeferacos, and D. Lamb, "Modeling Hydrodynamics, Magnetic Fields, and Synthetic Radiographs for High-Energy-Density Plasma Flows in Shock-Shear Targets," *Phys. Plasmas* **27**, 012303 (2020).
- K. Luo, V. V. Karasiev, and S. B. Trickey, "Towards Accurate Orbital-Free Simulations: A Generalized Gradient Approximation for the Noninteracting Free Energy Density Functional," *Phys. Rev. B* **101**, 075116 (2020).
- S. MacNally, C. Smith, J. Spaulding, J. Foster, and J. B. Oliver, "Glancing-Angle-Deposited Silica Films for Ultraviolet Wave Plates," *Appl. Opt.* **59**, A155 (2020).
- A. L. Milder, H. P. Le, M. Sherlock, P. Franke, J. Katz, S. T. Ivancic, J. L. Shaw, J. P. Palastro, A. M. Hansen, I. A. Begishev, W. Rozmus, and D. H. Froula, "Evolution of the Electron Distribution Function in the Presence of Inverse Bremsstrahlung Heating and Collisional Ionization," *Phys. Rev. Lett.* **124**, 025001 (2020).
- M. Millot, S. Zhang, D. E. Fratanduono, F. Coppari, S. Hamel, B. Militzer, D. Simonova, S. Shcheka, N. Dubrovinskaia, L. Dubrovinsky, and J. H. Eggert, "Recreating Giants Impacts in the Laboratory: Shock Compression of MgSiO<sub>3</sub> Bridgmanite to 14 Mbar," *Geophys. Res. Lett.* **47**, e2019GL085476 (2020).
- J. Nilsen, A. L. Kritcher, M. E. Martin, R. E. Tipton, H. D. Whitley, D. C. Swift, T. Döppner, B. L. Bachmann, A. E. Lazicki, N. B. Kostinski, B. R. Maddox, G. W. Collins, S. H. Glenzer, and R. W. Falcone, "Understanding the Effects of Radiative Preheat and Self-Emission from Shock Heating on Equation of State Measurement at 100s of Mbar Using Spherically Converging Shock Waves in a NIF Hohlraum," *Matter Radiat. Extremes* **5**, 018401 (2020).
- J. B. Oliver, A. L. Rigatti, T. Noll, J. Spaulding, J. Hettrick, V. Gruschow, G. Mitchell, D. Sadowski, C. Smith, and B. Charles, "Large-Aperture Coatings for Fusion-Class Laser Systems," *Appl. Opt.* **59**, A7 (2020).
- J. B. Oliver, J. Spaulding, and B. Charles, "Stress Compensation by Deposition of a Nonuniform Corrective Coating," *Appl. Opt.* **59**, A54 (2020).
- J. P. Palastro, J. L. Shaw, P. Franke, D. Ramsey, T. T. Simpson, and D. H. Froula, "Dephasingless Laser Wakefield Acceleration," *Phys. Rev. Lett.* **124**, 134802 (2020).
- V. A. Smalyuk, C. R. Weber, O. L. Landen, S. Ali, B. Bachmann, P. M. Celliers, E. L. Dewald, A. Fernandez, B. A. Hammel, G. Hall, A. G. MacPhee, L. Pickworth, H. F. Robey, N. Alfonso, K. L. Baker, L. F. Berzak Hopkins, L. Carlson, D. T. Casey, D. S. Clark, J. Crippen, L. Divol, T. Döppner, M. J. Edwards, M. Farrell, S. Felker, J. E. Field, S. W. Haan, A. V. Hamza, M. Havre, M. C. Herrmann, W. W. Hsing, S. Khan, J. Kline, J. J. Kroll, S. LePape, E. Loomis, B. J. MacGowan, D. Martinez, L. Masse, M. Mauldin, J. L. Milovich, A. S. Moore, A. Nikroo, A. Pak, P. K. Patel, J. L. Peterson, K. Raman, B. A. Remington, N. Rice, M. Schoff, and M. Stadermann, "Review of Hydrodynamic Instability Experiments in Inertially Confined Fusion Implosions on National Ignition Facility," *Plasma Phys. Control. Fusion* **62**, 014007 (2020).
- C. Smith, S. MacNally, and J. B. Oliver, "Ellipsometric Modeling of Serially Bi-Deposited Glancing-Angle-Deposition Coatings," *Appl. Opt.* **59**, A26 (2020).
- W. Theobald, C. Sorce, W. R. Donaldson, R. Epstein, R. L. Keck, C. Kellogg, T. J. Kessler, J. Kwiatkowski, F. J. Marshall, S. Sampat, W. Seka, R. C. Shah, A. Shvydky, C. Stoeckl, L. J. Waxer, and S. P. Regan, "Inferred UV Fluence Focal-Spot Profiles from Soft X-Ray Pinhole-Camera Measurements on OMEGA," *Rev. Sci. Instrum.* **91**, 023505 (2020).
- D. Turnbull, A. Colaitis, A. M. Hansen, A. L. Milder, J. P. Palastro, J. Katz, C. Dorrer, B. E. Kruschwitz, D. J. Strozzi, and D. H. Froula, "Impact of the Langdon Effect on Crossed-Beam Energy Transfer," *Nat. Phys.* **16**, 181 (2020).
- M. P. Valdivia, D. Stutman, C. Stoeckl, C. Mileham, J. Zou, S. Muller, K. Kaiser, C. Sorce, P. A. Keitner, J. R. Fein, M. Trantham, R. P. Drake, and S. P. Regan, "Implementation of a Talbot-Lau X-Ray Deflectometer Diagnostic Platform for the OMEGA EP Laser," *Rev. Sci. Instrum.* **91**, 023511 (2020).

S. Zhang, C. M. Krauland, J. Peebles, J. Li, F. N. Beg, N. Alexander, W. Theobald, R. Betti, D. Haberberger, E. M. Campbell, R. Yan, E. Borwick, C. Ren, and M. S. Wei,

“Experimental Study of Hot Electron Generation in Shock Ignition Relevant High-Intensity Regime with Large Scale Hot Plasmas,” *Phys. Plasmas* **27**, 023111 (2020).

### Forthcoming Publications

S. H. Cao, R. Yan, H. Wen, J. Li, and C. Ren, “Cogeneration of Hot Electrons from Multiple Laser–Plasma Instabilities,” to be published in *Physical Review E*.

B. Lahmann, F. J. Marshall, T. Michel, F. H. Séguin, C. Stoeckl, and R. D. Petrasso “3D xRAGE Simulation of Inertial Confinement Fusion Implosion with Imposed Mode 2 Laser Drive Asymmetry,” to be published in *High Energy Density Physics*.

L. Ceurvorst, R. Betti, A. Casner, V. Gopalaswamy, A. Bose, S. X. Hu, E. M. Campbell, S. P. Regan, C. A. McCoy, M. Karasik, J. Peebles, M. Tabak, and W. Theobald, “Hybrid Target Design for Imprint Mitigation in Direct-Drive Inertial Confinement Fusion,” to be published in *Physical Review E*.

B. M. Haines, D. E. Keller, J. A. Marozas, P. W. McKenty, K. S. Anderson, T. J. B. Collins, W. W. Dai, M. L. Hall, S. Jones, M. D. McKay Jr., R. M. Rauenzahn, and D. N. Woods, “Coupling Laser Physics to Radiation-Hydrodynamics,” to be published in *Computers and Fluids*.

L. E. Chen, A. F. A. Bott, P. Tzeferacos, A. Rigby, A. Bell, R. Bingham, C. Graziani, J. Katz, M. Koenig, C. K. Li, R. Petrasso, H.-S. Park, J. S. Ross, D. Ryu, T. G. White, B. Reville, J. Matthews, J. Meinecke, F. Miniati, E. G. Zweibel, S. Sarkar, A. A. Schekochihin, D. Q. Lamb, D. H. Froula, and G. Gregori, “Transport of High-Energy Charged Particles Through Spatially Intermittent Turbulent Magnetic Fields,” to be published in *The Astrophysical Journal*.

E. C. Hansen, J. R. Davies, D. H. Barnak, R. Betti, E. M. Campbell, V. Yu. Glebov, J. P. Knauer, L. S. Leal, J. L. Peebles, A. B. Sefkow, and K. M. Woo, “Neutron Yield Enhancement and Suppression by Magnetization in Laser-Driven Cylindrical Implosions,” to be published in *Physics of Plasmas* (invited).

A. R. Christopherson, R. Betti, S. Miller, V. Gopalaswamy, O. M. Mannion, and D. Cao, “Theory of Ignition and Burn Propagation in Inertial Fusion Implosions,” to be published in *Physics of Plasmas*.

S. X. Hu, V. V. Karasiev, V. Recoules, P. M. Nilson, N. Brouwer, and M. Torrent, “Interspecies Radiative Transition in Warm and Superdense Plasma Mixtures,” to be published in *Nature Communications*.

C. Fagan, M. Sharpe, W. T. Shmayda, and W. U. Schröder, “A Thin Alumina Film as a Tritium Adsorption Inhibitor for Stainless-Steel 316,” to be published in *Fusion Science and Technology*.

A. Kar, S. X. Hu, G. Duchateau, J. Carroll-Nellenback, and P. B. Radha, “Implementing a Microphysics Model in Hydrodynamic Simulations to Study the Initial Plasma Formation in Dielectric Ablator Materials for Direct-Drive Implosions,” to be published in *Physical Review E*.

R. K. Follett, J. G. Shaw, J. F. Myatt, D. H. Froula, and J. P. Palastro, “Multibeam Absolute Stimulated Raman Scattering and Two-Plasmon Decay,” to be published in *Physical Review E*.

O. M. Mannion, J. P. Knauer, V. Yu. Glebov, C. J. Forrest, A. Liu, Z. L. Mohamed, M. H. Romanofsky, T. C. Sangster, C. Stoeckl, and S. P. Regan, “A Suite of Neutron Time-of-Flight Detectors to Measure Hot-Spot Motion in Direct-Drive Inertial Confinement Fusion Experiments on OMEGA,” to be published in *Nuclear Instruments and Methods in Physics Research, A*.

W. Fox, D. B. Schaeffer, M. J. Rosenberg, G. Fiksel, J. Matteucci, H.-S. Park, A. F. A. Bott, K. Lezhnin, A. Bhattacharjee, D. Kalantar, B. A. Remington, D. Uzdensky, C. K. Li, F. H. Séguin, and S. X. Hu, “Fast Magnetic Reconnection in Highly Extended Current Sheets at the National Ignition Facility,” to be published in *Physics of Plasmas*.

D. I. Mihaylov, V. V. Karasiev, and S. X. Hu, “Thermal Hybrid Exchange-Correlation Density Functional for Improving the Description of Warm Dense Matter,” to be published in *Physical Review B*.

M. Gatu Johnson, B. M. Haines, P. J. Adrian, C. Forrest, J. A. Frenje, V. Yu. Glebov, W. Grimble, R. Janezic, J. P. Knauer,

H. G. Rinderknecht, D. T. Casey, R. Hatarik, R. M. Bionta, B. J. MacGowan, P. Patel, O. L. Landen, E. P. Hartouni, and O. A.

Hurricane, “Azimuthal Drive Asymmetry in Inertial Confinement Fusion Implosions on the National Ignition Facility,” to be published in *Physical Review Letters*

M. J. Rosenberg, A. A. Solodov, W. Seka, R. K. Follett, J. F. Myatt, A. V. Maximov, C. Ren, S. Cao, P. Michel, M. Hohenberger, J. P. Palastro, C. Goyon, T. Chapman, J. E. Ralph, J. D. Moody, R. H. H. Scott, K. Glize, and S. P. Regan, “Stimulated Raman Scattering Mechanisms and Scaling Behavior in Planar Direct-Drive Experiments at the National Ignition Facility,” to be published in *Physics of Plasmas*.

J. R. Rygg, R. F. Smith, A. E. Lazicki, D. G. Braun, D. E. Fratanduono, R. G. Kraus, J. M. McNaney, D. C. Swift, C. E. Wehrenberg, F. Coppari, M. F. Ahmed, M. A. Barrios, K. J. M. Blobaum, G. W. Collins, A. L. Cook, P. Di Nicola, E. G. Dzenitis, S. Gonzales, B. F. Heidl, M. Hohenberger, A. House, N. Izumi, D. H. Kalantar, S. F. Khan, T. R. Kohut, C. Kumar, N. D. Masters, D. N. Polsin, S. P. Regan, C. A. Smith, R. M. Vignes, M. A. Wall, J. Ward, J. S. Wark, T. L. Zobrist, A. Arsenlis, and J. H. Eggert, “X-Ray Diffraction at the National Ignition Facility,” to be published in *Review of Scientific Instruments*.

R. W. Short, “Absolute Stimulated Raman Side Scatter in Direct-Drive Laser-Produced Plasmas,” to be published in *Physics of Plasmas*.

R. Sobolewski, “Optical Detectors and Sensors,” to be published in the *Handbook of Superconducting Materials*.

A. A. Solodov, M. J. Rosenberg, W. Seka, J. F. Myatt, M. Hohenberger, R. Epstein, C. Stoeckl, R. W. Short, S. P. Regan, P. Michel, T. Chapman, R. K. Follett, J. P. Palastro, D. H. Froula, P. B. Radha, J. D. Moody, and V. N. Goncharov, “Hot-Electron Generation at Direct-Drive Ignition-Relevant Plasma Conditions at the National Ignition Facility,” to be published in *Physics of Plasmas*.

G. F. Swadling, C. Bruulsema, F. Fiuza, D. P. Higginson, C. M. Huntington, H.-S. Park, B. B. Pollock, W. Rozmus, H. G. Rinderknecht, J. Katz, A. Birkel, and J. S. Ross, “Measurement of Kinetic-Scale Current Filamentation Dynamics and Associated Magnetic Fields in Interpenetrating Plasmas,” to be published in *Physical Review Letters*.

S. Tochitsky, A. Pak, F. Fiuza, D. Haberberger, N. Lemos, A. Link, D. H. Froula, and C. Joshi, “Laser-Driven Collisionless Shock Acceleration of Ions from Near-Critical Plasmas,” to be published in *Physics of Plasmas*.

D. Turnbull, A. V. Maximov, D. H. Edgell, W. Seka, R. K. Follett, J. P. Palastro, D. Cao, V. N. Goncharov, C. Stoeckl, and D. H. Froula, “Anomalous Absorption by the Two-Plasmon–Decay Instability,” to be published in *Physical Review Letters*.

T. Walton, J. L. Sebold, I. E. Golovkin, J. J. MacFarlane, V. N. Golovkina, A. A. Solodov, P. M. Nilson, and R. Epstein, “Parameterizing Hot-Electron Energy Distributions for Tabular Emissivities and Opacities,” to be published in *High Energy Density Physics*.

K. M. Woo, R. Betti, O. M. Mannion, C. J. Forrest, J. P. Knauer, V. N. Goncharov, P. B. Radha, D. Patel, V. Gopalaswamy, and V. Yu. Glebov, “Inferring Thermal Ion Temperature and Residual Kinetic Energy from Nuclear Measurements in Inertial Confinement Fusion Implosions,” to be published in *Physics of Plasmas* (invited).

J. Zhang, R. Wei, M. El Kabbash, E. M. Campbell, and C. Guo, “Thin-Film Perfect Infrared Absorbers over Single- and Dual-Band Atmospheric Windows,” to be published in *Optics Letters*.

Y. Zhao and W. R. Donaldson, “Ultrafast UV AlGaIn Metal–Semiconductor–Metal Photodetector With a Response Time Below 25 ps,” to be published in the *IEEE Journal of Quantum Electronics*.

A. B. Zylstra, H. W. Hermann, Y. H. Kim, A. McEvoy, J. A. Frenje, M. Gatu Johnson, R. D. Petrasso, V. Yu. Glebov, C. Forrest, J. Delettrez, S. Gales, and M. Rubery, “ ${}^2\text{H}(p, \gamma){}^3\text{He}$  Cross Section Measurement Using High-Energy-Density Plasmas,” to be published in *Physical Review C*.

A. B. Zylstra, J. R. Rygg, G. W. Collins, C. K. Li, J. A. Frenje, R. D. Petrasso, S. R. Nagel, P. Fitzsimmons, and H. Reynolds, “Platform Development for  $dE/dx$  Measurements on Short-Pulse Laser Facilities,” to be published in *High Energy Density Physics*.

---

**Conference Presentations**

---

T. Z. Kosc, T. J. Kessler, H. Huang, and S. G. Demos, "Raman Polarizability Tensor in Potassium Dihydrogen Phosphate and Deuterated Potassium Dihydrogen Phosphate Crystals," presented at Photonics West 2020, San Francisco, CA, 1–6 February 2020.

---

M. K. Ginnane, D. N. Polsin, X. Gong, L. Crandall, T. R. Boehly, J. R. Rygg, G. W. Collins, A. Lazicki, R. Kraus, J. H. Eggert, M. C. Marshall, D. E. Fratanduono, J.-P. Davis, C. A. McCoy, C. Seagle, and S. Root, "X-Ray Diffraction of Platinum," presented at the NIF User Group, Livermore, CA, 3–5 February 2020.

---

The following presentations were made at the 60th Sanibel Symposium, St. Simons Island GA, 16–21 February 2020:

M. Ghosh, S. Zhang, and S. X. Hu, "Nanodiamond Formation in Hydrocarbons Under Extreme Pressure-Temperature Conditions-Evidence from First Principles."

V. V. Karasiev, J. Hinz, and S. X. Hu, "Characterization of the Liquid–Liquid Phase Transition in Dense Hydrogen: The Role of Accurate Exchange–Correlation and Nuclear Quantum Effects."

---

D. H. Froula, "Plasma Physics at the University of Rochester Laboratory for Laser Energetics," presented at the Office of Science, Rochester, NY, 24 February 2020.

---

J. L. Peebles, J. R. Davies, D. H. Barnak, T. Cracium, M. J. Bonino, and R. Betti, "Axial Proton Probing of Single and Double Plate Laser-Driven Coils," presented at the 2020 Stewardship Science Academic Programs Symposium, Washington, DC, 26–27 February 2020.

---

M. S. Wei, "OMEGA EP Experimental Capability: First-Year LaserNetUS Experiments and Future Plans," presented at the Laser-NetUS SAB and PI Meeting, Washington, DC, 3–4 March 2020.



